UNIVERSIDADE DE LISBOA
FACULDADE DE CIÊNCIAS
DEPARTAMENTO DE FÍSICA

Calibration of MR-Images for Accurate Dose Calculations

Filipa Borges Ferreira Guerreiro

Orientadores

Orientador Externo: Prof. Dr. Uwe Oelfke, Institute of Cancer Research, London, UK
Orientador Interno: Prof. Dr. Luís Peralta, Departamento de Física da Faculdade de Ciências da Universidade de Lisboa, Portugal

MESTRADO INTEGRADO EM ENGENHARIA BIOMÉDICA E BIOFÍSICA
Perfil de Radiações em Diagnóstico e Terapia

DISSERTAÇÃO

2015

Resumo

A Radioterapia é uma especialidade médica que resulta da utilização controlada de fontes de radiação ionizantes de alta energia com o principal objetivo de danificar o maior número de células tumorais e de preservar ao máximo os órgãos de risco adjacentes ao tecido tumoral. A prática clínica de radioterapia é planeada com base em imagens de Tomografia Computorizada (TC) do paciente. A modalidade de TC é assim escolhida visto oferecer uma elevada resolução espacial e também o mapa de distribuição da densidade eletrónica dos tecidos. A primeira possibilita o posicionamento adequado do paciente durante as sessões de imagiologia e posteriormente de tratamento enquanto a segunda oferece as informações necessárias para o cálculo da estimativa de dose a ser entregue ao paciente. A principal razão para a substituição da TC pela modalidade de Ressonância Magnética (RM) é que a RM oferece um elevado contraste dos tecidos moles possibilitando assim uma maior precisão na delineação do tumor. Esta oferece também uma redução da dose total dada ao paciente visto que a dose durante as sessões de imagiologia é assim evitada.

Atualmente, clinicamente recorre-se ao uso de uma modalidade TC-RM, a fim de se combinar os contornos dos volumes definidos usando imagens de RM com a informação necessária para o planeamento fornecida pelas imagens de TC. No entanto, esta prática, assim como o uso individual de TC para o planeamento radio-terapêutico, é também não considerada ideal. Para o seu procedimento, o registo das duas modalidades de imagem é um requisito. Erros de magnitude desconhecida resultantes do alinhamento das duas imagens propagam-se sistematicamente ao longo de todo o tratamento comprometendo a eficácia do mesmo. Um seguimento natural seria a implementação de um procedimento de radioterapia apenas baseado no uso de RM. Para o mesmo, a obtenção de informação equivalente à dada por uma TC mas através dos dados fornecidos pela RM é necessária. A esta dá-se o nome de TC sintética (sTC), que não é mais do que uma falsa imagem de TC que servirá como *input* para o cálculo de dose como se de uma verdadeira TC se trata-se. Também a ter em conta está a obtenção de uma sTC geometricamente precisa a fim de se proceder ao posicionamento correto do paciente durante o tratamento.

Nesta tese dois tipos de metodologias para a obtenção de imagens sTC foram avaliadas para pacientes com cancro na cabeça e pescoço e na próstata: A primeira foi o método de atribuição de densidade (sTC_{ad}) e a segunda foi o método atlas (sTC_a). O método de atribuição de densidade é baseado na segmentação de classes de tecido às quais os valores de densidade eletrónica específicos são posteriormente atribuídos, numa tentativa de representar a distribuição heterogénea da densidade eletrónica do corpo humano. Dois tipos de sTC_{ad} foram obtidos diferindo apenas no modo de segmentação das classes. O primeiro foi derivado a partir da informação proveniente da TC (sCT_{ad}_TCinfo), mantendo-se assim a geometria do paciente constante. Este foi utilizado de modo a avaliar unicamente a exatidão das estimativas das densidades eletrónicas atribuídas aos tecidos do paciente. O segundo foi obtido a partir da informação proveniente da RM (sCT_{ad}_RMinfo) e assim todas as estruturas foram delineadas diretamente utilizando essa modalidade. Esta metodologia foi aplicada a fim de se estudar as incertezas introduzidas no

planeamento aquando a delineação realizada na RM. Visto que a delineação de classes como a estrutura óssea não pode ser efetuada automaticamente utilizando imagens de RM espera-se que este método esteja sujeito a erros introduzidos pela variabilidade inter-observador.

As imagens sTC_a foram obtidas através da utilização de um atlas que compreende um conjunto de imagens TC e RM alinhadas. A imagem de RM do paciente foi então interligada a todas as imagens RM-TC existentes no atlas através da utilização de medidas de semelhança imagiológica específicas e de processos de registo deformáveis de imagens. O valor de cada *voxel* da imagem sTC_a final foi então obtido usando uma média ponderada dos valores dos *voxels* na mesma posição em todas as imagens TC incluídas no atlas. Doses foram então recalculadas em cada sTC usando o plano clínico inicial e ambos os métodos foram avaliados dosimetricamente e geometricamente. A avaliação dosimétrica foi realizada usando mapas da diferença de dose, análise gama e histogramas de dose-volume recorrendo ao uso dos contornos clínicos para todos os métodos. A avaliação geométrica foi realizada com intuito de comparar contornos (estrutura óssea, contorno externo do paciente e órgãos de risco) delineados usando RM (e utilizados para o método sTC_{ad}_RMinfo) e sTC_a comparativamente com os contornos clínicos originais delineados na TC(e utilizados para o método sTC_{ad}_TCinfo). Os contornos foram comparados em termos de forma, posição e volume.

A implementação de um procedimento de tratamento de radioterapia unicamente baseado na informação proveniente de imagens RM estará intrinsecamente ligado à utilização do MR-LINAC que é uma máquina que compreende um scanner de RM acoplado a um acelerador de partículas possibilitando assim a obtenção de imagens simultaneamente à ocorrência do tratamento e a entrega de radiação com milímetros de precisão. No entanto, a presença de um campo magnético durante a entrega de dose leva à ocorrência de fenómenos dosimétricos que irão alterar a distribuição de dose prevista. Este efeito é geralmente conhecido como o efeito de retorno dos eletrões. Apesar do campo magnético não afetar diretamente os raios-x emitidos pelo acelerador, este irá causar alterações na trajetória percorrida pelos eletrões secundários gerados pela interação do feixe de radiação com a matéria. Estes ao chegarem à superfície e ao interagirem com o ar irão virar para trás, descrevendo uma trajetória em forma de hélice, e irão voltar a reentrar no corpo do paciente levando a um aumento da dose dada ao mesmo. Tendo isto em conta, nesta tese a capacidade de ambos sTC serem capazes de reproduzir estes efeitos dosimétricos, tanto na superfície do paciente como também na presença de cavidades de ar no interior do mesmo, foi também estudada.

O método sTC_a foi o método que apresentou os resultados mais robustos em termos de semelhança dosimétrica e geométrica com os resultados clínicos oferecidos pela TC real. Ambos sTC_{ad} e sTC_a mostraram ser adequados para a realização de cálculos de dose visto que diferenças significativas comparativamente com a distribuição de dose oferecida pela TC original não foram encontradas. Contudo, uma melhor precisão na cobertura da região que inclui o volume alvo foi obtida para sTC_a para ambos os pacientes. De acordo com a análise geométrica, a estrutura óssea e o contorno externo definidos usando sTC_a apresentaram um maior grau de semelhança em termos de forma, posição e volume com a TC real. Não foram tiradas conclusões significativas sobre os órgãos de risco, visto estes apresentarem desvios significativos na forma e no volume face aos contornos definidos na TC real. É no entanto do conhecimento comum que a delineação de estruturas de tecido mole é feita com maior precisão quando utilizando imagens de RM. Também, ambos sTC foram capazes de reproduzir o aumento de dose na superfície do paciente numa situação em que o campo magnético estivesse presente durante uma sessão de tratamento. No entanto, na presença de cavidades de ar no interior do paciente, ambos sTC mostraram-se insuficientes na simulação dos efeitos dosimétricos presentes.

Apesar de ambos sTC demonstrarem serem precisos o suficiente para o planeamento de dose, a estrutura óssea não pode ser delineada automaticamente usando sTC_{ad} e o tempo necessário para que o contorno esteja definido faz com que a sua implementação clínica seja pouco viável. Apesar de uma melhor precisão de distribuição de dose ser obtida para sTC_a, exatamente devido à estimativa dos valores de densidade ser feita de *voxel* para *voxel* em vez de assumir que cada classe tem um valor único de densidade eletrónica, a imagem final aparece mais desfocada do que uma imagem de TC real. Desta forma, este método não fornece informação suficiente para a delineação tanto das estruturas de risco como do volume alvo. Como proposta, nós sugerimos a utilização conjunta dos contornos dos órgãos de risco e do volume alvo delineados usando imagens de RM e a distribuição de densidade eletrónica fornecida por sTC_a para a implementação de um procedimento de tratamento radio-terapêutico tendo unicamente como base a informação proveniente de imagens de RM para possivelmente ser usado no futuro com máquinas MR-LINAC. No entanto, melhorias na precisão e na obtenção de sTC_a devem ser ainda levadas em conta. Uma melhor definição de fronteiras entre classes de tecidos deve ser adquirida bem como uma maior rapidez na aquisição destas imagens deve ser implementada a fim de se considerar o seu uso em âmbito clínico.

Palavras-Chave: Procedimento de Tratamento de Radioterapia baseado em RM , TC sintética, Método de Atribuição de Densidade, Método Atlas, MR-LINAC.

Abstract

The gold standard for radiotherapy treatment planning is CT imaging, as it provides high spatial resolution and electron density values. The main arguments for substituting CT for MRI are the superior soft-tissue contrast of MR images and the avoidance of imaging dose. An MRI-only workflow relies on a method to derive CT-equivalent information from MR data enabling the performance of dose calculations.

In this thesis, Bulk Density Assignments (sCT_{bda}) and Atlas-based (sCT_a) approaches were used to generate sCTs for H&N and prostate patients. sCT_{bda} methods using only CT or MR information for tissue classes delineation were obtained separately. sCT_a methods were generated from an anatomical atlas based on aligned CT-MR images. Local similarity measures and deformable image registration were used to match the patient's MRI with the atlas database. The final sCT_a was obtained using a voxelwise weighting scheme. Clinical plans were re-calculated on sCT_{bda} and sCT_a and both were evaluated dosimetric and geometrically. The dosimetric evaluation including gamma and DVH analysis was performed using the original planning contours. In the geometric evaluation the original contours and sCT_a and MRI delineations were assessed in terms of shape, position and volume. In the future, MRI-only external radiotherapy treatments are foreseen to be performed at MR-LINAC machines. The evaluation of the reproducibility of the dosimetric effects generated by the presence of a magnetic field during treatment delivery when using both sCTs for treatment planning was also investigated.

Dose re-calculations on sCTs showed no clinically relevant dose differences to the original dose distribution on the planning CT. Hence, both sCT are suitable to perform dose calculations. Contours based on MRI and sCT_a were found to be similar to the original clinical contours. However, bone segmentation on the MRI cannot be performed fully automatically and the sCT_a cannot provide information for the delineation of both target volume and organs at risk. Also, the electron return effect generated by the presence of a magnetic field was similarly represented for CT and both sCT_a and sCT_{bda} at the patient's boundary. We therefore suggest combining soft tissue contours based on MRI with bone contours and electron density values obtained from the sCT_a in order to establish a MRI-only workflow for future MR-LINAC machines.

Key-words: MRI-only Radiotherapy Treatment Planning, sCT, Bulk Density Assignment Approach, Atlas-based Approach, MR-LINAC.

Acknowledgments

Firstly, I would like to start by thanking to my supervisor **Uwe Oelfke** from the Institute of Cancer Research, who gave me the opportunity to return to London and to join this amazing project. I also want to thank him for his encouragement during this internship. Secondly, I would like to give a special thanks to **Antje Knopf** who was so patient and glad to teach me everything that I wanted to know and basically for all the guidance during my stay at ICR. I have learned a lot because of her and she was not just a good supervisor but also a great friend for me. I have the most respect for her and I wish her all the best in this world. I also want to thank to **Jamie McClelland** and to **Alex Dunlop** who were essential for my work for always being there to help me and advise me. Their expertise, understanding and patience added considerably to my project and I have the most respect for them and for their work and dedication.

I would like to thank very much to **Ninon Burgos** and **Jorge Cardoso** who were kind to share with me their Atlas method which was crucial to the success of this project. I would like to thank to **Catarina Veiga** who provided me all the initial help and support to get started with the prostate atlas and also to **Kee Wong** and **Imran Petkar** for always being available to perform the contouring for me. I also would like to thank to **Simeon Nill** for being the person who knows everything about everything. He was also a great help for me, mostly solving all the Monaco problems, and I have the highest consideration of him.

A big thank you to everybody in the **Radiotherapy and Physics Department** from ICR who received me so well and who made me feel that I was at home every day. I would specifically like to thank **Jamie Dean**, **Henry Tsang**, **Peter Ziegenhein** and **Corijn Kamerling**, my office buddies, for their friendship and for the great moments and happy times we spent together, and also **Martin Menten** for making fun of my meat and cheese every day.

I would also like to thank to my supervisor **Luís Filipe Peralta**, one of the best professors I ever had, for being always available to help me and for all the things that he taught me. I must also acknowledge the Reitoria da Universidade de Lisboa for the financial support, under the ERASMUS program, that made this internship possible.

In addition, a very special thanks to my friends **Francisco Melo**, **Célia Fernandes** and **Nádia Vilhena** who accompanied once more in this adventure that is living in London. Also I would like to thank to all my EBB colleagues for this last 5 years. It was a great journey and a pleasure to share it with them. Especially, I would like to thank to **Francisco Melo** and **Marciano Carmo** for all the talks, for all the laughs, for their friendship and for the great moments we spent together. Sem dúvida duas pessoas espetaculares que tive o prazer de conhecer e que não trocava por nada deste mundo. Trio maravilha, sempre!

I would also like to thank to one of the most important persons in my life **João Tourais**, for being there by my side every second of this journey, for being supportive even when I was being stubborn and basically for being who he is. A ti só te posso mesmo agradecer, por TUDO.

Last but not least, there are no words to describe how grateful I am to my wonderful parents **Maria** and **Vítor** for all the support and for making me the person that I am today, my brothers **Rodrigo** and **Bernardo** that I've especially missed shouting at and to my grandparents **Manuela** and **Adolfo**, who are like parents to me. Sem dúvida todas as metas alcançadas uma parte se deve a todo o apoio dado pela minha fantástica família!

Agora na minha língua materna, a todos um muito obrigada!

Contents

List of Abbreviations

2D Two-dimensional

3D Three-dimensional

BE Bending Energy

CFRT Conformal Radiotherapy

cm Centimeters

CT Computed Tomography

CTV Clinical Target Volume

DD Dose Difference

deg Degree

DICOM Digital Imaging and Communication in Medicine

DIR Deformable Image Registration

DSC Dice Similarity Coefficient

DTA Distance to Agreement

DVH Dose-Volume Histogram

ERE Electron Return Effect

EUD Equivalent Uniform Dose

FOV Field of View

FWHM Full Width at Half Maximum

GTV Gross Target Volume

Gy Gray

H&N Head and Neck

HU Hounsfield Unit

ICR Institute of Cancer Research

IMGT Image Guided Radiotherapy

IMRT Intensity Modulated Radiation Therapy

ITV Internal Target Volume

JL Squared Jacobian Determinant Log

k Power Law Exponent

kV Kilovoltage

LINAC Linear Accelerator

LNCC Local Normalized Correlation Coefficient

MeV Mega Electron Volt

mm Millimiters

MRI Magnetic Resonance Imaging

NCC Normalized Cross Correlation

NIfTI Neuroimaging Informatics Technology Initiative

NMI Normalized Mutual Information

NSSD Local Sum of Squares Differences

OAR Organ at Risk

PRGP Pattern Recognition with Gaussian Process

PTV Planning Target Volume

QA Quality Assurance

RMH Royal Marsden Hospital

RMS Root Mean Square

RTP Radiotherapy Treatment Planning

sCT Synthetic CT

T Tesla

TPS Treatment Planning System

UTE Ultrashort Echo Time

VMAT Volumetric Modulated Arc Therapy

VI Volume Index

VOI Volume of Interest

List of Tables

List of Figures

Chapter 1

Introduction

Cancer treatment with radiotherapy requires image information of the patient's anatomy that can be obtained using image techniques such as X-ray Computed Tomography (CT) and Magnetic Resonance Imaging (MRI). The gold standard for radiotherapy treatment planning (RTP) is CT because CT images offer high spatial resolution, enabling patient positioning during treatments, and can be easily correlated with tissue electron densities, necessary for accurate radiation dose calculations. Despite having an accurate dose-calculation module being an essential element of radiotherapy treatment planning, accurate and reliable tumour localization during treatment is of key importance to ensure an optimal outcome of high precision radiation therapy. Currently, available in-room imaging technologies for tumour localization based on x-ray imaging can only provide very low contrast images for many clinical indications such that the tumour is very poorly visualized. So, the main arguments for integrating MRI into the radiotherapy workflow are the superior soft tissue contrast offered by Magnetic Resonance (MR) images providing a gain in accuracy in target volume definition [1],[2] and the avoidance of imaging dose. Therefore, it's a common practice to acquire both CT and MR images of the patient, using MR data to define the tumour volume, CT data to plan and optimize the treatment and image registration to find a spatial relationship between the two images. However, there are essential concerns with this approach that are related to the fact that MRI-CT workflow is heavily dependent on the quality of the image registration procedure – errors in the alignment of both images in treatment planning stage propagate as a systematic geometric error throughout the entire treatment period [3],[4],[5] - and an increase in cost and workload to the clinicians when using two different image modalities. A natural follow up workflow proposal should be replacing CT or CT/MRI based radiotherapy for an MRI-only approach, where only MRI is used in all steps of the treatment planning. The use of MRI in radiotherapy however places certain demands on the imaging procedure, which are of less importance in the diagnostic MRI setting [6]. The geometric representation of the patient during planning and treatment should be precise, and so the patient needs to be imaged in the same position and using the same fixation devices as during treatment. Finally, there must be an accurate method to derive CT equivalent data from the MR data (referred to as substitute CT or synthetic CT or pseudo CT) to be able to perform dose calculations and patient positioning in the same way as it is done when using a real CT image.

In this thesis, we propose to evaluate two of the most promising MRI calibration approaches for the generation of synthetic CT's (sCT): The Manual Bulk Density Assignment (sCT_{bda}) and the Multi Atlas Registration (sCT_a) schemes. These approaches were evaluated on patient data sets for which CT and MR images, acquired at the same day and under the same conditions, exist for head and neck (H&N) and prostate sites. Clinical Volumetric Modulated Arc Therapy (VMAT) plans for the H&N patients and Intensity Modulated Radiation Therapy (IMRT) plans for the prostate patients were re-calculated on both sCT_{bda} and sCT_a generated. A dosimet-

ric evaluation using the clinical original contours, including the use of Dose Difference (DD), Gamma Analysis and Dose Volume Histograms (DVH), was performed for dose comparisons between plans re-calculated on the sCT and calculated on the real planning CT. Also, a geometric evaluation was carried out in which the original clinical contours defined on the planning CT and the delineations/segmentations on the MRI and sCT_a were evaluated individually in terms of shape, position and volume and also using the Dice Similarity Coefficient (DSC). Therefore, the principal aim of this project was to investigate if a MRI-calibration could be established without prior CT information and by a better fundamental understanding of the MR signal itself to test the feasibility of implementing an accurate, fast and automatic MRI-only based RTP into clinic.

The next generation of radiation therapy treatment machines will then likely be related with the MR-LINAC device. This device combines a linear accelerator (LINAC) with an MRI scanner enabling real-time MR imaging of the patient directly prior to or even during treatment [7]. Besides the benefits that the use of the MR-LINAC could bring to the radiotherapy planning and treatment system, there is currently one major problem with the use of this device related to the occurrence of dosimetric effects during treatment delivery due to the existing strong MR field [8]. To accurately estimate them, a precise knowledge of the patient geometry is required and so in this work it was also tested if the sCT are accurate enough to simulate these dosimetric effects for H&N patients.

This dissertation describes the work performed in the Institute of Cancer Research (ICR) London during 6 months and is organized in 5 Chapters in each information about the feasibility of implementing an MRI-only RTP is presented. Chapter 2 provides background information about radiotherapy treatment planning, CT and MR image modalities, different approaches to derive a sCT and about technical challenges of the use of the MR-LINAC. Chapter 3 describes the data, software and methods used in this work. Chapter 4 presents the relevant results obtained and also the discussion of the same is given. Finally, Chapter 5 summarizes the main conclusions and possible future work.

Chapter 2

Background

2.1 Radiotherapy

Radiation therapy, also referred to as radiotherapy, is one of the three principal modalities used in treatment of malignant disease (cancer), the other two being surgery and chemotherapy. The aim of a radiotherapy treatment (RT) is to deliver the maximum dose to the cancer cells, damaging its DNA, while minimizing the dose to the surrounding healthy tissue. The RT could be given internally, using implants such as radioactive metal wires and seeds, and externally, being the most common the use of high energy X-ray beams such as photon beams. For the external radiotherapy different delivering methods have been used [9]. Conformal Radiotherapy (CFRT) is a common type of external radiotherapy that aims to exploit the potential biological improvements consequent on better spatial localization of high dose volume [10]. In CFRT the prescription dose is shaped closely around the tumour target while at the same time the dose given to specified organs at risk (OAR) is maintain below their tolerance dose. Dose delivery techniques range from the use of standard regular and uniform coplanar beams to intensity-modulated non-coplanar beams produced with multileaf collimators (MLCs).

2.1.1 Intensity Modulated Radiation Therapy

IMRT is currently the most advanced form of CFRT [9]. While in traditional CFRT the outline geometrical shape of each beam can be controlled the fluence is uniform across the field. IMRT adds the intensity modulation to CFRT combining geometrical and fluence shaping to improve target dose homogeneity and spare OAR (Figure 2.1) [11].

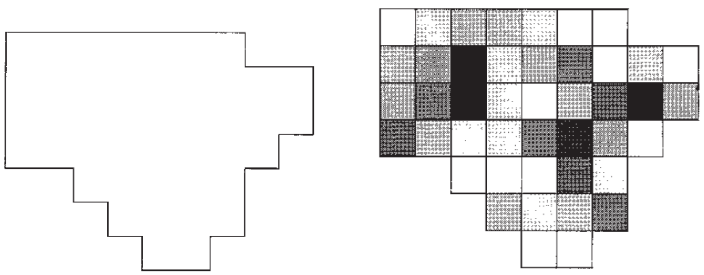

(a) (b)

Figure 2.1: Illustration of the two major classes of CFRT: (a) CFRT using simple geometric field-shaping alone (b) using intensity modulation (IMRT) across this geometric field-shape. The grey levels reflect the intensity value with bright higher than dark [11].

It relies on inverse treatment planning (ITP) for determination of the required intensity modulated beam maps, generally for a fixed number of beams positions, and on 3D multi-modality imaging to define the target volumes. This intensity modulation proves to be especially useful when the target volume has a concavity in its surface and/or when the target is situated right next to OARs [10].

2.1.2 Volumetric Modulated Arc Therapy

VMAT is a new available method for delivering radiation. VMAT delivers intensity modulated beams by means of one or more gantry arcs with continuously varying gantry speed, MLC leaf position, beam aperture and dose rate [12],[13]. Arching the gantry around the patient enables delivering the dose to the patient in all directions in a short period of time providing high quality dose distributions including improvement of dose conformity and normal tissue sparing.

2.2 Radiotherapy Planning Process

To design and deliver the best possible therapy, a wide variety of steps have to be undertaken. These include tumour and normal tissue delineation, treatment planning and evaluation, dose prescription and delivery.

The treatment delivery is divided into fractions where the patient receives a small amount of radiation in a given period until the total prescribed dose is reached. This is done to optimize the therapeutic ratio which is characterized by the maximal tumour control and minimal damage to healthy tissue [14]. In Royal Marsden Hospital (RMH) London, patients are treated with IMRT and VMAT plans and the radiation is administrated in 30 daily planned fractions for a total dose of 65 Gy for H&N patients and generally in 20 daily planned fractions for a total of 67 Gy for prostate patients or even 37 planned fractions for a dose prescription of 74 Gy. Since RT is divided into several fractions it's essential to assure treatment delivery reproducibility in each session. Thus, the patient needs to be positioned in the exact same position during image acquisition and subsequent RT.

2.2.1 Patient Treatment Position and Immobilization Devices

The proposed treatment position of the patient is determined prior to the planning process and an immobilization device is fabricated to reproduce the patient position over treatment. Fixation equipment such as a support for the hips and the legs is used for prostate patients while thermoplastic mask attached to the treatment table to fixate the head is used for H&N patients. Moreover, markers are placed on the patient's skin and the immobilization device to serve as fiducial marks for traceability, alignment and verification of the treatment set-up.

2.2.2 Image Acquisition and Registration

CT is used as primary source of image data to plan the treatment. When using other images modalities in addition to CT, such as MRI, the set-up patient position during acquisition must be maintained in order to perform accurate registration of both images.
Image Registration is the process where two images of the same scene taken at different times, which could be of the same modality or not, are overlaid [15]. In here, the planning CT is used as reference image while MRI is used as floating image. The spatial transformation will then warp

the points in the floating image with the correspondence points in the reference image having as a final result the floating image in the reference image coordinate system [16]. The spatial transformation applied could be categorized into rigid, affine and non-rigid transformation.

Most medical image registration algorithms assume that the spatial transformation is 'rigid body'. Rigid-body transformations consist of only rotations and translations maintaining all distances unchanged [17]. As bones are rigid at the resolution of radiological images, rigid body registration is widely used in medical applications where the structures of interest are either bone or are enclosed in bone [16]. The rigid registration could be applied using a geometric or an intensity based approach. In the geometric approach, landmarks such as points, curves and surfaces are defined in the reference and floating images and a correspondence between them is found. In the intensity based approach, a match of intensity patterns using mathematical or statistic criteria is done considering all image voxels in the process.

The affine registration is widely used to provide alignment of different subjects or when scale changes in images field of views (FOV) are expected. It is performed using rigid body parameters however introducing additional degrees of freedom by allowing for anisotropic scaling and skews [16]. This means that after performing an affine transformation all points, straight lines and planes are preserved however angles between lines and distance between points are not necessarily preserved. A rigid body transformation can usually be considered as a special case of affine, in which the scaling values are all unity and the skews are all zero [16].

When the aim is to tackle more challenging problems as for instance aligning images that are from different modalities and aligning organs that deform or move, using registration transformations with more degrees of freedom than the affine are required. Non-rigid body registration or deformable image registration (DIR) is used instead. The spatial transformation can be regarded now as a deformation field that denotes the displacement vector at each voxel in the floating image desired to align it with the corresponding voxel location in the reference image [16]. Non-rigid registration is based on non-rigid stretching where the final registered image has the same internal structure of the reference image but the intensity values of the floating one [18]. When performing DIR, reference and floating images are usually previously rigidly registered to each other to have a good starting point for the algorithm.

In RT it's common practice to acquire both CT and MR images of the patient. The concepts of CT and MR imaging will be explained in more detail in section 2.3. The registration between these two image modalities is a critical step as it will introduce an error that is generated by the use of different contrast images and due to time difference between scans acquisitions, which may result in the occurrence of small anatomical changes [15]. In many anatomical locations, tumours are relatively free to move with respect to the surrounding bone anatomy, and therefore, registrations should be focused on soft tissue. The reason of soft tissue registrations between CT and MRI are associated with substantial uncertainties is exactly the same reason as to why we need MR data to begin with. Additionally, imperfect patient repositioning may occur when the patient has to shift from one scanner to the other, introducing a systematic error that will be present in all treatment fractions.

After getting the planning CT, treatment planning stage takes approximately 2 weeks and it consists on: delineation of the target volume and OAR (see section 2.2.3), selection of the treatment plan (e.g beam energy, number and direction), optimization of the plan with assessment of DVH and others and quality assurance (QA).

2.2.3 Definition of Target Volumes and Organs at Risk

In order to be able to plan a radiation treatment, the relevant volumes of interest need to be "visible" to the planner and so delineation of the target volume and OAR is typically done by a physician. Generally, the image data is displayed and the contours are drawn manually slice-by-slice. However, for some structures such as external skin surface, which involves high contrast air-tissue interfaces, and also bone, which has a high contrast bone-tissue interface, an automatic threshold feature extraction might be employed [19].

The ICRU reports 50 [20] and 62 [21] defines several target and critical structure volumes that provide a basis for comparison of treatment outcomes, such as: gross target volume (GTV), clinical target volume (CTV), internal target volume (ITV), planning target volume (PTV) and OAR (Figure 2.2).

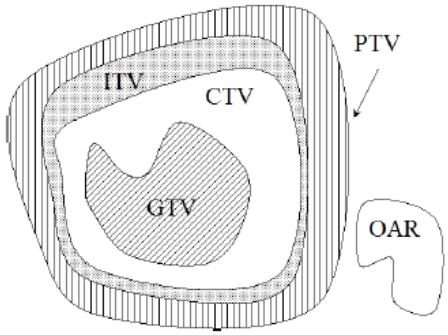

Figure 2.2: Graphical representation of the volumes-of-interest in radiotherapy, as defined by the ICRU 50 and 62 reports [9].

Accordingly to ICRU Report 50 the GTV is "the gross palpable or visible/demonstrable extent and location of malignant growth". The CTV is "the tissue volume that contains a demonstrable GTV and/or sub-clinical microscopic malignant disease" and is usually stated as a fixed or variable margin around the GTV [9]. The ITV is denoted by CTV plus an internal margin added to account variations in size and position of the CTV relative to the patient's reference frame due to e.g breathing and organ motion. The PTV is "a geometrical concept, and it is defined to select appropriate beam arrangements, taking into consideration the net effect of all possible geometrical variations, in order to ensure that the prescribed dose is actually absorbed in the CTV". This contour includes the ITV and an additional margin given for set-up uncertainties and intra treatment variations [9]. OARs are critical normal tissue structures which might be significantly damaged by the radiation such as the brainstem, the spinal cord and the parotid glands for H&N patients and the bladder, the rectum, the right and left femur head for prostate patients.

2.2.4 Treatment Planning, Implementation and Delivery

The treatment planning includes defining the beam geometry (e.g: gantry, couch angles, weight) and field apertures to produce multiple cross-firing beams that concentrate dose within the target. Tumour requirements, such as the desired dose prescribed to the target volume and the acceptable degree of dose inhomogeneity within it, are taken into account to achieve acceptable target coverage [19].

Concerning to the dose prescription, it's common practice to prescribe the dose to the PTV being however the dose given to the CTV what matters clinically. Regarding to the ICRU 50 [20] report the following considerations have to be full filled:

1. Dose has to be delivered to a specific point within the tumour (e.g isocenter);
2. At least 95% of the prescription dose has to be delivered to the entire PTV;
3. The total prescription dose has to be delivered to at least 95% of the PTV volume.

To obtain dose homogeneity within the target volume the following restrictions have to be met:

1. A minimum of 95% and a maximum of 107% of the prescribed dose has to be delivered to the PTV;
2. The standard deviation of the dose delivered to the PTV should be equal or smaller than 4%.

The requirements on OARs are almost always stated as constraints and are responsible for limiting the maximum dose to the target volume. After the beam geometry is designed, the dose distribution is calculated and evaluated (see section 2.2.5). After the plan is optimized and approved by a clinician and before delivering it to the patient, all the set-up is verified. First, to verify patient's position, digitally reconstructed radiographs (DRR) generated by the treatment planning system (TPS) from the CT are compared to radiographs acquired at the LINAC. If there is an acceptable deviation between both images the treatment may proceed. To ensure the validity and accuracy of the approved plan, patient specific QA is performed. This will comprise isocenter placement check on the LINAC, equipment performance, beam parameter settings among others [22].

2.2.5 Dosimetric Analysis

2.2.5.1 Dose Volume Histogram

DVH summarize the information contained in a 3D dose distribution in a 2D graphic display allowing the observer to know the total dose that a specified volume receives [23]. There are two variants of DVHs: differential and cumulative DVHs [19].

The calculation of the DVH involves the division of the whole structure volume into smaller volume elements - voxels - and calculating the dose at the centre of each voxel. The differential DVH sums the number of voxels with an average dose within a given range and plots the resulting volume as a function of dose [9] (Figure 2.3). The cumulative DVH plots the volume or percentage volume that receives at least a specific dose [9]. Then, all cumulative DVH plots start at 100% of the volume for 0 Gy, since all of the volume receives at least no dose. The cumulative DVH is found to be the most used in RTP as a tool for dose summarization particularly when plans must be compared and it will be referred as DVH from now on.

For dose comparison between different plans special DVH points are usually chosen in accordance with recommendations from the ICRU Report 83 [24]. For PTV and CTV the following DVH points are generally used:

1. D98%: Minimum absorbed dose that covers 98% of the volume;

2. D50%: Absorbed dose received by 50% of the volume or median absorbed dose. D50% describes the most uniform absorbed dose since the steepest slope in the DVH is often close to the median;

3. D2%: Minimum absorbed dose that covers 2% of the volume. D2% is usually clinically used as a good indication of the maximum absorbed dose in the target volume;

4. Dmean: Mean absorbed dose by the target volume.

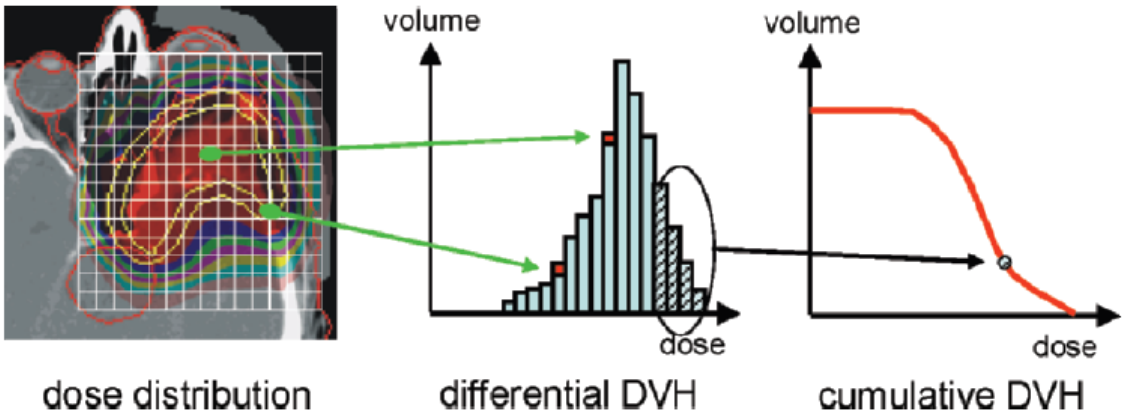

Figure 2.3: Illustration of how differential and cumulative DVHs are constructed. The two voxels identified in the dose distribution (left) represents voxels that receives a lower dose (the one on the edge) and a high dose (the one on the centre). Therefore, they are respectively represented in the differential DVH in a low and high dose bin accordingly to the dose received by each voxel. In the cumulative DVH the total volume of the structure which receives a dose greater or equal to the dose bin indicated in the differential DVH is represented [19].

While D98%, D50% and D2% can be directly read from the DVH, Dmean has to be calculated by the TPS. For OAR the recommended DVH points differ according to the classification of the organs into serial or into parallel. Parallel OARs are organs that tolerate very high dose values in small sub-volumes if the rest of the body is spared. For these organs the use of D50% or Dmean is recommended. Serial OARs are organs which high doses are harmful even if they are limited to small volumes. For these volumes the use of D2% is suggested.

Besides being a useful tool for treatment planning, the main drawback of the DVHs is the loss of spatial information [9].

2.2.5.2 Absolute and Relative Dose Difference

Absolute and Relative DD is one of the most useful tools in RTP to evaluate two different dose distributions. DD employs that both dose distributions are in the same coordinates system and have exactly the same size. Then, it consists on the difference between dose values on the same position in both dose sets through voxel by voxel value subtraction. In Absolute DD the final value is shown in radiation dose units - Gy - and in Relative DD the final value is represented by a percentage usually related to the maximum dose.

2.2.5.3 Distance to Agreement

Van Dyk developed the concept of Distance to Agreement (DTA) [25] which consists in measuring the closest distance between a point in the reference dose distribution r_r to a point in the evaluated dose distribution r_c where the dose value is the same.

$$DTA(\vec{r}_r) = min|\vec{r}_c - \vec{r}_r| \tag{2.1}$$

The reference dose distribution is the one whereby the DTA is computed point by point, while the evaluated dose distribution is the one queried for the closest approach of the specific dose value [26]. A threshold value of Δd is typically considered as acceptance criteria such that if the DTA at the comparison point is greater than Δd the test fails and if it's lower the opposite occurs.

2.2.5.4 Gamma Analysis

The most straightforward method to compare two dose distributions is to take the numerical difference between them. However, there are practical limitations that might arise if the dose distributions are not precisely aligned. If there is a spatial error associated with the measurement, even for a relatively small one, the dose distribution differences with steep dose gradients will be artificially enhanced by the spatial offset of the two dose distributions [26].

The gamma method was designed by Low et al. [27] to compare two dose distributions - one is used as reference (D_r) and the other is used for evaluation (D_c) - accounting for dose and spatial differences between them. Thus, in this method DD and DTA test criteria are used to determine if the compared dose points passes or fails the dose distribution comparison test.

The acceptance criteria are denoted by ΔD_M (measured in %) for DD and Δd_M (measured in mm) for DTA [28]. The investigation is performed for each point $\vec{r}_r$ in the reference dose distribution in order to find the most similar point $\vec{r}_c$ in the evaluated dose distribution. Hence, this method provides a numerical quality index - referred to as gamma value or gamma index - that serves as a measure of disagreement in regions that fail the acceptance criteria and indicates the calculation quality in regions that passes [28].

The gamma test for 2D dose distributions is denoted by an ellipsoid surface (Figure 2.4) representing the acceptance criteria for dose and spatial tolerance with the centre located at $\vec{r}_r$:

$$\Gamma(\vec{r}_r, \vec{r}_c) = \sqrt{\frac{r^2(\vec{r}_r, \vec{r}_c)}{\Delta d_M^2} + \frac{\delta^2(\vec{r}_r, \vec{r}_c)}{\Delta D_M^2}} \tag{2.2}$$

Where $r(\vec{r}_r, \vec{r}_c)$ is the distance between the reference and evaluated point as it follows $r(\vec{r}_r, \vec{r}_c) = |\vec{r}_c - \vec{r}_r|$ and $\delta(\vec{r}_r, \vec{r}_c)$ is the dose difference between the evaluation dose D_c at the position $\vec{r}_c$ relative to the reference dose D_r at the position $\vec{r}_r$ as it follows $\delta(\vec{r}_r, \vec{r}_c) = D_c(\vec{r}_c) - D_r(\vec{r}_r)$.

The gamma index is calculated by finding the minimum value of $\Gamma(\vec{r}_r, \vec{r}_c)$:

$$\gamma(\vec{r}_r) = min\{\Gamma(\vec{r}_r, \vec{r}_c)\} \forall \{\vec{r}_c\} \tag{2.3}$$

For the compared distribution to match, the gamma value for the reference dose in r_r has to be smaller or equal than 1. If it's greater the evaluated point is not within the specified acceptance criteria.

It's most common to use a global criterion for DD, where ΔD_M is constant for all combination of points evaluated and its value is calculated regarding to the maximum dose. However, a harder constraint could be applied when using a local criterion for DD, where ΔD_M is not constant and its value is calculated regarding to the dose at the reference point.

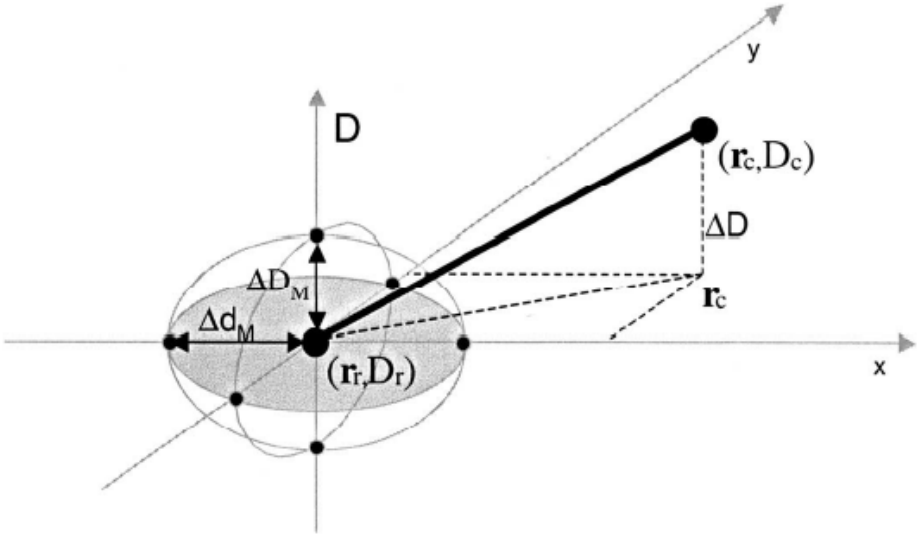

Figure 2.4: Schematic representation of the theoretical concept of the gamma evaluation method for 2D dose distributions. The reference and evaluation dose distributions are denoted by (r_r,D_r) and (r_c,D_c), respectively. The criteria defining the ellipsoid of acceptance is denoted by the dose difference tolerance ΔD_M (in the z axis) and the maximal distance to agreement Δd_M (in the x-y axis). In this example the point r_c fails the critera (outside the ellipsoid) [28].

2.3 Image Modalities in Radiotherapy

2.3.1 Computed Tomography

In CT, transaxial X-ray projections are computed to create cross-sectional images of the human body. In a CT scanner, the X-ray tube rotates around the body, while the beams pass through the patient at different angles. The intensity of the attenuated beams is measured and converted into electric signals with detectors placed opposite to the X-ray tube. After being processed, these signals are transformed into attenuation values which consists of the CT raw data [29]. The raw data is then reconstructed into an image using a CT reconstruction algorithm, being the *filtered back-projection* reconstruction algorithm the most used for clinical practice [30]. This algorithm basically works by reversing the acquisition steps and with it the attenuation values are assigned to each pixel in the image matrix. As the data from a large number of rays are back-projected to the image matrix adding the values of each projection to each voxel, a better discrimination of areas with high as well as low attenuation properties is reinforced [30]. As a final result, the reconstructed CT image is a grey tone image where each pixel represents a scanned voxel with a specific Hounsfield Unit (HU) which describes the degree of attenuation relative to water [31]:

$$\text{HU(i,j)} = 1000 \times \frac{\mu(i,j) - \mu_w}{\mu_w} \tag{2.4}$$

Where $\mu(i,j)$ represents the linear attenuation coefficient of the voxel ij and μ_w is the linear attenuation coefficient for water at the same spectrum of photon energies.

The HU is a dimensionless measure that describes the absorption properties of the tissue. Thus, different HU values are responsible of creating different contrasts in a CT image [31]. So in general, bone appears bright as it has the highest HU values (+1000HU), air is usually black as it has the smallest HU values (-1000HU) and soft tissue appears in different shades of grey [19]. The similarity in the HU for different types of soft tissue makes it difficult to differentiate between tumour and healthy tissue (Figure 2.5).

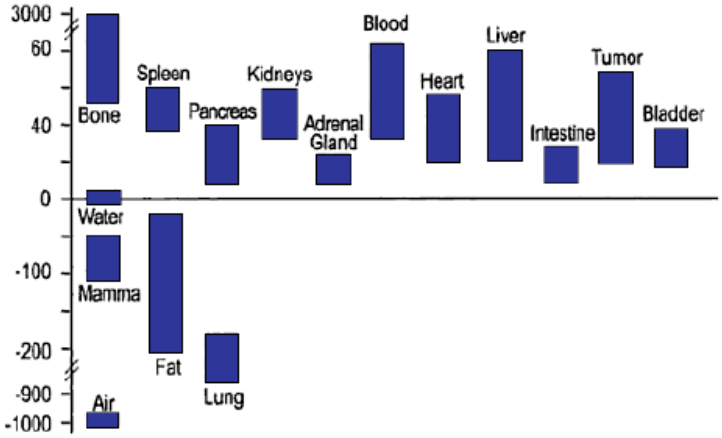

Figure 2.5: An overview of HUs for human tissues. y scale is in HU [32].

The accuracy of dose calculations based on CT data is partly determined by the precision of HUs to relative electron densities conversion. The relationship between HUs and relative electronic densities is called calibration curve [33].

2.3.2 Magnetic Resonance Imaging

MRI is remarkably known for giving excellent images of soft tissue. This is due to the fact that MRI makes use of the circumstance that approximately 70% to 90% of the human body consists of water [34] and also takes advantage of the physical properties of hydrogen, which as part of water and lipids makes up to 75–80% of the human body [34].

Generically, MR is based upon the interaction between an applied magnetic field and a nucleus that possesses spin[1]. The required MR image is obtained with a MR pulse sequence that consists usually of 90°radio frequency (RF) pulses which are applied with controlled duration and timings [34] and are responsible for causing the spin excitation. The signal from the nuclei of the hydrogen atoms generated by its maximal transverse magnetization is then used for image generation [35]. After the nuclei being flipped by a RF pulse, the MR signal will fade due to two independent processes that will cause the reduction of the magnetization and the return to

[1]Intrinsic property of nearly all elementary particles that makes the same rotates around its axis like a spinning top

the stable state: the spin lattice interaction known as the T1 relaxation time and the spin-spin interaction known as the T2 relaxation time.

T1 is the relaxation time for the recovery of magnetization along the z axis in where the spins dissipate energy to their surroundings [36] and T2 denotes the process of transverse relaxation characterized by an energy transfer between spins as a result of local changes in the magnetic field [35]. Transverse relaxation is the decay of transverse magnetization as a result of the loss of phase coherence of the individual spins which could happen in two ways: by energy transfer between spins, which occur with a time constant T2 as mentioned before, and by time independent inhomogeneities of the external magnetic field. Both occur at a time constant shorter than T2 and denoted by $T2^*$. $T2^*$ is then a composite relaxation time which includes T2, inhomogeneities due to main fields and tissue susceptibility and diffusion of protons [34]. Most of the inhomogeneities that produce the $T2^*$ effects occur at tissue boundaries and the loss of the MR signal due to $T2^*$ effects is called free induction decay (FID).

So, MR intensities can be correlated with proton densities, which are related to the number of hydrogen atoms in a volume, and tissue relaxation properties rather than with the attenuation properties in the tissues such as in CT. The density and relaxation time of protons in different tissues is used to create the required contrast and signal intensity for diagnostic purpose in MR images by changes in the Echo Time (TE) and the Repetition Time (TR) [34]. TR is the time between two excitation pulses in a sequence while TE is the interval between the application of the excitation pulse and the measurement of the MR signal [35]. The contrasts are created based on a linear look up table, where magnitudes of the measured signals are converted to a grey tone.

In T2-weighted images, the TR and TE are both long and tissues with long T2, such as fluids, give the highest signal intensities, producing a bright appearance. T2 images are often called as 'pathology images' as the abnormal fluids appear bright against the dark normal tissue [34]. In T1-weighted images, long T1 tissues give the weakest signal and appear dark, as fluids, and bright pixels are associated with short T1s, as fat based tissues. T1 images are often called anatomy scans as they display clearly the boundaries between different tissues. Using short TR and TE times the T1 differences between tissues will be enhanced [34].

As for CT, MRI generates cross-sectional images of the human body [34]. The RF pulse is therefore delivered only to the slice that is needed to be imaged. Slice position will be selected according to the centre frequency of the applied RF pulse [35]. After selecting slice thickness and position, spatial position of the MR signal needs to be identified which is accomplished using spatial encoding. Spatial encoding comprises two steps, phase encoding and frequency encoding, and requires the application of additional gradients that will alter the magnetic field strength along the y and x axis enabling unique spatial identification of each voxel. The raw data space which is used to store the digitized MR signals during data acquisition is called k-space [34]. k-space has two axes with the horizontal axis (k_x) representing the frequency information and the vertical axis (k_y) the phase information [35]. The final MR image will be created from the raw data by applying the 2D-Fourier Transformation to the k-space after the scan is over.

2.4 State of the Art for Building an MRI-only Radiotherapy Workflow

Currently, MRI scans are used in the treatment planning for target delineation as they offer superior soft tissue contrast while CT scans are used to plan the treatment as they offer tissue electron density information enabling dose calculations and high spatial accuracy allowing the generation of reference images to be used for patient positioning. However, for the use of the MRI scans in the treatment planning they must be registered to the corresponding patient's CT scans, allowing any manual contouring from the MRI to be mapped across the planning CT. This step is required as MRI scans are acquired by a process completely different from that of CT as it was explained before in section 2.3. This appears to be an optimal workflow at an initial glance as the benefits of both CT and MRI are used to their full extent. Although, there is a central problem with this approach related to the errors in the alignment of the MR and CT images as explained before in section 2.2.2. The elimination of registration errors between MRI and CT scans, the less exposure to ionizing radiation, the reduction in imaging costs and the reduction of extra margins added to account for delineation uncertainties had increase the pursuit of a MRI based treatment planning in the last few years. However, several challenges must be overcome to fully establish the MRI based treatment planning such as:

1. Patient aperture, couch and RF coils needs to be re-designed to allow the patient to be at the exact same position during planning and treatment delivery stages [37];
2. The distortions in MR images induced by system hardware or patient specific magnetic susceptibility needs to be avoided or corrected [37, 38, 39];
3. Poor bone imaging with traditional MR sequences as cortical bone is reflected as regions of very low intensity signal due to its short T2 relaxation time which makes the separation of bone and air extremely difficult since air produces the same very low or zero intensity signal [40, 41];
4. Lack of electron density information for dose calculations.

Trying to solve the last problem, currently exist two families of algorithms for transformation of MR data into CT like data: The Anatomy and the Voxel based Methods. The Anatomy Method generally uses DIR between a library of MR reference images and a new patient MRI to warp a reference CT to match the anatomy of the new patient data [37], [42, 43, 44, 45, 46, 47]. The Voxel based Method could be divided in two types. The first one involves a direct characterization of individual voxels into different tissue classes by manual segmentation followed by bulk assignments of electron densities values [48, 49, 50]. The second one comprises a direct conversion of MRI voxels values to HU or electron density values by introducing a prior correlation between MRI and CT [51, 52, 53, 54, 55, 56].

2.4.1 Anatomy Methods

The Anatomy Method, could be divided in two main approaches: The Atlas Registration scheme [37], [42, 43, 44], [46] and the Patch based method [47].

The Atlas Registration scheme (Figure 2.6) uses information from the whole image and is essentially made of a 2 stage approach: average atlas construction and conversion of a new MRI to a labelled sCT.

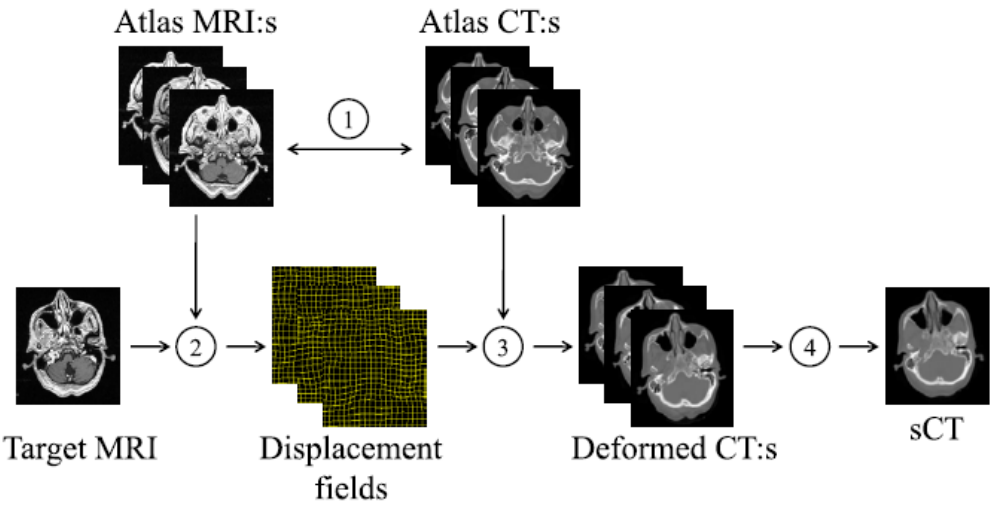

Figure 2.6: Outline of the Atlas Registration based Method: (1) MR and CT image pairs are collected and rigidly registered, (2) each atlas MRI is registered to the target MRI, (3) the resulting transformation is applied to the corresponding CTs and (4) the set of deformed CTs are fused to a single sCT [42].

Atlas construction stage is usually divided in three steps, which are:

1. In the first step, every CT and MR image from the atlas dataset are aligned via linear rigid-body or affine registration to enable intra-subject alignment and producing multiple conjugated CT/MR atlas image pairs [37], [43].

2. The second step involves mapping the MRI of a new patient to all MR atlas images using rigid, affine and non-rigid transformations enabling inter-subject alignment to create the MRI atlas [37], [42].

3. To calculate dose, a sCT scan is created automatically with electron densities mapped to tissues by means of a CT atlas [45]. This step consists in a CT atlas generation where the transformation matrices and deformation fields used in the MRI atlas generation are also applied to the result of each CT/MR image registration to build the CT atlas [37], [42].

The HU value for each voxel in sCT could be obtained using a simple arithmetic mean process [37], [43, 44], a weighted average based on similarity measures [46] or even by using pattern recognition with Gaussian process (PRGP) [37], [44].

In the arithmetic mean process, the sCT intensity (μ) of a voxel at the position x_o is simply the mean of those at the same location in all deformed CT images in the CT atlas [37]:

$$\mu(x_o) = \frac{1}{Na} \times \sum_{i=1}^{N_a} y_i(x_o) \tag{2.5}$$

Where N_a is the number of atlases and y_i the HU value in all CT images in the atlas.

In the weighted average based on similarity measures method the target MRI is locally matched with the MRI atlas database using both DIR and local image similarity measures such as convolution-based fast local normalized correlation coefficient (LNCC) - explained later in section 3.2.1.2 - and local sum of squares differences (NSSD) - explained later in section 3.2.1.3. Similarity results at each voxel are ranked across all MR images in the atlas according to the

quality of the registration. The ranks in each n^{th} subject atlas and voxel $\vec{v}$, $R_{n\vec{v}}$, are then converted to weights, $W_{n\vec{v}}$. Better registration results have a larger weight by applying a negative exponential decay function as it follows [46]:

$$W_{n\vec{v}} = e^{-\beta \times R_{n\vec{v}}} \tag{2.6}$$

Where β is a constant weighting factor. The weights $W_{n\vec{v}}$ are used to reconstruct the target sCT image I^{sCT} at each voxel $\vec{v}$ using the following weighted averaging equation:

$$I_{\vec{v}}^{sCT} = \frac{\sum_{n=1}^{N_a} W_{n\vec{v}} \times J_{n\vec{v}}^{CT}}{\sum_{n=1}^{N_a} W_{n\vec{v}}} \tag{2.7}$$

Where $J_{n\vec{v}}^{CT}$ is the atlas CT image from subject n at voxel $\vec{v}$.

The intensity of each voxel predicted by PRGP is also a weighted average of voxels from the deformed CT atlas where the voxel at the same location and also the neighboring ones will contribute to the prediction [44]. The intensity of each voxel in each position, $\mu(x_o)$, in the final sCT is a linear function of [37]:

$$y = [y_1(x_o) \quad y_1(x_1) \quad ... \quad y_1(x_{N_n}) \quad ... \quad y_{N_a}(x_o) \quad y_{N_a}(x_1) \quad ... \quad y_{N_a}(x_{N_n})] \tag{2.8}$$

Where N_n is the number of neighbors and N_a the number of atlases. The weight assigned to each element of y will be determined by "patches" comparison between all MRIs in the atlas and the target MRI. A patch is defined to be a square matrix surrounding the voxel of interest (VOI). Then, PRGP gives a rule to combine $N_a \times (1 + N_n)$ CT numbers from (1+N_n) voxels (including the VOI and its neighbors) in each CT atlas image. A Gaussian process is defined by a mean function, m, and a covariance or kernel function, k [44]. The kernel function measures the degree of correlation or similarity between two patches as it is expected that similar MR patches translates highly correlated CT values. The training patches for prediction are usually extracted from the same slice only.

The sCT value for each voxel at a fixed position x_o is then given by:

$$\mu(x_o) = m(x_o) + kC^{-1} \times (y^T - m^T) \tag{2.9}$$

Where $m(x_o) = \frac{1}{Na} \times \sum_{i=1}^{N_a} y_i(x_j)$, j=0...$N_n$ and $k(p_i, p_j) = e^{\frac{-\|p_i - p_j\|^2}{2 \times \sigma_p^2}} \times e^{\frac{-\|x_i - x_j\|^2}{2 \times \sigma_x^2}}$ denotes the kernel with respect to the patches p_i at query position x_i in the patient MR image and p_j at query position x_j in the atlas MRI. σ_p^2, σ_x^2 and patch size are usually determined by cross validation.

As for all standard MR sequences the MRI intensity of each voxel does not give sufficient information to uniquely determine its tissue class and also as it's not possible to assume a one to one correspondence between patient and atlas image the use of the patch may add some more characteristic information about the typical pattern of the tissue structures. This may be particularly useful when distinguishing between bone and air because the intensity of the voxel alone is near zero in both cases, but the surrounding volume looks different for air and bone regions.

Finally, the Patch based method (Figure 2.7) is a singular case of the Anatomy Methods as it involves the use of a rigidly aligned CT-MRI atlas as a database but not the use of DIR. In here, 3D patches are extracted from the target MRI and a spatial local search is done to acquire the most intensity similar patches in all MRIs in the database [47]. The need of using DIR is here removed as the segmentation is driven mostly by patch resemblance.

The database will be made of patches extracted from the atlas MRIs centered on an arbitrary spatial location x, $P_s(x)$, and the CT value on position x of the corresponding rigidly aligned CT, $T_s(x)$. Using this database, an intensity based nearest neighbor search is performed using the following measure:

$$d(s,x) = \|P(y) - P_s(x)\|^2 \tag{2.10}$$

Being P(y) the patch at the target MRI. Then, the search consisted on finding the k database patches that minimize d(s,x) - $P_{s_k^{min}}(x_k^{min})$ - and storing the corresponding CT value in the atlas at the same spatial position as $T_{s_k^{min}}(x_k^{min})$. The sCT value at position y is then calculated using a weighted average as it follows:

$$sCT(y) = \frac{\sum_k w_k \times T_{s_k^{min}}(x_k^{min})}{\sum_k w_k} \tag{2.11}$$

Where the weights are denoted by w_k and calculated by:

$$w_k = exp\left(\frac{-d(s_k^{min}, x_k^{min})}{\min\limits_k \quad d(s_k^{min}, x_k^{min})}\right) \tag{2.12}$$

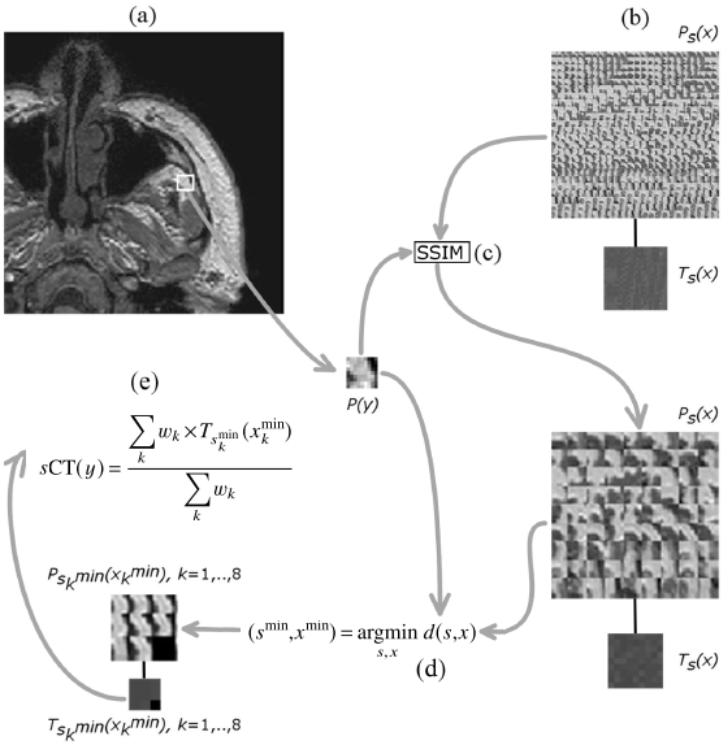

Figure 2.7: 2D patch based sCT prediction. (a) A patch , P(y), is extracted from the target MRI at position y. (b) A database of spatially close patches, $P_s(x)$, is stored with their corresponding CT value value, $T_s(x)$. (c) Structural similarity measure (SSIM) is used to discard highly dissimilar patches in the neighborhood. (d) Using this equation the 8 most similar database patches, $P_{s_k^{min}}(x_k^{min})$, and their CT values, $T_{s_k^{min}}(x_k^{min})$, are found from the database. (e) Using the weighted average equation the CT values, $T_{s_k^{min}}(x_k^{min})$, are combined to produce the final sCT value at position y [47].

2.4.2 Voxel based Methods

2.4.2.1 Manual Bulk Density Assignment

Applying bulk electron densities to the MRI involves overriding original pixel values with a single electron density value (Figure 2.8). Electron density values could be applied to an entire body region originating a homogeneous density assigned MRI or to specific contoured structure volumes creating a bulk heterogeneous density assigned MRI [57]. 3 sets of sCT with increasing level of heterogeneity are commonly generated [48], [50]:

1. MRI_w: External body contour outlined with water equivalent density assuming that all body is made of soft-tissue;

2. MRI_{w+b}: Bone segmentation is performed and bone specific electron density is applied to the contour while the remaining anatomy is defined to be of water equivalent density;

3. MRI_{w+b+a}: Bone and air segmentation are performed and bone and air electron density are applied to the contours while the rest of the body is defined to be of water equivalent density.

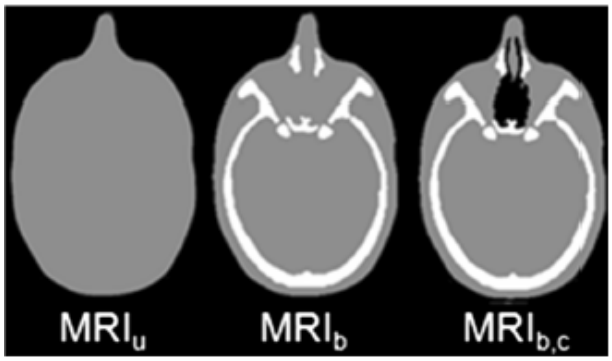

Figure 2.8: Schematization of different density corrected MRIs for H&N patients. MRI_u is representing a homogeneous density assigned MRI, MRI_b a bulk density assigned MRI considering bone as the only tissue class and finally $MRI_{b,c}$ is representing a bulk density assigned MRI including bone and air as tissue classes [48].

To improve the accuracy, it's preferable to segment as many tissue types as possible and assign them appropriate densities (eg. defining fat and white and grey matter for H&N patients) [57]. Unfortunately, such approach is not practical. A more realistic approach is to contour a limited number of tissues, whose segmentation can potentially be automated being MRI_{w+b+a} the minimum approach to achieve high dosimetric accuracy.

Bulk density geometries and OARs segmentation could be either performed on CT data and then copied to the MRI to control for potential variability in structure delineation or performed directly on MR data. Hence, CT and MR images are previously rigidly registered to each other.

To standardize comparisons between CT and MRI-alone treatment planning, it's necessary to validate the dosimetric accuracy of bulk density assignment using identical contours and so usually clinical structures segmentation relies on CT data. Once validated, the feasibility of MRI-based treatment planning will rest on the ability to delineate structures on the MRI alone. The same protocol applies to the delineation of the external body contour. However, it's more common that the external body is outlined separately in the MRI to include for possible effects of geometrical distortion [48]. When using the external contour from the MRI, differences in the delineation of the body may arise because of small variations in the CT and MR images set-up, such that the original clinical contours occasionally extended beyond the MRI body. To exclude the effects of body contour differences between CT and MRI, the external contours from both scans have to be matched and all internal contours cropped to the final external contour used [50].

2.4.2.2 Direct Voxelwise Conversion

Instead of applying manual bulk density for the segments outlined, improvements in dose distribution accuracy might be obtained by assuming a direct conversion of MRI values into HU adopting a patient specific tissue modelling by finding a prior correlation between MRI intensity signals and HU. Recently, the interest for this approach has been increasing significantly especially due to the development of ultrashort echo time (UTE) imaging.

UTE sequences were especially designed to visualize tissues with short T2. A variety of tissue components, such as tendons and ligaments [40], have short T2 relaxation time as their MR signal decays rapidly. As a result little or no signal is detectable by the time that conventional MR systems begin to operate in receive mode [58]. Therefore, they appear dark with virtually all pulse sequences routinely used in clinical MRI. In UTE imaging, the signal is sampled during the FID that is directly following the excitation and before the signal from these tissues has

vanished [59]. Thus, this pulse sequence uses TEs 10-200 times shorter than those normally used [58]. This short TE is produced by using a half RF pulse with radial mapping from the centre of k-space [41]. Cortical bone has an even shorter T2 time than these tissues caused by the lower water content of the same. Therefore, it was necessary to investigate the feasibility of visualizing cortical bone with this sequence.

Several groups proved that is possible to distinguish between air, which causes a signal void in both traditional and UTE sequences, and bone using UTE imaging. However, because UTE sequences samples FID the contrast in the images is controlled by $T2^*$ rather than T2 [53]. Therefore, the UTE approach leads to difficulties in distinguishing voxels with both short T2 and $T2^*$, such as cortical bone, from those with a long T2 combined with a short $T2^*$, such as interfaces between air and soft tissues [58]. To distinguish air-soft tissue interface signal from bone signal, additional information coming from the T1 relaxation time, which differs from both, and using different flip angles as complement of using different TE might increase the accuracy of tissue segmentation [53], [60]. So, implementing an MRI-only RTP based on UTE images it's not possible using only a single MR image. Therefore, it has been suggested to use UTE sequences with at least 2 or 3 different TEs [40, 53, 56, 61].

For the generation of sCT from the UTE sequences automatic segmentation via bulk density assignments [40], [61] or continuous model based conversion, [53, 54, 55, 56, 60], methods could be used. The last ones rely on statistical models, describing the relationship between the voxel intensities in MR and CT data.

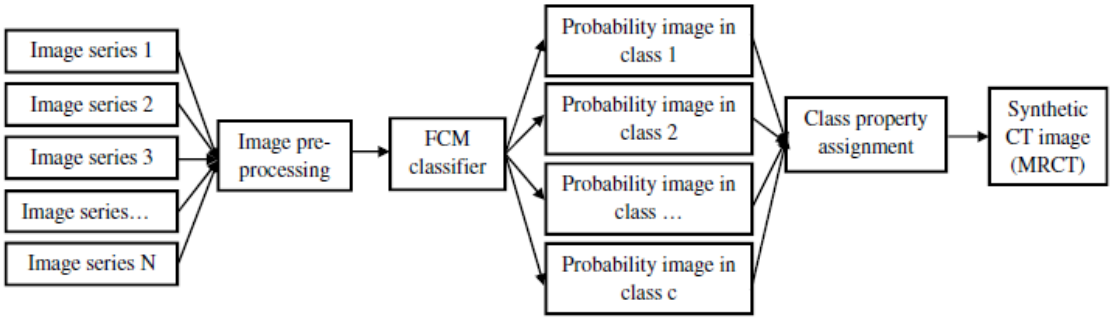

Figure 2.9: Overall scheme of using multiple MRI volumes to generate sCT trough probabilistic tissue classification achieved via fuzzy c-means (FCM) clustering [55].

The application of these statistical models involves using as database a set of CT and MR images co-registered to each other and resampled to the same image resolution. Tissue classes' differentiation is obtained with different types of MRIs, including UTE images. A joint distribution of the intensities in the CT and MR images is done using probabilistic tissue classification. For each image voxel a probability between 0 and 1 of belonging to one of the tissue classes defined is calculated. The sCT value of a voxel is then obtained by the product of the posterior probability of a voxel belonging to each one of the classes defined and the mean CT number of each class (or the specific electron density value attributed to the same). The final sCT value is obtained by summing the results across all classes. As a result, the probability weighted sum of the attenuation properties of each voxel yields an attenuation map capable of producing a sCT based entirely on MR information of a new patient (Figure 2.9). Gaussian mixture regression models [53],[60], high dimensional discriminant analysis [56] and fuzzy c-means clustering [55] have been showing good results as algorithms used for this probability tissue classification.

2.5 Image Guided Radiotherapy and the MR-LINAC

Image guided radiotherapy (IGRT) is a type of CFRT that aims to decrease the geometric uncertainties during the treatment, enabling the reduction of PTV margins and the dose given to the healthy tissue around the target, by means of image guidance. Techniques based on cone beam CT, ultrasound and implanted fiducial markers are some of the existing IGRT technology [62, 63, 64, 65]. The use of these techniques however introduces problems related to the limited visibility of the tumour itself and the absence of real intrafraction imaging [66]. MRI offers high soft tissue contrast for tumour definition and provides several imaging modalities for direct on-line motion imaging overcoming the problems faced when using other technologies as stated before.

Therefore, with the goal of real time MRI guidance, at the University Medical Center Utrecht was constructed an MR-LINAC which comprises a 6 MeV Elekta (Crawley,UK) accelerator mounted on a ring around a modified 1.5 T Philips Achieva (Best,Netherlands) MRI system [7]. The accelerator is located in a ring around the patient making the radiation beam travel through the closed bore MRI before reaching the patient (Figure 2.10). The principal aim of this system is to deliver the radiation dose with mm precision based on diagnostic quality MRIs enabling real-time MR imaging of the patient directly prior or even during treatment.

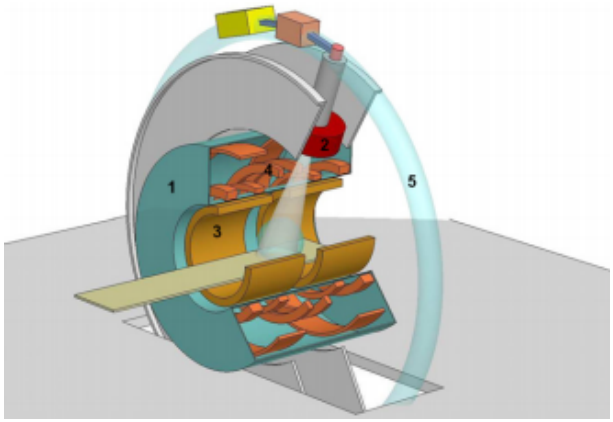

Figure 2.10: Sketch of a MRI accelerator concept: The 1.5T MRI scanner is shown in blue (1) while the 6 MeV accelerator (2) is located in a ring around the MRI [7].

Besides the benefits that the use of the MR-LINAC could bring to the RTP, both the radiation dosimetry and the geometrical accuracy of the MR images must be ensured. The treatments will be delivered to the patient located within a strong lateral magnetic field which will affect the dose distributions. The magnetic field dose effects can be divided in two types: the first is related to the fact that in homogeneous tissues, the point spread kernel for secondary electrons becomes asymmetrical culminating with a reduced build up distance and a shifted asymmetrical penumbra [67] (Figure 2.11). The second is related to the interaction of the magnetic field with the secondary electrons and it's called electron return effect (ERE) [8]. Because the ERE is much more pronounced than the reduced build-up distance and the asymmetrical penumbra shape of secondary electrons, only the ERE has been more intensively investigated.

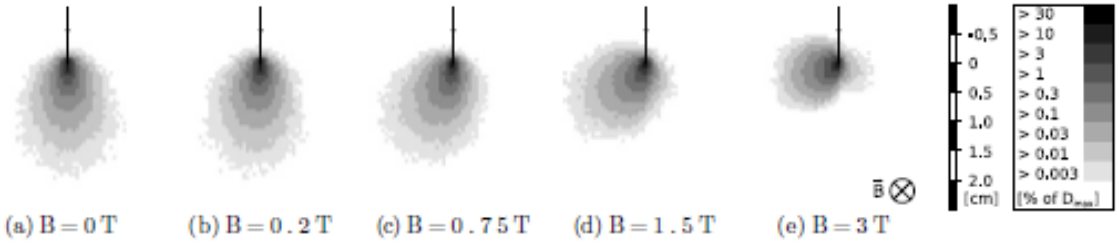

Figure 2.11: Monte Carlo calculated pointspread kernels for secondary electrons depending on the magnetic field strength B. A logarithmic grey value scaling is used [67].

Although the primary X-rays are unaffected, the magnetic field interaction with electrons, liberated by the interaction of the primary radiation with the tissue, generates a Lorentz force that will affect the electron path and thus all aspect of measuring and calculating the absorbed dose [8]. In the presence of a magnetic field, the trajectories of the electrons will be bent, describing a helix, and its induced curvature will depend on the electron energy and on the magnetic field strength [67] (Table 2.1).

Table 2.1: In vaccum electron trajectory radius (in mm), depending on the electron energy and magnetic field strength [67].

	Magnetic Field Strength			
Electron Energy (MeV)	**0.2T**	**0.75T**	**1.5T**	**3T**
0.5	14.5	3.9	1.9	1.0
1.0	23.7	6.3	3.2	1.6
1.5	32.4	8.6	4.3	2.2
2.0	41.0	10.9	5.5	2.7

Within the patient, the electrons will scatter from interaction to interaction, with curved trajectories in between. When reaching transitions to low density materials such as the surface and around internal air cavities, the ERE will be more pronounced as the arc-shaped trajectory of the electrons can be followed without any interaction, and so without the electrons loosing energy, culminating with them re-entering into the patient tissue. This will happen regardless of the exit angle of the electrons and will lead to a severe dose increase at those sites. Raaijmakers et al. [67] proved that for 5×5 cm^2 beams, the maximum ERE dose increase for a magnetic field B= 0.2; 0.75; 1.5 and 3T is respectively 20, 50, 40 and 20% relative to the maximum dose at B=0T. For 10×10 cm^2 beams these values are equal to 40, 52, 42 and 25%.

2.6 Previous Work

Different attempts in trying to implement an MRI-only radiotherapy workflow into clinic have been proposed in the last few years and were previously mentioned in section 2.4. The first method which accuracy was investigated was the Manual Bulk Density Assignment - section 2.4.2.1 - in a straightforward approach of assigning the entire patient anatomy with a single bulk density, usually water or a mixture of adipose and muscle tissue. Although drastic, this method yields acceptable dosimetric results and for intracranial and prostate volumes dosimetric errors are reported to be between 2% to 3% when compared to the real CT based dose calculations.

Korsholm et al. [48] showed that the difference for the median PTV coverage was $1.0 \pm 1.9\%$ for H&N patients and $1.3 \pm 1.4\%$ for prostate patients. In the same study when looking at OAR DVH points percentage difference the results were higher than the PTV coverage and for example the percentage difference of the mean dose given to the right and left parotid could arise to $-1.2 \pm 6.2\%$ and $1.7 \pm 7.4\%$, respectively for H&N patients. Kristensen et al. [68] also showed that with dose calculations based on MRI unit density the differences in the treatment isocenter dose have a mean value of $1.4 \pm 0.4\%$ for brain tumours. Similar results were stated in [50], [69, 70, 71].

The differences between plans can be mitigated by manually delineating tissue classes and assigning each class a different bulk density. Using this approach errors are reduced to approximately 1% for intracranial volumes and between 1% to 2% in prostate volumes. In Korsholm et al. study, when segmenting bone the difference in the median PTV coverage was reduced to $-0.0002 \pm 1.1\%$ for prostate patients and when segmenting bone and air to $-0.02 \pm 3.0\%$ for H&N patients. Also for Kristensen et al. study, the reduction on the mean difference in the isocenter dose point when segmenting bone was $0.4 \pm 0.3\%$. Similar results were obtained in [49, 50], [72].

Despite this method proves to be relatively accurate for dose calculations, it has not reached widespread clinical acceptance primarily because of the time consuming task of structure definition as bone cannot be automatically delineated using traditional MR sequences. Bone delineation it's necessary for obtaining dosimetric accuracy as bone accounts for the majority of density heterogeneity in the tissue. Also, the precision with which the operator is able to define bone may not be of large importance for dose calculation proposes but it has extreme importance when generating positioning reference images. So, it's essential to develop an automated process for MR conversion into sCT data.

Another approach is the Anatomy Method which enables automatic generation of sCT data using MR-label image atlas mentioned previously in section 2.4.1. This method has been developed for attenuation correction applications within positron emission tomography (PET)/MRI [44], [46], [73], [74] as well as for radiotherapy [37], [42], [43], [45], [47]. These methods normally do not rely on tissue segmentation; rather they warp full complexity atlas data onto patient specific shape yielding results similar to those provided by Bulk Density Assignment approach.

Dowling et al [43] found that differences in point dose between CT and atlas based images are less than 2% for prostate patients. Uh et al. [37] showed that atlas based images constructed using both mean arithmetic and pattern recognition processes differed from the original CT values in mean dose to the PTV by less than 1.3% of the prescription dose for brain tumours. When looking at OAR, the mean dose to right and left cochleae differed from the original CT values around 2% to 4% while when using a water uniform density scheme the percentage differences rise to around 8% to 10%.

Despite the Atlas approach gives accurate dosimetric results and despite being more automatic than the Bulk Density Assignment approach, an error of unknown magnitude is resulting from the registration processes and if the deformed sCT images are used to create the positioning reference, a systematic geometrical error may arise into the treatment. Also, both Bulk Density Assignment and Atlas approaches are usually sensitive to atypical geometries and patient variability (such as the presence of structural abnormalities and presence of metal implants).

Recently a vast interest has arisen for the use of methods that perform a direct conversion of MRI intensity values into HU - previously mentioned in section 2.4.2.2. In Jonsson et al. [75] study, sCT data were generated using UTE sequences with 2 flip angles and 2 echo times combined with a Gaussian regression mixture regression model to link the voxel values in CT images to voxel values in MRIs. Dose calculations performed on sCT images were compared to the real dose distributions for intracranial lesions and the isocenter point differences were within $\pm 0.5\%$. In Rank et al. [56], [76] a voxelwise tissue based classification was performed to derive sCT images using as input 8 different MR contrast images, including UTE sequences. The voxel classification into each tissue class was done using discriminant analysis. Difference in dose distributions between sCT and CT plans in the PTV mean coverage was less than 0.2% for tumours in the head region.

Benefits of these Voxel based Methods include that they can be fully automatic and the geometric integrity of UTE images is preserved. UTE images are subject to the same system related distortions, inhomogeneities in the magnetic field and nonlinearity in the gradients, as traditional MR images. However, these images are less sensitive to common object related distortions, such as chemical shift and susceptibility effects, because of its very short TE and fast radial sampling of the k-space. The main disadvantages of using this method are related to the necessity of using different MR sequences to be able to perform tissue classification. Hence, an increment of the scanning duration that might introduce problems related to patient and organ motion and an extreme dependency on scanner hardware and imaging pulse specifications is verified.

Chapter 3

Methods

3.1 Data Specification

This study includes data from 6 anonymized H&N cancer patients (Patients 1 to 6), more specifically nasopharynx patients, treated with VMAT and 16 anonymized prostate cancer patients (Patients 1 to 16) treated with IMRT both provided by RMH London. Prostate patient 16 has a metal prosthetic hip situated on the left femur head which will be taken into consideration when building and evaluating the sCTs for that patient.

The data sets for each patient include:

1. Planning CT + Structure Set;
2. T2 and T1 weighted MRIs obtained with a turbo spin echo sequence;
3. Clinically approved treatment plan.

CT data was obtained using both a Philips Big Bore CT scanner and a GE LigthSpeed Ultra CT scanner operated at 120 kV. MR data was obtained using a Siemens 1.5T MRI scanner. Both MR and CT images of each patient were taken on the same day and in the same position: Head First-Supine (HFS). The voxel size for T1- and T2- MRI scans is $0.104 \times 0.104 \times 0.2$ cm^3 for all H&N patients, $0.164 \times 0.164 \times 0.5$ cm^3 for T1-MRI scans and $0.146 \times 0.145 \times 0.5$ cm^3 for T2-MRI scans for all prostate patients. For H&N patients, the voxel size for CT scans is $0.096 \times 0.096 \times 0.25$ cm^3 for patient 1 and 6 and $0.117 \times 0.117 \times 0.2$ cm^3 for the remaining ones. For prostate patients, the voxel size for CT scans is $0.117 \times 0.117 \times 0.15$ cm^3 for patient 13, $0.096 \times 0.096 \times 0.12$ cm^3 for patients 6, 10, 12 and 15 and $0.098 \times 0.098 \times 0.15$ cm^3 for the remaining ones. Each patient has a structure set, which contains information about all annotated structures, including the target volumes, OARs and a full CT-based body outline. Optimized plans and clinical delineated volumes on the planning CT were obtained using Pinnacle^3 (Philips Medical System). Further evaluation was done using RayStation (RaySearch Laboratories) where plans, structure and images sets were imported to. All medical imaging data sets are in DICOM (Digital Imaging and Communication in Medicine) format which is the standard format between different types of medical devices.

3.2 sCT Construction

3.2.1 sCTa

The attainment of the sCT_a was based on a method previously mentioned in section 2.4.1 - Atlas Method based on weighted average and similarity measures [46] - with some modifications. This method was applied for both H&N and prostate patients. For the prostate patients, an atlas construction was required. Details regarding to the atlas construction will be explained first. This part of the project was done in collaboration with Centre of Medical Image Computing (CMIC) and Translational Imaging Group of University College London (UCL).

3.2.1.1 Prostate Atlas Construction

The generation of sCT_a for H&N and prostate patients implies the use of atlases made of CT and MR image pairs from different subjects. The H&N atlas was already built on using T2-weighted MR images and CT scans for 17 patients provided by University College London Hospital (UCLH). The construction details and results regarding to the utilization of this atlas are stated in [77]. In H&N patients inaccuracies when performing inter-subjects registrations may arise especially due to large scale postural changes such as flexion or extension of the neck and position of the jawbone that might cause large epiglottis/tongue mismatch between MR and CT images. Despite that, sCT_a generation using this approach proved to be accurate enough to be potentially used in RTP [77]. Considering these results, it was decided to test this algorithm for prostate patients for the first time where inaccuracies might arise especially due to organ motion regarding to different bladder fillings. Prostate data provided by RMH was used where each patient had a set of scans including T1- and T2-weighted MRIs and CT scans.

Registrations were performed using NiftyReg (http://cmic.cs.ucl.ac.uk/home/software/) which was developed in CMIC at the Department of Medical Physics and Bioengineering of UCL. For image processing and evaluation an additional software was used - NifTK - also developed by CMIC. It contains several tools such as NiftyView for image analysis and visualization and niftkN4BiasFieldCorrection for MRI bias field correction. NiftyReg and NifTK use a common image format called NIfTI (neuroimaging informatics technology initiative) and therefore mricron software (https://www.nitrc.org/projects/mricron) was used to convert data sets from DICOM to NIfTI format and an in-house MATLAB script was used to convert the data sets from NIfTI to DICOM format (see APPENDIX A.1).

After converting images to NIfTI format, a mask to segment the body outline designed using tools in NiftyView was applied to each patient. These masks were used to remove the existence of the fiducial markers placed for positioning as their presence was interfering with the quality of the registration process.

The prostate atlas construction started with image processing and all MRIs were bias field corrected (Figure 3.1). A bias field is a low frequency smooth and undesirable signal that causes the corruption of MR images due to inhomogeneities in the magnetic field of the scanner [78]. Due to bias field, high frequency contents of the MR image, such as edges and contours, get reduced resulting in changes of the intensity values of image pixels. As a result, the same tissue presents different grey level distribution across the image introducing a blurred effect. Bias field correction was implemented using niftkN4BiasFieldCorrection executable which is based on N4 bias field correction contributed to ITK by Nicholas J. Tustison and James C. Gee [79].

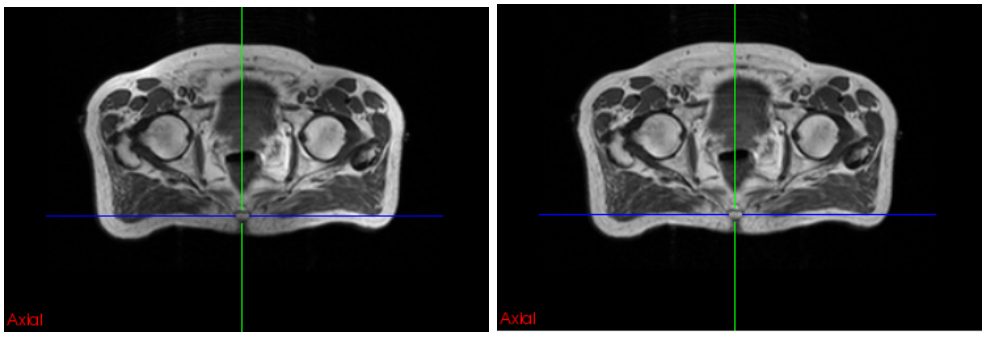

(a) (b)

Figure 3.1: Axial images for one representative prostate patient showing the original MRI (a) and the bias field corrected MRI (b). Images are T1- weighted images. Differences in pixels intensities near the cursor are seen.

The corrected image is then obtained using the following model:

$$v(x) = u(x)f(x) + n(x) \tag{3.1}$$

Where v(x) is the input image, u(x) is the corrected image, f(x) is the bias field (estimated by a Gaussian model) and n(x) is the noise. As input values two parameters where defined: FWHM and noise. FWHM is the full width at half maximum of the Gaussian used to model the bias field and noise is the noise estimation performed by deconvolution using a Wiener filter. High values of FWHM and low values of noise gave better results.

After performing bias field correction, the corrected MR images were aligned to the respective CT images using an affine transformation. The registration was performed using a symmetric global block matching algorithm based on Ourselin et al. [80] in a two-step approach. The first step is based on establishing a point correspondence between the floating - MRI - and reference image - CT [81]. This is achieved by dividing the reference and floating image into blocks of the same size. Then, each block in the reference/floating image will be compared to the blocks in a pre-defined neighborhood in the transformed floating/reference image. This algorithm ensures that the registration is symmetric and no bias is comming from the registration direction. The process will be done iteratively until the optimal rigid transformation is found by calculating the normalized cross correlation (NCC) to evaluate the block matching:

$$NCC = \frac{1}{N} \times \sum_{\vec{x} \in b_r} \frac{[b_r(\vec{x}) - \mu_{b_r}][b_f(\vec{x}) - \mu_{b_f}]}{\sigma_{b_r} \times \sigma_{b_f}} \tag{3.2}$$

Where b_r and b_f denote blocks in the reference and floating image, respectively, μ and σ correspond to the mean and standard deviation value within a block and N to the number of voxels in a block.
The second step is based on computing the transformation parameters according to the optimal point correspondence using a Least Trimmed Squares regression. In the end, as output the floating image will be mapped into the space of the reference image.

After performing an affine body registration for all CT-MR image pairs, all CT and MR images were deformably registered to each other using a fast free-form deformation algorithm in NiftyReg [82]. This method uses Cubic B-Spline to deform the floating image in order to optimize an objective function based on Normalised Mutual Information (NMI) and on penalty terms such as the bending energy (BE) and the squared Jacobian determinant log (JL).
The algorithm computes a rectangular grid superimposed on the image size that will get deformed under the influence of a finite number of uniformly spaced control points. Individual voxel movement between the two images is parameterized in terms of these control points (Figure 3.2) and the displacement vectors that maps the voxels in the floating image to those in the reference image are obtained via interpolation using a piecewise continuous B-spline basis functions.

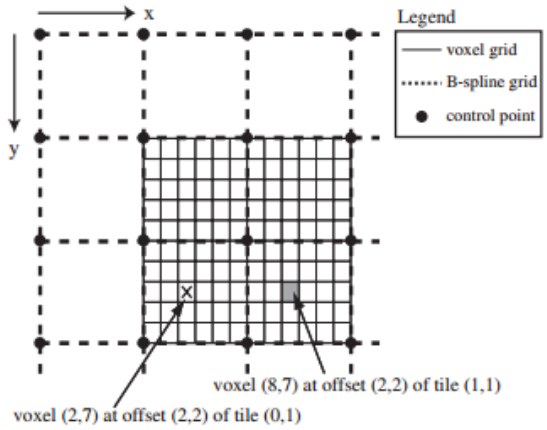

Figure 3.2: A portion of 2D image showing a B-Spline control-point grid superimposed upon an aligned voxel grid. The voxel grid is then divided into 6×5 tiles. The vector field at any given voxel within each tile is influenced by the 16 control points in the tile's immediate vinicity and the value of the B-Spline basis function evaluated at each voxel. The B-Spline function is only dependent on the voxel's local coordinates (i.e offset) within the tile [83].

The B-Spline interpolation yielding the x-component of the displacement vector field, $\vec{v}$, for a voxel located at (x,y,z) is given by [83]:

$$v_x(x,y,z) = \sum_{l=0}^{3}\sum_{m=0}^{3}\sum_{n=0}^{3} \beta_l(u)\beta_m(v)\beta_n(w)\ p_{x,l,m,n} \tag{3.3}$$

Where p_x is the spline coefficient defining the x component of the displacement vector for one of the control points that influence the voxel.

The uniform cubic B-Spline basis function β_l along the x-direction is [83]:

$$\beta_l(u) = \begin{cases} \dfrac{(1-u)^3}{6} : l = 0 \\ \dfrac{(3u^3 - 6u^2 + 4)}{6} : l = 1 \\ \dfrac{(-3u^3 + 3u^2 + 3u + 1)}{6} : l = 2 \\ \dfrac{u^3}{6} : l = 3. \end{cases} \tag{3.4}$$

The same equation is used to find β_m and β_n along y and z directions respectively. u, m, and n are determined, normalized between [0,1], by $\frac{x}{N_x} - \lfloor \frac{x}{N_x} \rfloor$, $\frac{y}{N_y} - \lfloor \frac{y}{N_y} \rfloor$, $\frac{z}{N_z} - \lfloor \frac{z}{N_z} \rfloor$, respectively. $N_x \times N_y \times N_z$ are the dimensions of the B-spline control point grid in terms of voxels.
The displacement vector field, $\vec{v}$, is the vector field which includes all displacement vectors of all the voxels. Once the displacement vector field is generated, it is used to deform each voxel in the floating image.
In the end, the deformation T which denotes the displacement vector field that optimizes the most the objective function that quantifies the similarity between the deformed floating image, F(T), and the reference image, R, is found.

NMI is a voxel intensity based similarity measure that is used to find the best match between F(T) and R [82]:

$$NMI(A, B) = \frac{H(A) + H(B)}{H(A, B)} \tag{3.5}$$

Where H(R), H(F(T)) and H(R, F(T)) are respectively the two marginal entropies and the joint entropy. The entropy H of a given image point is a measure of how well the intensity of that point can be predicted [16]. Similarity, the joint entropy measures the amount of information that is given by the two images combined. The more similar images are, the lower the joint entropy compared with the sum of the individual entropies is. Thus, larger NMI values reflect a greater level of shared information between them. NMI is maximized at the optimal alignment between images.

Optimizing the similarity is not the unique goal of the registration process. Without any restrictions, unrealistic transformations, such as folding, could be made while trying to maximize the resemblance between images. To avoid that usually two penalty terms are applied: The BE, which restrains the transformation smoothing, and the JL, which constrains the transformation T changes in each 3 directions penalizing local tissue expansion and compression. If JL=0 the deformation will be incompressible allowing local volume preservation. For bigger values of JL more changes in volume will be allowed. For CT-MRI registrations lower values of BE and JL gave better results (Figure 3.3).

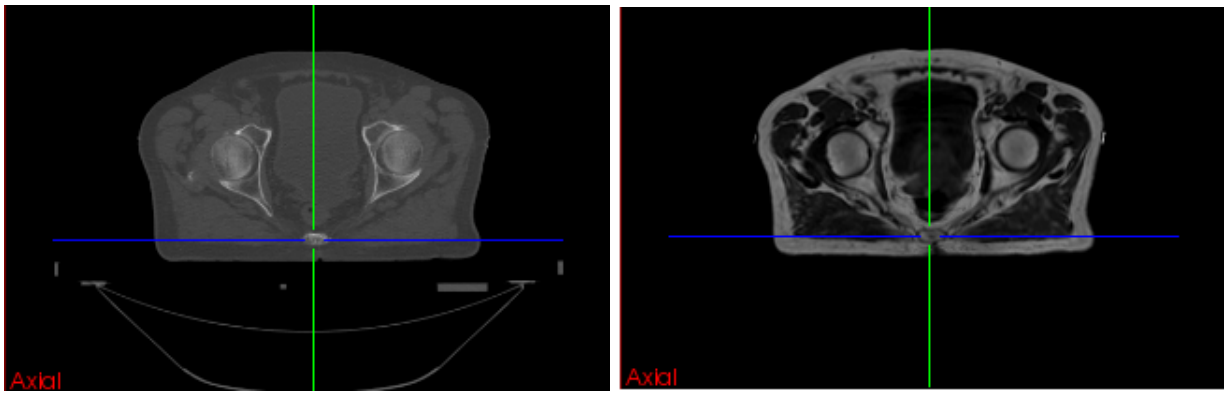

(a) (b)

Figure 3.3: Schematization of a deformable registration performed for one representative prostate patient (axial view). In (a) is represented the planning CT while in (b) is represented the T1-MRI deformably registered to the CT.

3.2.1.2 Methodology

The method used for sCT_a construction is based on three main steps [77]:

1. **Construction of the atlas database:** To form the database, CT and MR images of each patient were first affinely and then non-rigidly aligned, as explained before, to account for differences in patient positioning during acquisition. For the H&N patients, 17 pairs of T2-weighted MRI and CT scans were used to build the atlas and for the prostate patients, the atlas was built using a combination of both T1 and T2-weighted MRI information and CT pairs from 14 patients. The 6 H&N evaluation patients were not part of the atlas database while the 15 prostate evaluation patients (excluding patient 16) were used to build the atlas. For prostate patients, the evaluation of the sCT_a was done using a Leave-one-out Cross-validation (LOOCV) approach. After finishing registering the MR-CT image pairs, they were also aligned into a common coordinate frame via an affine groupwise registration [81]. The transformations were applied to each CT-MR image pair iteratively by updating their image coordinate system. At the end, a database of MR and CT images in the same common space was built.

2. **Alignment of the target MRI to the database:** The first step to synthetize the sCT_a was to register the target MRI to all MR images in the atlas database using a symmetric global affine registration followed by a deformable cubic B-Spline registration, using NMI as similarity measure as before. When the FOV of the target MRI is limited to just cover the tumour, as it happens for the H&N patients (see section 3.2.3), the use of a simple affine alignment can be inaccurate. To overcome this limitation, a robust affine was applied relying on the fact that all atlases pairs are in the same space framework. The robust affine could be divided in three main steps: First, each MRI in the atlas was affinely aligned to the target MRI. Second, the average transformation obtained from all the affine transformations applied was calculated. Finally, the average affine was then used to start a second affine registration step to refine the registration results and to guarantee that each atlas is initially aligned with the MRI target before applying the cubic B-Spline parametrised non-rigid algorithm. To build the sCT_a, the non-rigid transformations were also applied to all CTs in the atlas database.

3. **Synthesis of the sCT_a:** The sCT_a was obtained by fusing the mapped atlases to the target MRI using a voxelwise weighting scheme where the weights were defined according to the use of morphological similarity measures between the atlas and the target image. The similarity measures were used under the supposition that if two MR images are similar at a certain spatial location the two CT images will also be similar at the same location.

One similarity measure was used to evaluate the quality of the alignment between the two images, with a larger focus on high contrast regions, based on the LNCC proposed by Cachier et al. [84]. The LNCC at voxel $\vec{v}$ is given by [77]:

$$LNCC_n(\vec{v}) = \frac{\langle I^{MRI}, J_n^{MRI} \rangle(\vec{v})}{\sigma(I^{MRI}(\vec{v}))\sigma(J_n^{MRI}(\vec{v}))} \tag{3.6}$$

Where the target MRI is given by I^{MRI} and the MR atlas image from subject n is denoted by J_n^{MRI} at voxel $\vec{v}$. The NMI was not used as similarity measure to avoid redundancy of the results as it was already used in the atlas construction stage.

Such as in [46] (see section 2.4.1) a ranking scheme was applied giving a larger weight to MR images better registered to the target MRI. The ranks, $R_n(x)$, were converted to weights using an exponential decay function as in Equation (2.6), where β assumes a value equal to 0.5. The final sCT_a is obtained using a spatially varying weighted averaging to determine each voxel value using Equation (2.7).

3.2.1.3 Iterative Bone Refinement Process

This algorithm relies on the capability of accurately mapping images from different subjects. Opposing to CT imaging, MR imaging does not provide good contrast for bone localization and in order to improve the registration results in low contrast areas, an additional sCT_a was created in an iterative bone refinement process – sCT_a_bref. For this multiple modalities were used: an initial sCT_a, generated by the method described previously, and the target MRI. The sCT_a generated was then combined with the target MRI to form a MRI-sCT_a pair. Then the MRI-sCT_a pair was registered to all MRI-CT atlas pairs first using the robust affine and then the non-rigid registration. MRI-sCT_a pair was registered to all MRI in the atlas using as similarity measure NMI (Equation (3.5)) and to all CT images in the atlas using NSSD.

The NSSD characterizes the differences in intensity between the two images, making it more susceptible to contrast problems, and is given by [46]:

$$NSSD_n(\vec{v}) = \left[G_{\sigma_G} \star \left(\frac{I^{sCT} - \overline{I^{sCT}}}{\sigma(I^{sCT})} - \frac{J_n^{CT} - \overline{J_n^{CT}}}{\sigma(J_n^{CT})} \right) \right]^2_{\vec{v}} \tag{3.7}$$

Where I^{sCT} is calculated using Equation (2.7) and corresponds to the intensity values in the sCT_a generated while J_n^{CT} corresponds to the intensity values in each CT atlas image from subject n.

sCT_a_bref is then obtained by fusing the mapped MRI-CT pairs according to their similarity to the target MRI-sCT_a pair which is weighted using a multivariate LNCC (MV-LNCC) defined as [77]:

$$MV - LNCC_n = LNCC(I^{MRI}, J_n^{MRI}) + LNCC(I^{sCT}, J_n^{CT}) \tag{3.8}$$

The weights and final sCT_a_bref are obtained using the same equations (Equations (2.6) and (2.7)) as for sCT_a.

This bone refinement was implemented for both H&N and prostate patients. For the H&N patients, sCT_a and sCT_a_bref were built with the resolution of the T2-weigthed MRIs while all sCT_a and sCT_a_bref for the prostate patients were built with the resolution of the planning CTs. For patient 16, with the prosthetic hip, the same method with no modifications was applied to build both sCT_a and sCT_a_bref. This was done to verify if the atlas scheme is capable of automatically reproducing the presence of the metal implant.

After sCT_a and sCT_a_bref scans were constructed they were converted into DICOM format and imported into RayStation where they were further analysed. In Figures 3.4 and 3.5, for one representative H&N and prostate patient it's represented the planning CT, sCT_a and sCT_a_bref using the same slice. In Figure 3.6, one can see the planning CT, sCT_a and sCT_a_bref for prostate patient 16. Doses were re-calculated on both sCT_a and sCT_a_bref using the original clinical plan.

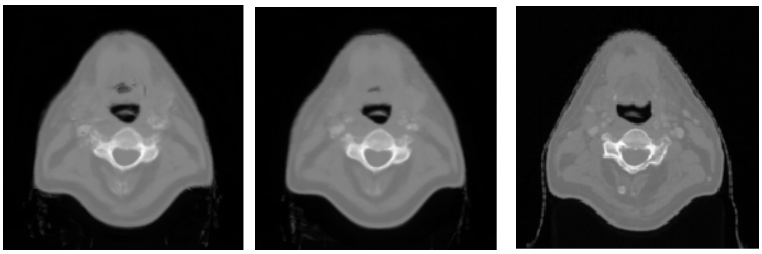

(a) (b) (c)

Figure 3.4: Transverse plane scans for one representative H&N patient showing the sCT_a (a) the sCT_a_bref (b) and the planning CT (c) using the same slice.

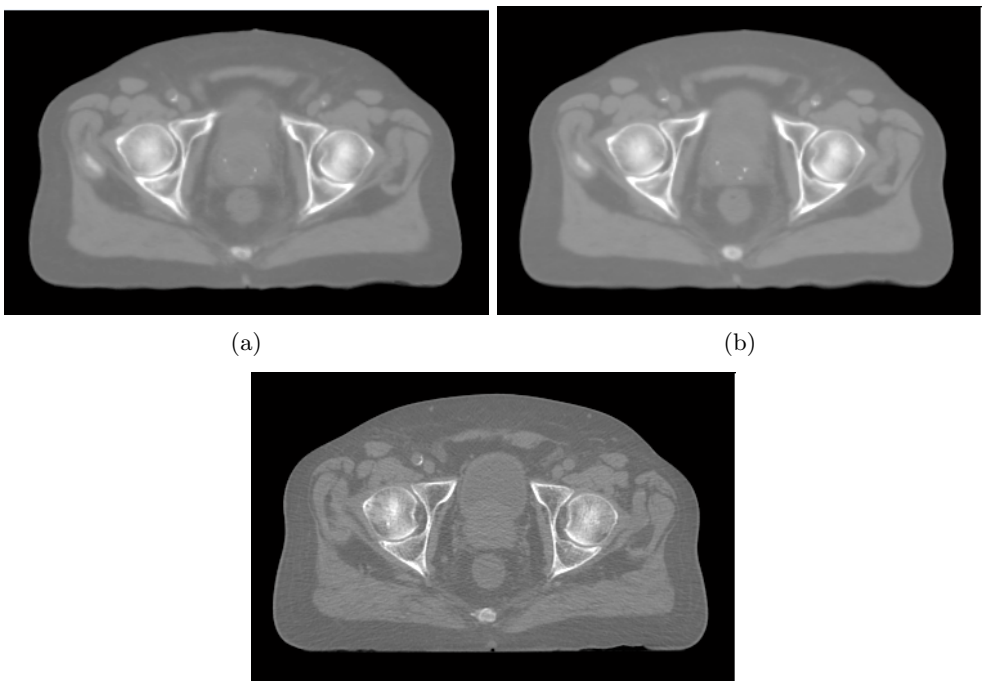

(a) (b)

(c)

Figure 3.5: Transverse plane scans for one representative prostate patient showing the sCT_a (a) the sCT_a_bref (b) and the planning CT (c) using the same slice.

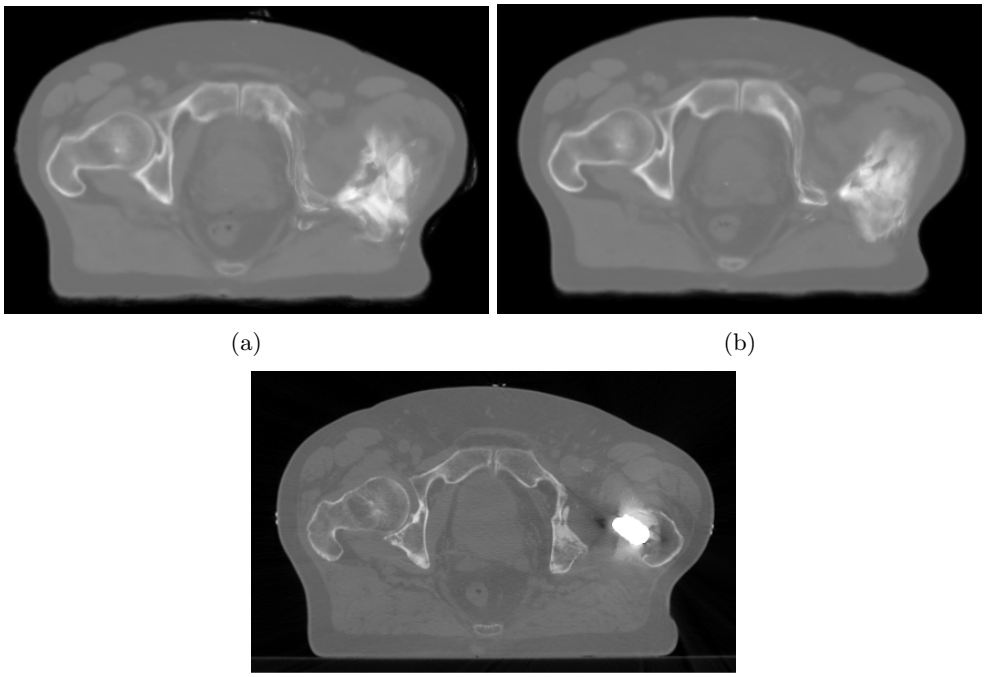

(a) (b)

(c)

Figure 3.6: Transverse plane scans for the prostate patient with a prosthetic hip (patient 16) showing the sCT_a (a) the sCT_a_bref (b) and the planning CT (c) using the same slice.

3.2.2 sCTbda

sCT_{bda} were generated using the Bulk Density Assignment method. Two different types of sCT_{bda} were created: one using CT information to test the influence of rough density estimates - sCT_{bda}_CTinfo - and the other using only MR information (both T1- and T2- weighted) to add the uncertainties of MRI contouring - T1- and T2-MRinfo sCT_{bda}. sCT_{bda} construction and evaluation was performed in RayStation.

The creation of both sCT_{bda} involved the following main steps:

1. CT-MRI rigid registration to spatially align both image sets using the planning CT as reference image and the MRI as floating image. The first part of the registration was performed manually to find a gross match between both volumes. This was done 3D, where the user was able to rigidly translate and rotate the floating image. To find a fine match between both images an automatic 3D Grey Level based registration algorithm was then applied. In RayStation, the algorithm uses NMI as similarity measure when performing registration between images of different modalities.

2. Delineation of tissue classes and assignment of specific electron density values to each class while the remaining anatomy was defined to be of water equivalent density. For the prostate patients bone (1.22 g/cm^3) and for the H&N patients air (0.001g/cm^3) and bone (1.53 g/cm^3) tissue classes were defined (Figure 2.8).

3. Dose distribution re-calculation on the sCT_{bda} keeping the CT planning parameters, unchanged.

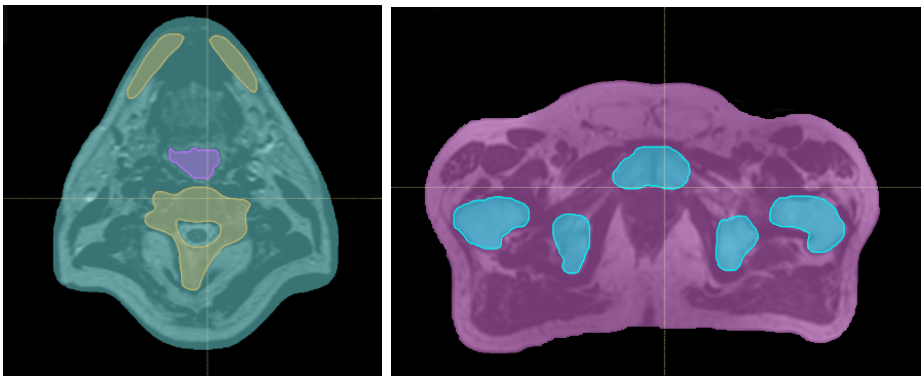

(a) (b)

Figure 3.7: Representation of tissue classes definition for sCT_{bda}-MRinfo for one representative H&N (a) and prostate (b) patients. For the H&N patient in (a), bony anatomy is defined in orange, air class in pink and the remaining tissue defined with water equivalent density in blue. For the prostate patient in (b) bone is defined in blue while the remaining soft tissue is represented in a pink color.

The delineation of the external geometry and tissue classes was done differently depending on the sCT_{bda} type.
For sCT_{bda}-CTinfo both external and tissue classes were delineated on the CT and rigidly copied to the T1-weighted MRI. The external was delineated using an automatic tool in RayStation that computes a threshold value to outline the patient body. Manual adjustments were also applied to exclude holes and small contours on the outline. For the H&N patients, air and bone were defined using a threshold-based condition. Air was defined to have HU values between -1024 and -900. Also ROI algebra was applied to define air contour within the external contour. For bone, a medium threshold was applied and HU values bigger than 200 were defined to be absolutely bone and smaller than 100 definitely not bone. For the prostate patients, a low threshold was applied to define bone contour as bone electron density is smaller for the femur than for the skull. Then, HU values bigger than 150 were defined to be definitely bone and HU values smaller than 50 were defined to be definitely not bone.
For T1 and T2-MRinfo sCT_{bda} both external and tissue classes were delineated directly on both MR images without relying on CT information. Bone delineation was made using a combination of threshold-based and manual delineation for both prostate and H&N patients. Air delineation in the H&N patients was done using a threshold-based segmentation. As air is one of the lowest intensity values in MRI, an MR intensity interval of 0 to 9 was applied to define air cavities. Possible deviations and the existence of small contours were corrected manually. External delineation was also automatically performed using a threshold based technique. Final sCT_{bda} scans were constructed with the resolution of the original MRI used.

For patient 16 to build both CTinfo and MRinfo sCT_{bda}, in addition to tissue segmentation, the implant was also delineated using a combination of manual and threshold based delineation. As for the remaining anatomy, for sCT_{bda}-CTinfo the delineation was performed first using the CT scan and then copying the contour defined to the T1-MRI scan. As the metal implant had the highest tissue electron density, its delineation was straightforward. For sCT_{bda}-MRinfo the delineation was performed directly using T1- and T2-MRIs. Similarly to bone, the prosthetic hip was represented on the MRIs with a low intensity signal. Thus, the delineation process is performed as a best guess. As the implant was a titanium alloy prosthesis, a density of 3.71 g/cm^3 was given to the delineated contour [85].

3.2.3 Geometry Challenges

When constructing the sCT two major challenges had to be overcome: The reduced MRI FOV compared to CT FOV and the MRI lack of coverage.
While for the CT a large FOV was available, which involved scanning the H&N patients from the top of the head until the top of the lungs and the prostate patients from the abdomen until the lower limbs, for the MRI only the region of interest including the PTV was imaged. To make a consistent evaluation of the dose distributions differences between plans, all the anatomy regions outside the MRI FOV were assigned to be of water equivalent density (Figure 3.8). To simulate the whole body of the patient, the external CT contour was copied to the sCT_a and sCT_{bda} and altered in the MRI FOV to be able to maintain the original external forms in the sCT. This way, the only differences in plans will be related to different structure segmentation within the MRI FOV.

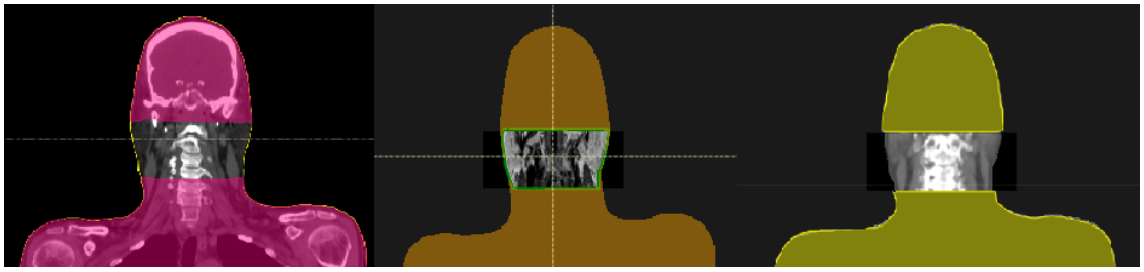

Figure 3.8: Representation of the geometry applied to CT and sCT scans to correct the reduced MRI FOV for one representative H&N patient. Regions outside the MRI FOV were assigned to be of water equivalent density and the same are represented in pink for CT scans (left), orange for MRI (middle) and yellow for sCT_a (right). The same geometry was implemented for the prostate patients.

Only the H&N patients suffer from the MRI lack of coverage and all sCT scans were affected. For the MRI, a full coverage of the patient outline was not available translating into missing tissue imaged in the back of the head or on the chin (Figure 3.9). To be able to maintain the use of the original external contours for T1- and T2-MRinfo sCT_{bda} and sCT_a, the following tissue gaps were assigned to be of air equivalent density. The maintenance of the sCTs original externals introduces a systematic error. To make sure that this does not influence the results, especially for the gamma analysis and DD, comparisons between scans were only made using slices in which this problem was not apparent.

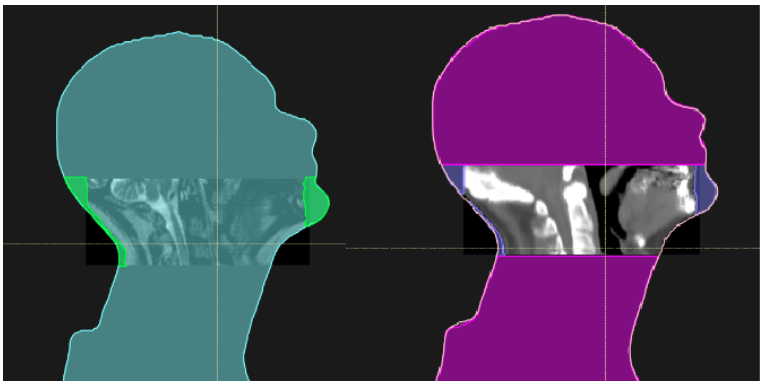

Figure 3.9: Representation of the geometry applied to sCT scans to correct the MRI lack of coverage for one representative H&N patient. Tissue gaps represented in green for MRI (left) and purple for sCT_a (right) were assigned to be of air equivalent density.

3.3 sCT Evaluation

For both H&N and prostate patients, the performance of the sCT was evaluated using a dosimetric and a geometric evaluation. Details related to that are described in section 3.3.1 and 3.3.2, respectively. Prostate patient 16 was evaluated separately from the remaining patients and details regarding to that are stated in section 3.3.3.

3.3.1 Dosimetric Evaluation

The dosimetric evaluation was performed using the original clinical contours delineated on the planning CT and rigidly copied to all the sCT generated. The planning CT contours were used for all methods to standardize the comparisons between the dosimetric performances of the sCT against the clinical one on the planning CT.

For the Bulk Density Assignment method, both CTinfo, T1- and T2-MRinfo sCT_{bda} were evaluated. For the Atlas scheme, both sCT_a and sCT_a_bref were evaluated. The dosimetric evaluation included the use of absolute DD maps, gamma analysis and DVH analysis. For that the calculated dose distributions were exported from the TPS in .mha and .mhd format (Insight Meta-image) and converted to a DICOM format using Iphyton Notebook. The dose cubs in DICOM format were then imported into MATLAB using DICOM-RT-based toolbox [86] and evaluated afterwards using in-house MATLAB functions and scripts.

DD maps were calculated for the whole body outline and using dose distributions in the same system of coordinates. The final map was built using an absolute dose difference between all points in the CT dose distribution and in the sCT dose distributions.

For gamma evaluation a local 2D gamma algorithm based on [28] was used (APPENDIX A.2). Both H&N and prostate CT and sCT dose cubs had the same dose grid equal to $0.25 \times 0.25 \times 0.25$ cm^3/voxel. For each slice used in the gamma evaluation, pixel resolution was resized using a cubic interpolation to obtain a pixel with 0.5×0.5 mm^2 dimension. The investigation was then performed using 2 combinations of DTA and DD: 3mm_3% and 2mm_2%. Gamma analysis was performed using the whole body outline contour. Finally, the information from the gamma map was summarised using a gamma histogram and a cumulative gamma volume histogram to determine the percentage of passing points.

For DVH analysis, the DVH for PTV and OAR was plotted for all sCT methods against the real clinical curve. Also a DVH point difference investigation for the most common DVH points was performed using the following:

$$Diff(\%) = \frac{D_{CT_i} - D_{sCT_i}}{D_{CT_i}} \times 100 \tag{3.9}$$

Where D_{CT_i} and D_{sCT_i} are the dose value for a specific DVH point obtained using the CT and sCT dose distributions, respectively. According to each patient and structure evaluated, the DVH points used are referenced in Table 3.1.

Table 3.1: Dosimetric evaluation: Analyzed DVH points summary for the H&N and the prostate patients.

Patient	ROI	Volume Definition	DVH Points
H&N	PTV	Target Volume	D98%; Dmean; D2%
	SpinalCord	Serial OAR	D2%
	LParotid	Parallel OAR	Dmean
	RParotid	Parallel OAR	Dmean
Prostate	PTV	Target Volume	D98%; Dmean; D2%
	Prostate	Target Volume	Dmean
	Rectum	Serial OAR	D2%
	Bladder	Serial OAR	D2%
	LFem	Serial OAR	D2%
	RFem	Serial OAR	D2%

For the H&N patients, the LParotid, RParotid and SpinalCord denotes the right and left parotids and spinal cord, respectively. For the prostate patients LFem and RFem denotes the left and right femur heads, respectively.

A statistical analysis was also performed to evaluate the dosimetric performance of each sCT. The statistical analysis was performed individually on each diagnostic group for the calculated percentage difference of the reported DVH points using MATLAB. As a final goal, the significance of performing dose calculations on each sCT was investigated by comparing the percentage dose deviations between dose distributions based on each sCT against the original one based on CT.
For both H&N and prostate patients, the normality distribution of the data was first investigated using the Shapiro-Wilks normality test. The null hypothesis of this test is that the data for each diagnostic group is normal with unspecified mean and variance. A significant level of 0.05 was used. As not all the diagnostic groups passed the Shapiro-Wilks test, the normality of the data was not ensured. Thus, a non-parametric test was used to test the significance of the data. The Kruskal-Wallis test was selected as is the non-parametric equivalent test of the One-Way Analysis of Variance (ANOVA) test. The Kruskal-Wallis was then applied to assess if the dose differences between sCT and CT dose distributions have equal medians. The null and alternative hypothesis can be written as:

$$H0 : M_{sCT_{bda\_CTinfo}} = M_{sCT_{bda\_T1-MRinfo}} = M_{sCT_{bda\_T2-MRinfo}} = M_{sCT_a} = M_{sCT_{a\_bref}}$$

$$H1 : M_{sCT_{bda\_CTinfo}} \neq M_{sCT_{bda\_T1-MRinfo}} \neq M_{sCT_{bda\_T2-MRinfo}} \neq M_{sCT_a} \neq M_{sCT_{a\_bref}}$$

A significance level equal to 0.01 was assumed. When the p-value is less than 0.01, the data is taken to be significantly different.

Finally, the results for the PTV Dmean DVH point for both H&N and prostate patients were summarized using a box and whisker plot. The box and whisker plot illustrates the quartiles in the data where each quartile describes 25% of the data. The box illustrates the 2^{nd} and 3^{rd} quartile which are separated by the median and the whiskers indicate the 1^{st} and 4^{th} quartile and extend to the minimum and to the maximum value, respectively. However, the whiskers only extend to the smallest/largest observation when it's not too far from the $2^{\text{nd}}/3^{\text{rd}}$ quartile. Data points that do not fulfill these criteria are displayed as outliers. The box plots were used to evaluate the degree of dispersion of the results from the sCT against the CT plan.

3.3.2 Geometric Evaluation

The geometric evaluation was performed using the CT contours (sCT_{bda}_CTinfo) and the delineations/segmentations performed on the T1- and T2-weighted MRIs (sCT_{bda}_MRinfo) and on the sCT_a scans. To make standardize comparisons all clinical contours were redrawn using the same treatment planning system as for MRI and sCT_a based delineations - RayStation. The following contours were evaluated: external, bone and OARs. For the H&N patients, the contours from the left and right parotids and the spinal cord were delineated and for the prostate patients, the left and right femur heads, the rectum, the bladder and the prostate contours were outlined.

The delineation of the OAR was performed by a qualified clinician for each site. The external contour was delineated automatically using threshold in all scans. In MRI scans, bone contours were delineated manually as explained before (see section 3.2.2). In CT, sCT_a and sCT_a_bref scans, bone delineation was performed automatically using a threshold based delineation. Evaluation of contours was made in terms of shape, position and volume individually and an overall evaluation using Dice Similarity Coefficient (DSC) was also performed.

To evaluate the shape and position of contours a simple overlay of the clinical contours with the new segmented ones using Iphyton Notebook was made.

To evaluate changes in volume a Volume Index (VI) was calculated:

$$VI = \frac{V(A) - V(B)}{V(A)} + 1 \tag{3.10}$$

Where V(A) is the volume of the reference contours and V(B) the volume of the evaluated contours. The addition of 1 ensures that identical volumes have an index equal to 1. This formula is applied for external and bone contours using the clinical contours as reference volumes as it's well known that bone and body outline delineation is accurately performed when using a CT scan. The OAR delineation is based on soft tissue contrast which is better performed when using an MRI instead of CT, being this one of the main reasons to substitute CT for MRI in RTP. For OARs, treating the original CT based delineations as gold standard is probably not correct and so to make fair comparisons between these contours delineations the volume for these organs were plotted in absolute value to detect any tendency when using contours based on CT, MRI and sCT_a information.

DSC is an index often used to evaluate changes in position, size, shape and orientation of two overlapping volumes. A value of 0 indicates no overlap between volumes and a value of 1 indicates perfect agreement. DSC is given by [87]:

$$DSC(A, B) = \frac{2|V(A) \cap V(B)|}{V(A) + V(B)} \tag{3.11}$$

Both volumes and intersection and union between volumes were obtained using ROI algebra tools in RayStation. As recommended by Zijdenbos et al [88] in literature of image validation, a good overlap occurs when DSC >0.7.

A statistical analysis was also performed considering all diagnostic groups to evaluate the geometric results - VI and DSC. For both H&N and prostate patients, the normality distribution of the data was first investigated using the Shapiro-Wilks normality test. A significant level of 0.05 was used. As not all the diagnostic groups passed the Shapiro-Wilks test, no assumptions about the probability distributions of the diagnostic groups were assessed. For the same reason as before, a Kruskal-Wallis test was performed.
The Kruskal-Wallis test was applied to both VI and DSC results to see if is significantly different performing delineation using sCT_{bda}_MRinfo (T1-MRI / T2-MRI) and sCT_a (and sCT_a_bref only for bone) when comparing to delineations performed using CT scans. The null and alternative hypothesis can be written as:

$$H0 : M_{T1-MRI\_CT} = M_{T2-MRI\_CT} = M_{sCT_a\_CT}$$

$$H1 : M_{T1-MRI\_CT} \neq M_{T2-MRI\_CT} \neq M_{sCT_a\_CT}$$

A significance value of 0.01 was assumed.

3.3.3 Prostate Patient 16 Evaluation

For prostate patient 16 only a dosimetric evaluation including the use of absolute DD maps and gamma analysis was performed. Gamma analysis was done using the same local 2D gamma algorithm and also after resizing the pixel size to $0.5 \times 0.5 \quad mm^2$ (see section 3.3.1). The gamma test was applied for the external contour and using a 2mm_2% combination of DTA and DD. Also, the percentage of passing points was determined for the applied criteria.

3.4 Evaluation of MR Field Induced Dose Effects on sCTs

In the future, MRI-only external radiotherapy treatments are foreseen to be performed at MR-LINAC machines which are devices incorporating both MRI scanner and a LINAC enabling patient imaging while the treatment is being delivered. The treatments will be delivered to the patient located within a strong magnetic field, affecting all aspects of measuring and calculating the absorbed dose (see section 2.5). The ability to estimate these dosimetric effects during treatment planning depends on the accuracy of the underlying patient geometry. Thus, it's necessary to investigate if both sCT_{bda} and sCT_a are accurate enough to reproduce these effects.

This part of the project was performed using a research version of Monaco® (Elekta) based on the Monaco® clinical version 5.00.00. Dose distributions in the presence of magnetic fields were calculated for 3 of the 6 H&N patients (Patient 1, 2 and 6) where the challenges regarding to MRI lack of coverage stated in section 3.2.3 were not as evident. These 3 patients were chosen trying to minimize the effects of the geometry inaccuracy in the final results.

The 3 patients scans and structures sets were exported from RayStation into Monaco® while all the planning was performed directly in the Monaco® TPS. The planning and optimization of the final plan was performed using the planning CT at 0T for each patient and the same plan was re-calculated on the following sCT's: sCT_{bda}_T2-MRinfo and sCT_a. As the methodology for the construction of both sCT_{bda}_MRinfo and sCT_a and sCT_a_bref was the same, sCT_{bda}_T2-MRinfo and sCT_a were chosen to represent each method. Also, the sets of optimized objectives for 0T plans were unaltered when recalculating the plan at higher field strengths (0.5T and 1.5T).

3.4.1 Geometry Definition

Regarding the reduced FOV of the MRI and to be able to perform equal comparisons between plans under the same conditions, the FOV of the CT was reduced and equalled to the FOV of the MRI. The planning was then performed using this restrained set of CT scans. Bone and air tissues defined previously in RayStation were used for bulk density override in sCT_{bda}-T2-MRinfo. The same electron density values were applied to each contour while the rest of the body was assumed to be of water equivalent density. Trying to minimize the geometrical inaccuracy introduced by the MRI lack of coverage, the tissue gaps previously defined to be of air equivalent density were now filled in with a water equivalent density trying to simulate soft tissue and the skin boundary on those areas. PTV and OAR defined on the planning CT were used for planning purposes in all methods. To avoid increasing plan complexity and consequently higher degrees of modulation during plan optimization, the PTV was modified and reduced by 1cm in superior and inferior direction.

Also, as the PTV and PTV nodes (PTV1 and PTV2 respectively) were defined adjacent to the skin surface (Figure 3.10) a bolus contour was created to provide a more effective treatment to the superficial target volume. Megavoltage photon beams exhibit a dose build up effect that translates at a maximum absorbed dose at a certain depth beyond the surface. This produces a 'skin sparing' effect which is highly dependent on beam parameters. A bolus is used as a build-up material placed on the skin to enhance dose near the surface. This contour was generated for both CT and sCT using ROI algebra by expanding the PTV and PTV nodes contours by 1cm margin and subtracting the patient outline. Finally, a water equivalent density was applied to the contour defined.

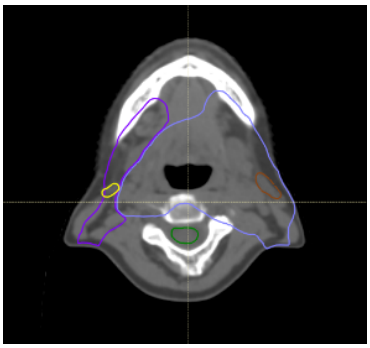

Figure 3.10: PTV and OAR geometry for one representative H&N patient using a CT scan: the PTV1 is represented in ligth purple, the PTV2 in purple, the RParotid in yellow, the LParotid in brown and finally, the SpinalCord contour in green.

3.4.2 Planning

For the 3 H&N patients, a VMAT photon plan with a prescription dose of 65 Gy into 30 fractions was planned and optimized as before. The dose was prescribed to the PTV1 isocenter. The VMAT implementation in Monaco® follows the workflow of static gantry IMRT plans in which the clinical goals are identified first and then an optimization algorithm is used to find the best configuration of beam intensities.

3.4.2.1 Beam Parameters

For a VMAT plan it's mandatory to specify beam parameters such as the maximum range of the gantry rotation and the frequency at which static fluence profiles sample the arc - Number of sectors (Figure 3.11). The beam settings denoted in Table 3.2 were equally specified for the 3 patients.

The increment determines in how many sectors the initial full arc will be divided for the optimization process to generate fluence profiles at static gantry positions. Using an increment that is too large, creates fewer sectors which can result in poor quality plans and using an increment that is too small increases computational time that may not significantly improve the plan quality. Accordingly to [89] using increments from 10 to 15 degrees allows having a homogeneous target dose without compromising the planning speed.

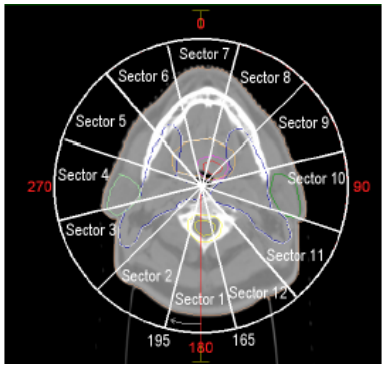

Figure 3.11: Full 360 degree arc with starting angle of 180 degrees and an increment of 30. The Monaco® system creates sectors in 30 degree increments starting 15 degrees in front of each angle and ending 15 degrees after each angle. For the implemented plan an increment equal to 15 was used instead [90].

Table 3.2: Defined VMAT plan beam parameters for all 3 H&N patients.

Beam Parameters	
Number of Beams	1
Number of Arcs	1
Energy (MeV)	6
Beamlet Width (cm)	0.3
Arc (deg)	360
Gantry Start Angle (deg)	180
Increment (deg)	15
Rotation Direction	Counterclockwise
Collimator and Couch Angle (deg)	0

3.4.2.2 Constraints

Monaco optimizes treatment plans using cost functions that model different types of tissue and volume specific radiation responses. The optimization is first performed using a constrained mode in which all the constraints applied to the OAR are treated as hard constraints. Objectives placed to the target might not be met during optimization if the constraints are too restrictive. Then, a pareto mode, in which priority is placed on target underdose constraints, is secondly used. The final desired result is that the dose given to the target corresponds to the maximum effective dose under the given constraints.

Monaco® provides a set of biological and physical cost functions [90]. The biological cost functions take advantage of the biological volume effect of structures. Therefore, it allows forecasting the radiation effects on tissues enabling the estimation of the radiation treatment efficacy. The physical cost function is based on dose calculation results and in here all structures are treated as if they have the same dose response mechanism. Summary of the optimization prescription for all H&N patient VMAT plans is denoted in Table 3.3. BrainStem_3mm and SpinalCord_3mm denotes BrainStem and SpinalCord contours expanded by 3mm uniformly in all directions.

Table 3.3: Defined VMAT plan contraints for all 3 H&N patients. Parameters for each cost function are presented in intervals according to the minimum and maximum values used for all patients. D stands for dose, V for volume and SM for Shrink Margin.

Constraints		
Structure	**Cost Function**	**Details**
PTV1	Target Penalty	D= 6250-6300 cGy; V= 95%
	Target Penalty	D= 6000-6050 cGy; V= 98%
	Maximum Dose	D=7150-7250 cGy
PTV2	Target Penalty	D= 5100-5150 cGy; V= 95%
	Target Penalty	D= 4850-4900 cGy; V=98%
	Maximum Dose	D= 6000-6200 cGy
LParotid	Serial	D= 3000-3500 cGy; k= 1; SM=0.5-2 cm
RParotid	Serial	D= 3000-3750 cGy; k= 1; SM=0.5-1 cm
BrainStem	Maximum Dose	D= 5400-5600 cGy
BrainStem_3mm	Maximum Dose	D= 5600-5800 cGy
SpinalCord	Maximum Dose	D= 4100-4300 cGy
SpinalCord_3mm	Maximum Dose	D= 4300-4500 cGy
External	Quadratic Overdose	D= 5000-5250 cGy; RMS= 500 cGy; SM=1-2 cm
	Quadratic Overdose	D= 4750-5000 cGy; RMS= 200 cGy; SM=1.5-2.5 cm
	Maximum Dose	Dose= 6000-6250 cGy

For all patients, the structure layering order was the same as the one stated in Table 3.3. In Monaco®, the layering order determines how the optimizer treats the voxels in overlapping volumes. Thus, voxels in an overlapped region are assigned with the structure that is listed higher. Cost functions associated with that structure will be applied to that region and the same happens if there is no cost function assigned to it.

Target Penalty is a physical objective cost function that uses a threshold dose value that must be met at least by the percentage of volume specified. For this cost function, a Surface Margin of 0.3 cm was applied. When selecting a Surface Margin, the cost function will only be applied to voxels inside the structure with the exception of the voxels that lie within the margin distance (Figure 3.12). Surface Margin is usually applied for superficial targets as it lets the cost function essentially ignore the low dose in a structure where it intersects the build-up region, resulting in a more homogeneous target dose. Also, an Auto Flash margin of 0.2 cm was applied to this cost function to improve target coverage (Figure 3.13). When selecting Auto Flash option, a flash margin of voxels that extends beyond the target volume in the direction of the skin surface is created to avoid the build up region to be happening inside the target.

Maximum dose is a physical constraint that sets a maximum dose that cannot be exceeded in any voxel in the structure. For SpinalCord, SpinalCord_3mm, BrainStem and BrainStem_3mm ROIs an option 'Optimize over all voxels' was selected to give priority to this constraint compared to others regardless of the structure layering order (Figure 3.14). This means that if there is any overlap between two different structures with different cost functions, both functions will be applied to the overlapped voxels.

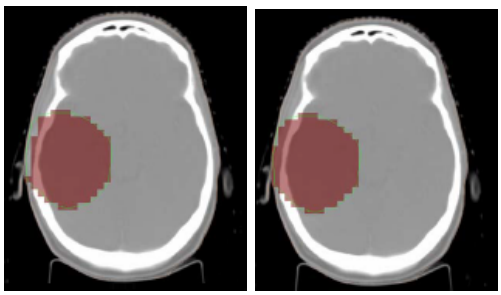

(a) (b)

Figure 3.12: Representation of Surface Margin option in Monaco®. This figure shows the cost function occupancy where a 0.5 cm Surface Margin was applied (a) and the same cost function occupancy without Surface Margin (b). Only the voxels shaded in red are optimized [90].

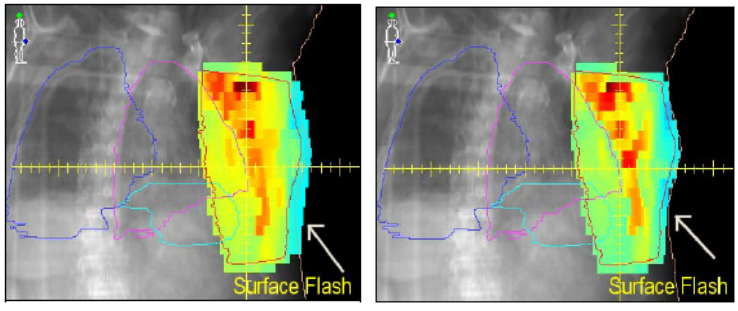

(a) (b)

Figure 3.13: Representation of Auto Flash option in Monaco®. This figure shows the dose distribution occupancy where a 1 cm Auto Flash margin was applied (a) and the same dose distribution occupancy without Auto Flash margin (b) [90].

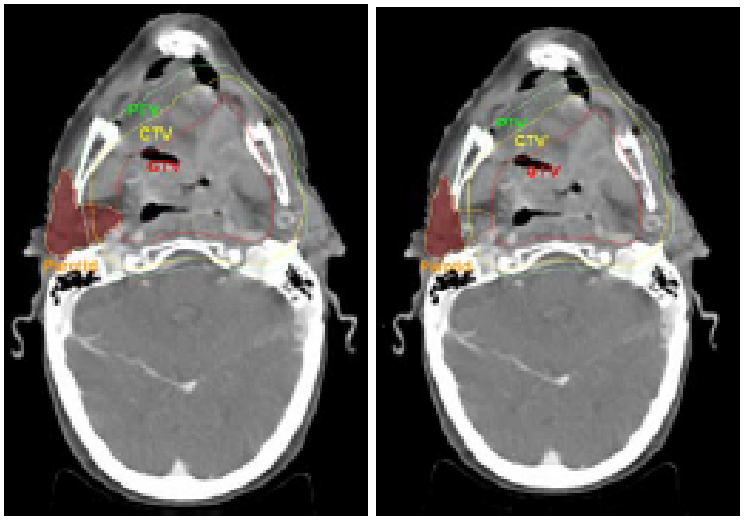

(a) (b)

Figure 3.14: Representation of 'Optimize over all voxels' option in Monaco®. In this figure, one can see a situation where the GTV (red), CTV (yellow) and PTV (green) overlap the parotid (orange) for one representative H&N patient. The cost function occupancy when 'Optimize over all voxels' was applied is shown in (a) and the same cost function occupancy without using 'Optimized over all voxels' option is shown in (b). The cost function is only applied to voxels shaded in red [90].

Serial cost function is a biological function that is responsible of evaluating the damage to the organ caused by the delivered dose. This function requires entering two parameters: the Power Law Exponent (k) and Equivalent Uniform Dose (EUD). The EUD is the dose that causes the same damage if applied uniformly to the entire volume. k is the volume-effect parameter and the higher it is the less tolerance is given to excessive damage to small volumes of the structure. As a k value equal to 1 was assumed, the EUD selected specifies the mean dose given to the organ as low dose and high dose volumes in the structure are equally weighted.

Finally, the Quadratic Overdose is a physical cost function that can be used to limit high doses. It requires setting two parameters: the Maximum Dose and the Root Mean Square (RMS) Dose Excess. The Maximum Dose denotes the dose beyond which a penalty is incurred and RMS Dose Excess is the average tolerated dose violation. This function was applied to the external tissue to limit the effect of the constraints to voxels near the target volume ensuring this way a conformal dose distribution.

To Serial and Quadratic Overdose cost functions, a Shrink Margin was applied. As the PTV1 and PTV2 were defined adjacent and even overlapping the right and left parotid ROIs, competing cost functions were present (Figure 3.10). The application of a Shrink Margin will move the dose gradient out of the target and into the competing structure enabling the voxels near the target and competing structures to have a 'transition zone' between competing cost functions (Figure 3.15).

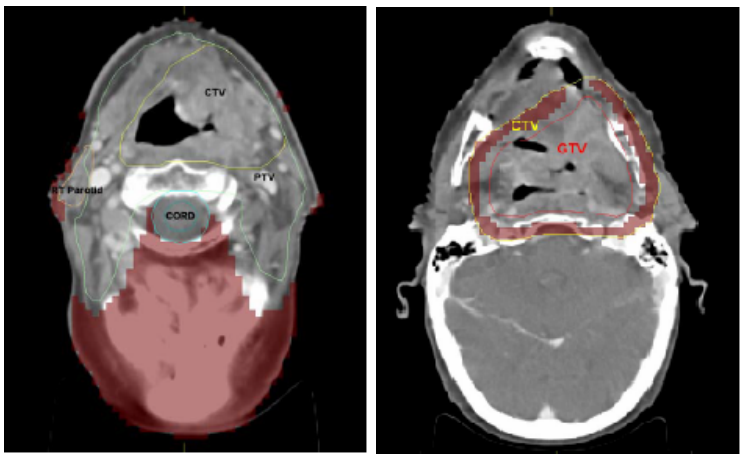

(a) (b)

Figure 3.15: Representation of Shrink Margin option in Monaco®. (a) shows the cost function occupancy for the unspecified tissue where a Shrink Margin was applied and (b) shows a situation where the GTV is inside the CTV and a Shrink Margin was applied to the cost function of the CTV. The cost function is only applied to voxels shaded in red [90].

3.4.2.3 Calculation Properties

The first stage of the optimization was performed with fast pencil beam algorithm, whereas stage two is a final dose calculation performed on a 0.25 cm^3 grid with a Monte Carlo-based algorithm (1% statistical uncertainty per plan).

The first algorithm is used to optimize the ideal fluence distribution of sectors in VMAT plans. This optimization stage changes each cost function's relative weight until all constraints are met or the weighting hits a pre-determined threshold, at which time the constraint is identified as infeasible. In stage two, the ideal fluence distribution is translated into a set of segments where shapes and weights are optimized based on the same dose prescription (Figure 3.16). For VMAT plans the system will then convert the optimized fluences into a deliverable arc sequence with multiple control points (max 180 control points per arc) defining the obtained segments.

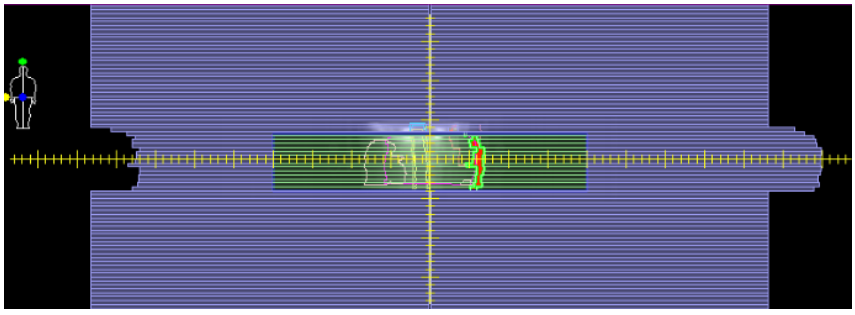

Figure 3.16: Representation of optimization stage two in Monaco® [90].

To account for the effect of the presence of a magnetic field for Monte Carlo dose calculations, GPUMC dose engine was used selecting 'Include Magnetic Field' option on. The field strength was defined to be both 0.5T and 1.5T in the z direction (pointing towards the observer considering an observer facing the gantry). 'Transport Through MRI Housing' option was turned on to generate particles outside the cryostat and perform full Monte Carlo particle transport through the MRI cryostat. The 'Electron Max Step Length (cm)' option denotes the maximum step length that the dose calculation will allow an electron to take and it was defined to be equal to 0.75 cm.

3.4.3 Magnetic Field Induced Dose Effects Evaluation

For the evaluation of the influence of a magnetic field, only a dosimetric approach was developed. The evaluation was performed for all the available scans using the clinical contours delineated on the planning CT as before (see section 3.3.1). The calculated dose distributions were evaluated using the exported dose and structures DICOM files and DICOM-RT-based toolbox [86] in MATLAB.

First, absolute DD maps between the situation with and without a magnetic field for the whole body outline were obtained. Two different maps were created varying in the strength of the magnetic field used: 0.5T - 0T and 1.5T - 0T. This dosimetric evaluation also included DVH analysis on the following contours: PTV1, PTV2 and SpinalCord. The DVH analysis included overlaying the 0T-, 0.5T- and 1.5T- DVH's for the previous contours. A DVH point analysis using an absolute DD between a situation with and without a magnetic field was also performed for the DVH points in Table 3.4.

To evaluate the overall effect of the presence of a magnetic field, the percentage volume in which the dose difference between situations with a magnetic field turned on - 0.5T and 1.5T – and without a magnetic field was bigger than 5%, 10% and 20% of the prescribed dose was calculated for each patient. Finally, the maximum dose increase caused by the ERE was calculated and the results were presented in a percentage regarding to the maximum dose in a B=0T scenario. In this evaluation, a statistical analysis was not performed as the sample size was too small to have sufficient statistical power.

Table 3.4: Evaluation of MR field induced dose effects: Analyzed DVH points summary for all 3 H&N patients.

ROI	Volume Definition	DVH Points
PTV1	Target Volume	D50%; D2%
PTV2	Target Volume	D50%
SpinalCord	Serial OAR	D50%

Chapter 4

Results and Discussion

The present chapter summarizes the results from the data analysis and the discussion of the achieved information. Due to the large amount of data analysed, only some results obtained from individual slices of representative patients and interval of values were selected to be shown.

This chapter is divided into three main parts:

A.1 Dosimetric results for the H&N and the prostate patients when comparing dose distributions on the sCT against dose distributions on the planning CT;

A.2 Geometric results for the H&N and the prostate patients when comparing CT, MRI and sCT_a based contours;

A.3 A comparison of magnetic field induced dose effects calculated based on sCT and calculated on the original CT for the H&N patients.

A discussion of the results is included in each subchapter.

4.1 Dosimetric Results

The dosimetric evaluation was implemented to see differences in clinical dose calculations resulting when using real electron density values obtained with the planning CT against when using estimated electron density values obtained by the generation of the sCT's.
The results of this part of the study are divided in 3 parts for both H&N and prostate patients:

B.1 Dose Difference Map Analysis;

B.2 Gamma Analysis;

B.3 Dose Volume Histogram Analysis.

The results for the prostate patient who has a metal implant are presented separately. This patient case is only addressed in parts B.1 and B.2 of the analysis.

4.1.1 Head and Neck Patients

4.1.1.1 Dose Difference Analysis

The DD maps were obtained for one representative patient and the same slice was chosen for all the performed comparisons between the dose distributions calculated on the CT and on the sCT_{bda}-CTinfo, sCT_{bda}-T1-MRinfo, sCT_{bda}-T2-MRinfo, sCT_a and sCT_a-bref, respectively. The selected slice was chosen within the MRI FOV, excluding areas with a lack of coverage (see section 3.2.3). Similar results were obtained for the remaining patients. The maps in Figures (4.1 - 4.3) show absolute dose differences (-5 to 5 Gy).

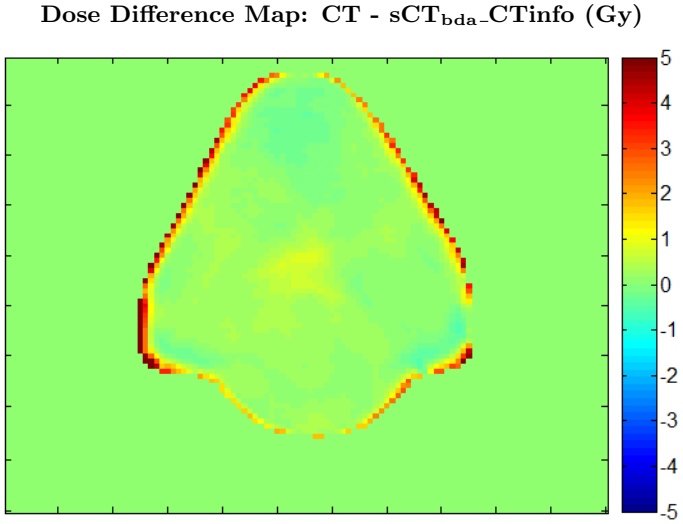

Figure 4.1: DD map for CT – sCT_{bda}-CTinfo for one representative H&N patient (scale in Gy).

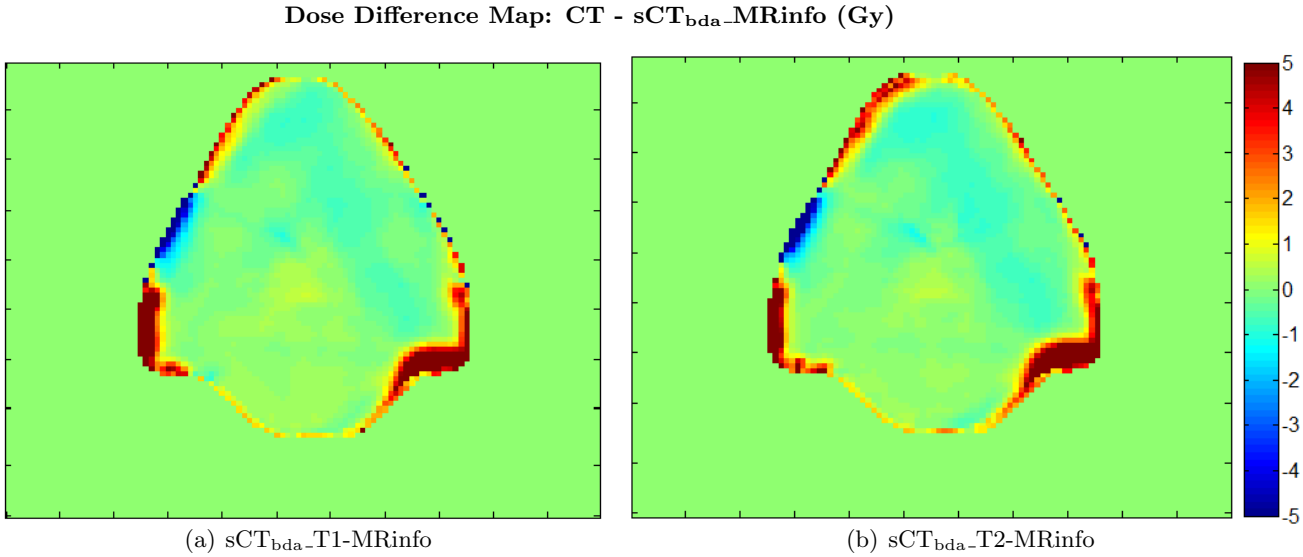

(a) sCT_{bda}-T1-MRinfo (b) sCT_{bda}-T2-MRinfo

Figure 4.2: DD map for CT – $sCT_{bda\text{-}T1\text{-}MRinfo}$ (a) and sCT_{bda}-T2-MRinfo (b) for one representative H&N patient (scale in Gy).

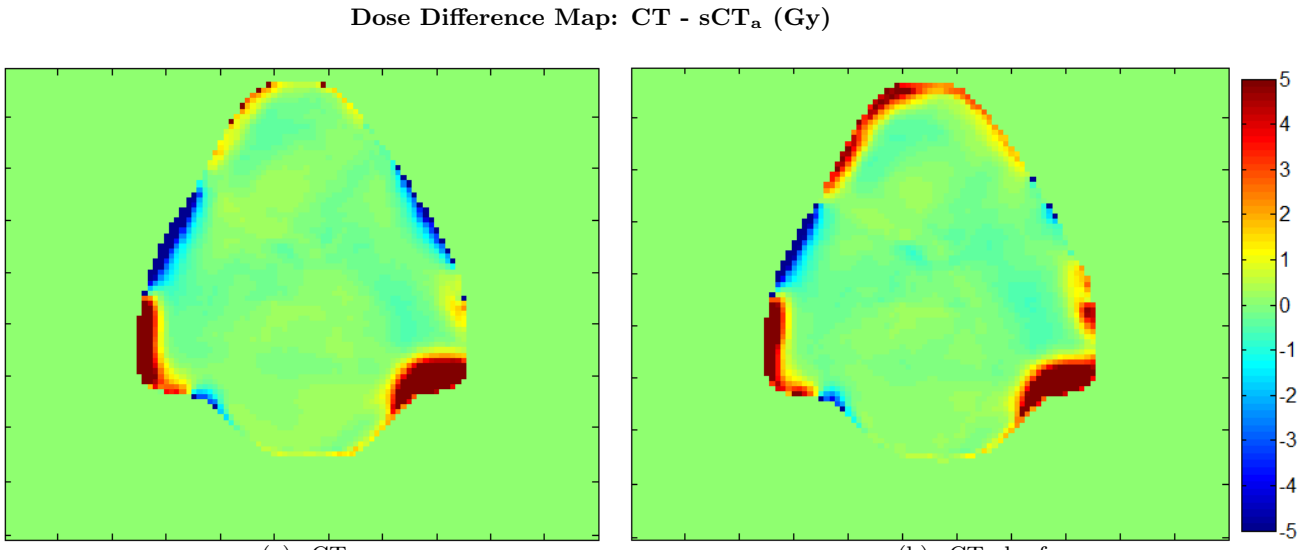

(a) sCT_a (b) sCT_a_bref

Figure 4.3: DD map for CT – sCT_a (a) and sCT_a_bref (b) for one representative H&N patient (scale in Gy).

For sCT_{bda}_CTinfo in Figure 4.1, a constant difference around the edges reaching a maximum of 5 Gy in the most superficial voxels can be seen. Despite the fact that the external contour was the same for both scans, this slight difference is possibly a result of registration inaccuracies and different voxel resolution that may cause alterations in the contour shape when performing a rigid copy from the CT to the MRI scans. For T1 and T2-MRinfo sCT_{bda} (Figure 4.2) and also for sCT_a and sCT_a_bref (Figure 4.3) larger differences are observed in the patient outline with a maximum of 5/-5 Gy. This is mainly due to the use of different external contours. The differences stated by the red colour on the dose scale are dominant and indicate an extension of the CT outline compared to both sCT_{bda}_MRinfo and sCT_a while differences specified by the blue colour on the dose scale indicate the opposite. These differences are going to be explained in more detail in section 4.2.1.

Comparing calculations considering all different sCT methods, one can see that the main dose differences are introduced by external delineation differences. Despite these differences, a similar dose distribution is obtained for the PTV region within the patient with a maximum difference of 1/-1 Gy for all methods, which is approximately 1.5% of the prescribed dose and thus considered insignificant for clinical purposes. In Figure 4.1, for sCT_{bda}_CTinfo an underdosage can be seen in the PTV region illustrated by the positive difference (in yellow) while for the remaining methods (Figure 4.2 and 4.3) an overdosage is seen, denoted by a negative dose difference (in blue). This overdose estimation is more dominant for both T1 and T2-MRinfo sCT_{bda}.

4.1.1.2 Gamma Analysis

A gamma analysis was performed for 2 combinations of DTA and DD values (see section 3.3.1): 3mm_3% and 2mm_2%. The range of percentage of points in the patient's outline that fulfil the gamma criteria will be denoted for both combinations. The gamma maps in Figures 4.4 - 4.8 display results for the 2mm_2% criteria. Points denoted in red indicate gamma values bigger than 1 and so the points that fail the criteria.

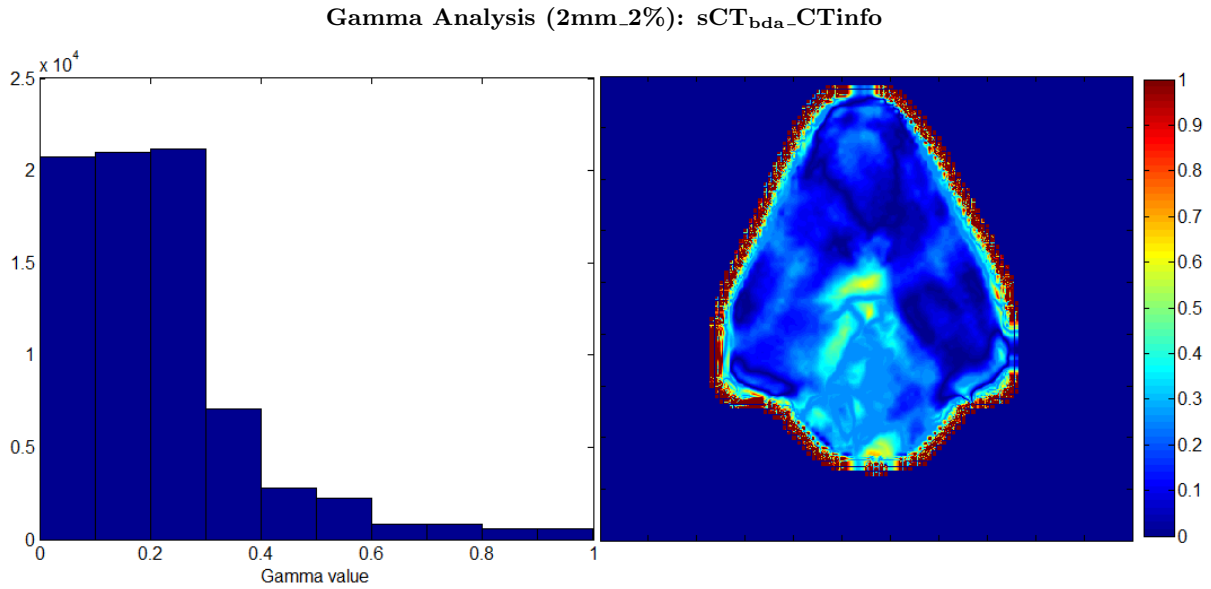

Figure 4.4: Gamma map performed for a combination of 2mm DTA and 2% DD for sCT$_{bda}$_CTinfo (right) and respective gamma histogram (left) for one representative H&N patient.

In the sCT$_{bda}$_CTinfo gamma map (Figure 4.4), it's possible to see that the majority of points (91.7%) passes the criteria with only some points in red at the patient outline falling. This confirms the results given by DD maps in Figure 4.1. When using a broader acceptance criteria combination of 3mm_3%, the percentage of points that passes the gamma test increase to 94.5%.

For T1- and T2-MRinfo sCT$_{bda}$ (Figure 4.5 and 4.6, respectively), one can see a greater number of points failing at the extremities of the patient, due to the external outline differences, also represented in the DD maps seen before. In the PTV region, a greater dissimilarity is seen with gamma values between 0.3 and 0.8. This can be explained by the air and bone delineation being performed manually on the MRI scans, leading to different results than the automatic delineation of the contours on the planning CT used for sCT$_{bda}$_CTinfo. The percentage of points that passes the gamma criteria is equal to 88.0% for sCT$_{bda}$_T1-MRinfo and 87.9% for sCT$_{bda}$_T2-MRinfo for a 2mm_2% gamma test. When using 3mm_3% criteria, these percentages increase to 92.3% and 91.9%, respectively. Although the percentage of passing points is similar for both methods, a more heterogeneous gamma map is obtained for sCT$_{bda}$_T2-MRinfo. Here a greater number of points have gamma values greater than 0.4, represented in a green/yellow colour on the gamma map and also on the gamma index histogram in Figure 4.6.

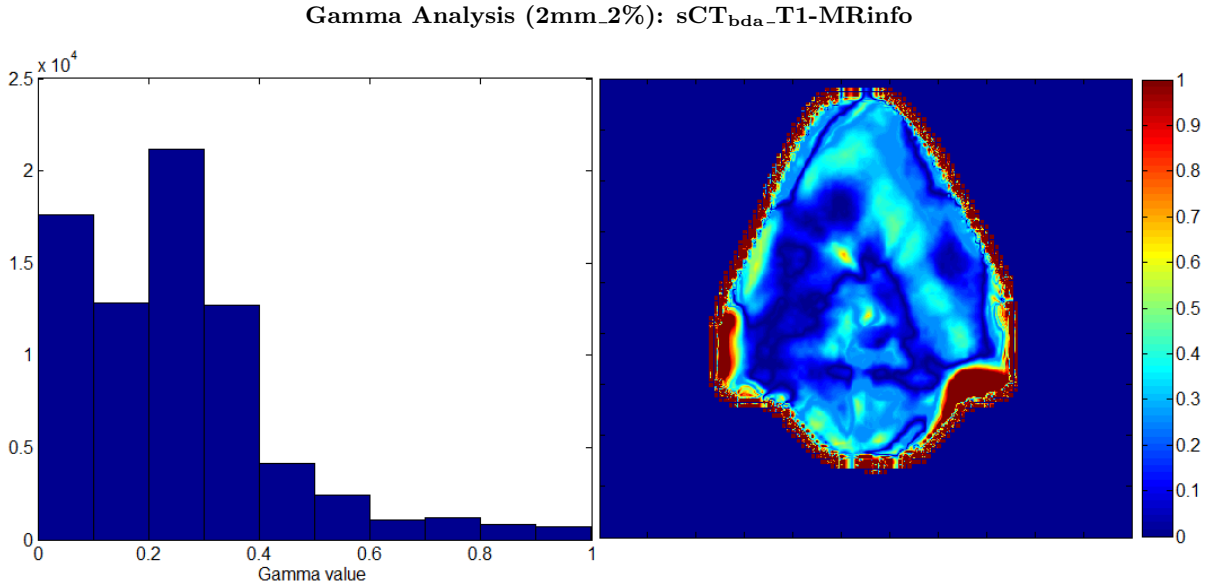

Figure 4.5: Gamma map performed for a combination of 2mm DTA and 2% DD for sCT_{bda}_T1-MRinfo (right) and respective gamma histogram (left) for one representative H&N patient.

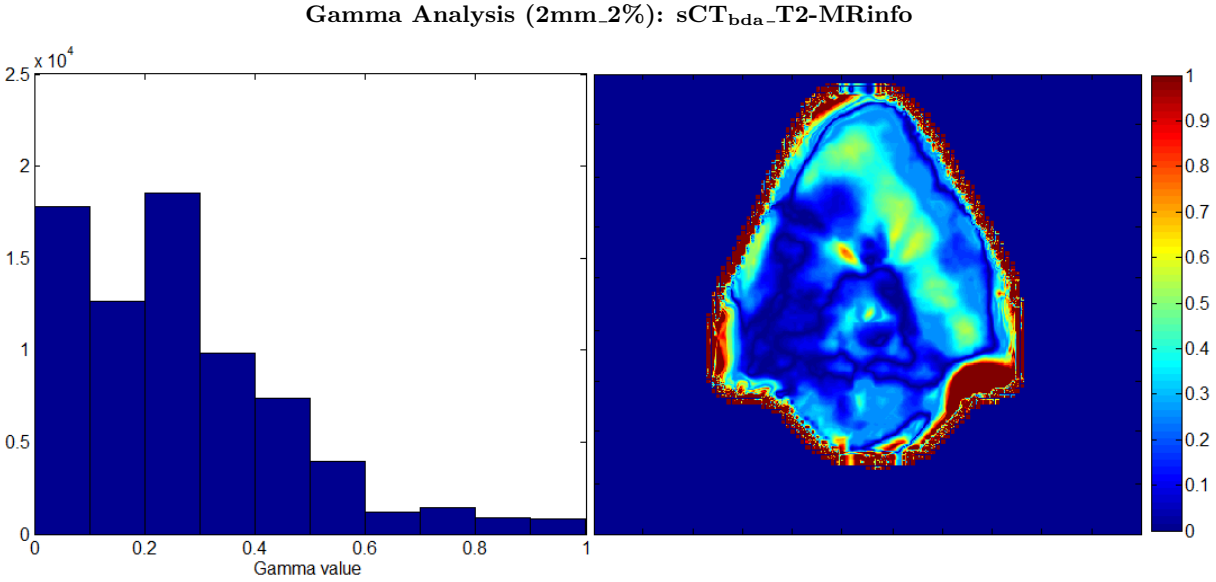

Figure 4.6: Gamma map performed for a combination of 2mm DTA and 2% DD for sCT_{bda}_T2-MRinfo (right) and respective gamma histogram (left) for one representative H&N patient.

As for sCT_{bda}_MRinfo, both sCT_a and sCT_a_bref show a higher number of points failing the criteria close to the edges. However, when using these Atlas methods, a greater similarity with the CT dose distributions is achieved in general. A greater number of small gamma values (0-0.3) and a greater number of points passing is obtained compared to all bulk density methods. For sCT_a method, the pass rate is equal to 88.1% and 92.8% for 2mm_2% and 3mm_3% criteria, respectively and it is 88.7% and 92.9% for sCT_a_bref, respectively. Similar results are achieved for sCT_a and sCT_a_bref and dose recalculations on both show the greatest dose similarity to the calculations on the initial planning CT in the PTV region.

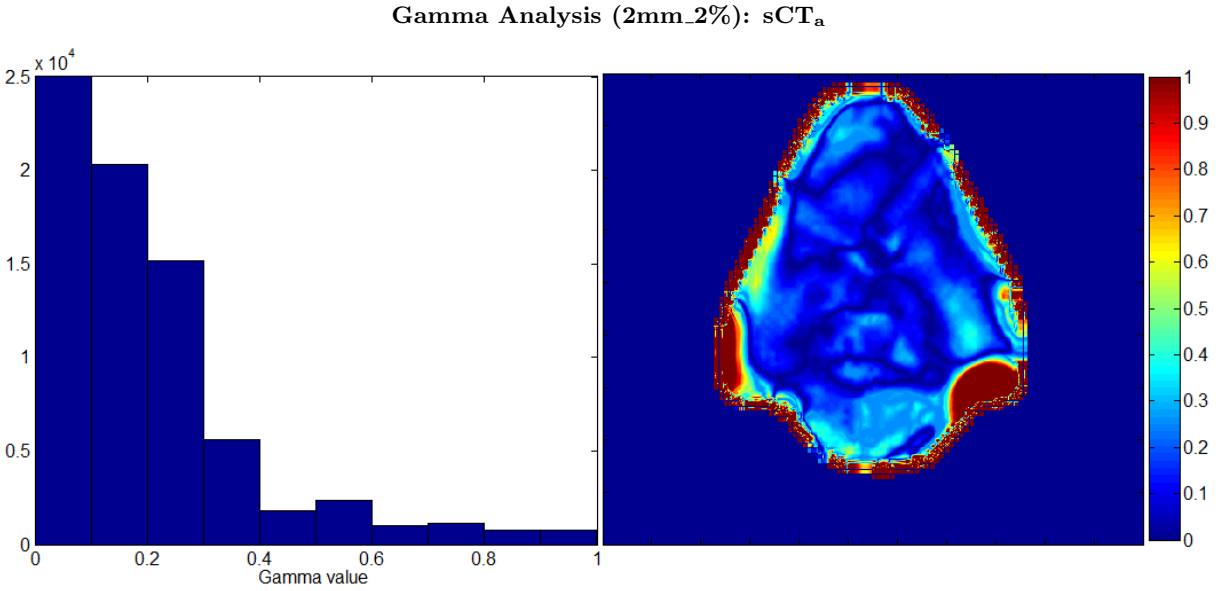

Figure 4.7: Gamma map performed for a combination of 2mm DTA and 2% DD for sCT_a (right) and respective gamma histogram (left) for one representative H&N patient.

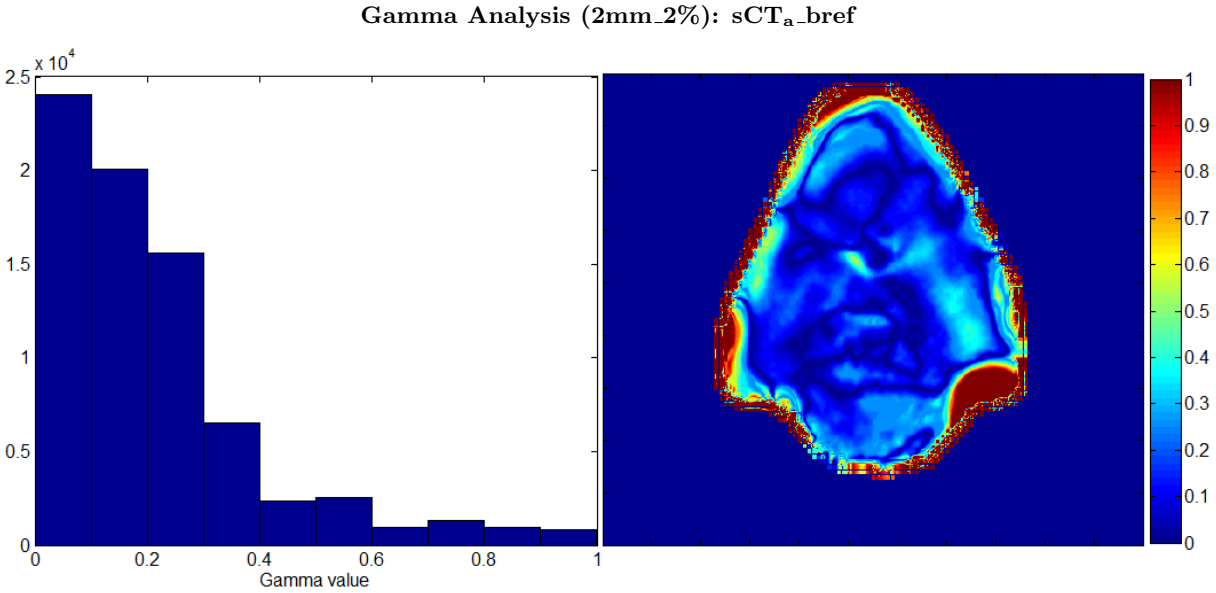

Figure 4.8: Gamma map performed for a combination of 2mm DTA and 2% DD for sCT_a_bref (right) and respective gamma histogram (left) for one representative H&N patient.

4.1.1.3 Dose Volume Histogram Analysis

In this section, a DVH analysis for the H&N patients is presented. The DVHs for the PTV and the OAR - SpinalCord, RParotid and LParotid – were plotted for all 5 sCT used - sCT_{bda}_CTinfo, T1- and T2-MRinfo sCT_{bda}, sCT_a and sCT_a_bref. In Figure 4.9, one can see a comparison of the DVHs, plotted as bands enclosing information for all investigated H&N patients. The DVH bands represent the area enclosed by the envelope of the DVHs of all patients. Each band comprises the mean curve for each method and the maximum and minimum deviation to that curve. As the use of the mean is usually not meaningful and to evaluate the robustness of the plan using each sCT against the CT plan, the bands were used in addition to summarize the statistical deviations of the multiple 3D dose distributions. The DVH bands were plotted using information from all 6 H&N patients as they all had the same prescribed dose of 65 Gy.

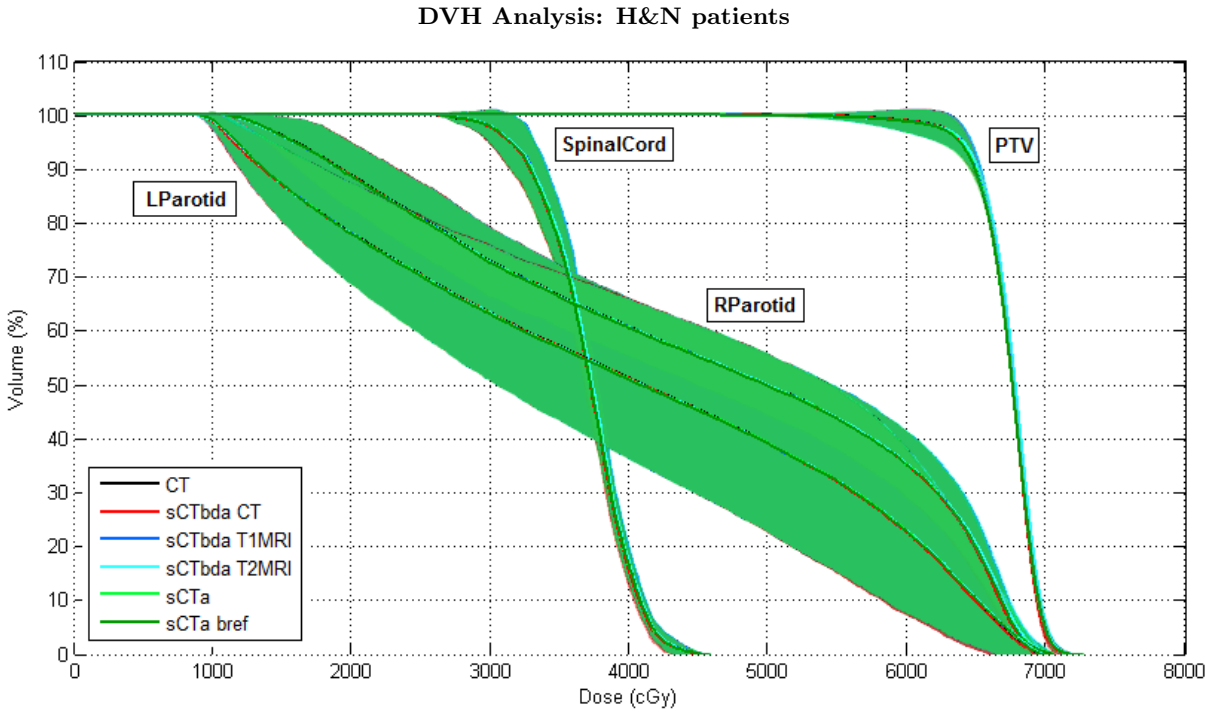

Figure 4.9: DVH bands for all 6 H&N patients plotted for CT (black) and the remaining 5 sCT dose distributions: sCT_{bda}_CTinfo (red), sCT_{bda}_T1-MRinfo (blue), sCT_{bda}_T2-MRinfo (cyan), sCT_a (lime), sCT_a_bref (green). The bands were plotted for the following ROIs represented from left to right: Lparotid, Rparotid, SpinalCord and PTV.

The overall shape of the DVH bands derived using both CT and each sCT dose distributions are very similar as it's possible to see in Figure 4.9. To have a clear idea of the differences between using each sCT scan a zoom was performed at the dose gradient of the DVHs. The results are presented for the PTV and the SpinalCord contours in Figures 4.10 and 4.11, respectively.

For the PTV contour (Figure 4.10), it's clear to see a greater similarity between the mean curve for CT, sCT_a and sCT_a_bref methods, whose envelops (in black and green, respectively) are in the majority overlaid. For sCT_{bda}_CTinfo, method a slight underdosage estimation is observed. The opposite occurs for both sCT_{bda}_MRinfo methods whose envelops (in blue) do not even coincide with the CT envelope denoting an overestimation of the dose given to the PTV contour. Despite these differences, the deviations between the PTV mean curves of the sCT methods and CT were insignificant with an absolute maximum deviation of approximately 0.3 Gy, which is considered clinically insignificant for a 65 Gy prescribed dose.

For all OAR, the results are similar to the following presented one. In Figure 4.11, a zoom for the DVHs of the SpinalCord contour is presented in which a great similarity between DVH bands based on sCT_a scans and DVH bands from the original CT can be observed. A slight overestimation is seen when using sCT_{bda}_MRinfo scans and a sligth underestimation can be seen for sCT_{bda}_CTinfo. These DVH results for the H&N patients are consistent with the results for DD and gamma maps previously shown.

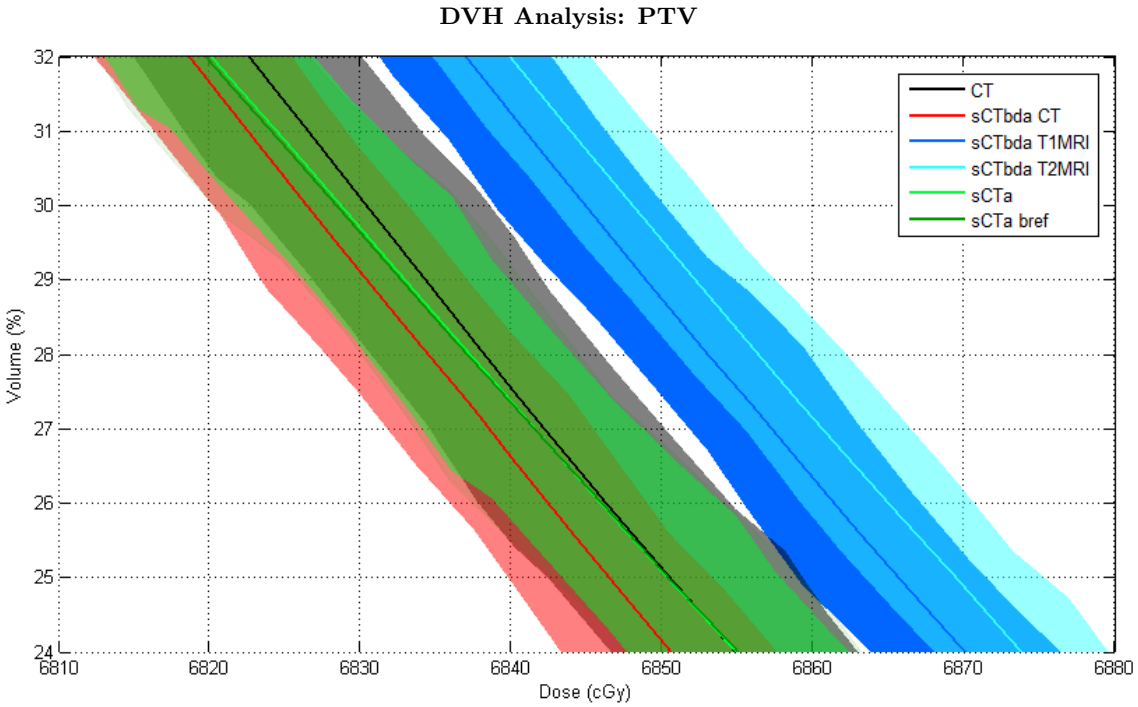

Figure 4.10: Performed zoom on the drop curve of the DVH for PTV ROI.

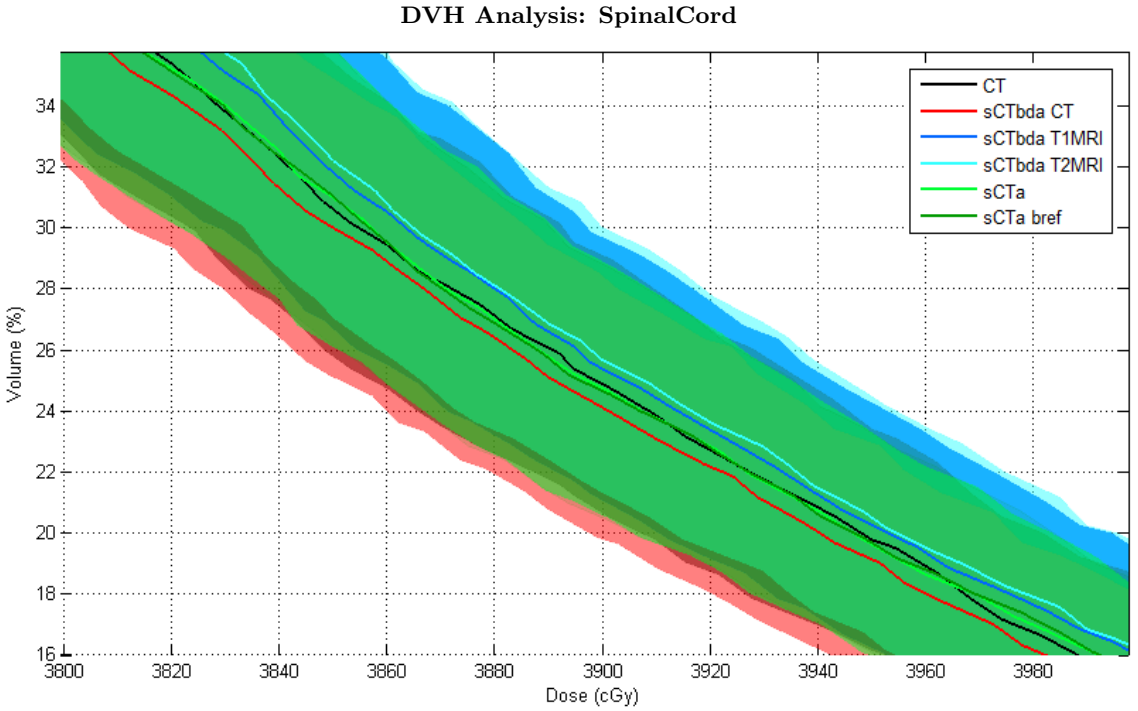

Figure 4.11: Performed zoom on the drop curve of the DVH for SpinalCord ROI.

A DVH point percentage difference was performed using data from all 6 patients and for the DVH points stated previously in Table 3.1 in section 3.3.1. The percentage difference results will be discussed here using absolute values without regarding to the signal stated by the difference.

For the PTV contour, using D98%, Dmean and D2%, it's difficult to denote any trends when using different sCT methods (Figures 4.12 - 4.14). The maximum percentage difference for D98% is about 2%. For Dmean and D2% it's equal to about 1%. As there is not an explicit

acceptable dose difference defined in clinical practice, adequate deviations for the DVH points should be established. According to reference [48], a 2% dose calculation deviation for 95% of the patients is usually acceptable. Hence, in this study the sCT methods for the H&N as well as for the prostate patients will be considerable clinical acceptable if 95% of the patients have a dose calculation deviation of 2% or less. This threshold was used for both PTV and OAR DVH points. So, it's possible to see that the results seen in Figures 4.12 - 4.14 for the PTV contour are within the clinically acceptable deviation.

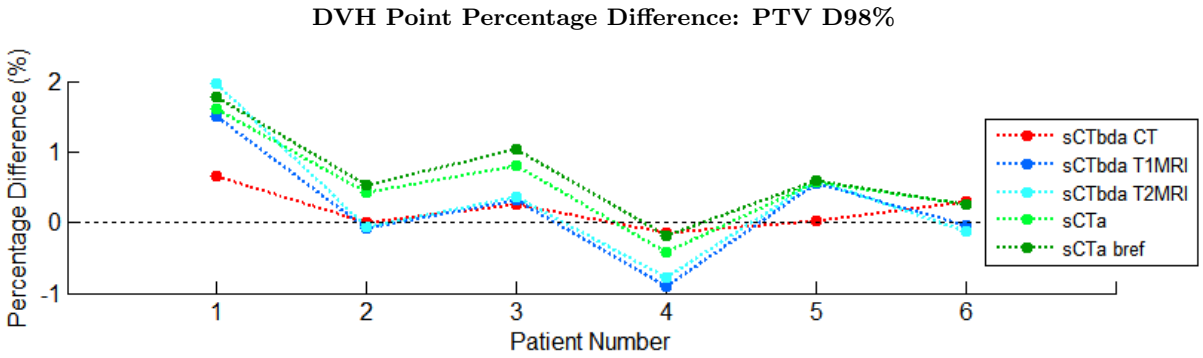

Figure 4.12: DVH point D98% percentage difference for PTV ROI for CT and sCT plans for all 6 H&N patients.

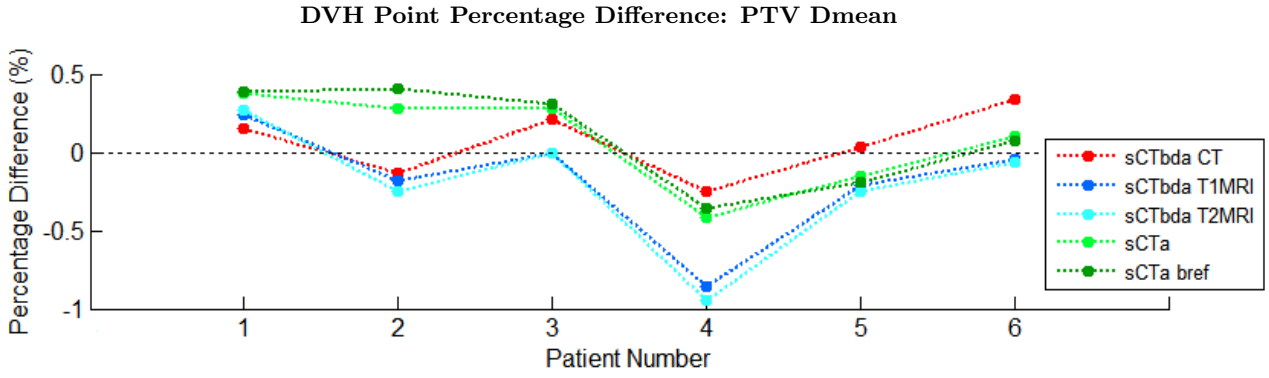

Figure 4.13: DVH point Dmean percentage difference for PTV ROI for CT and sCT plans for all 6 H&N patients.

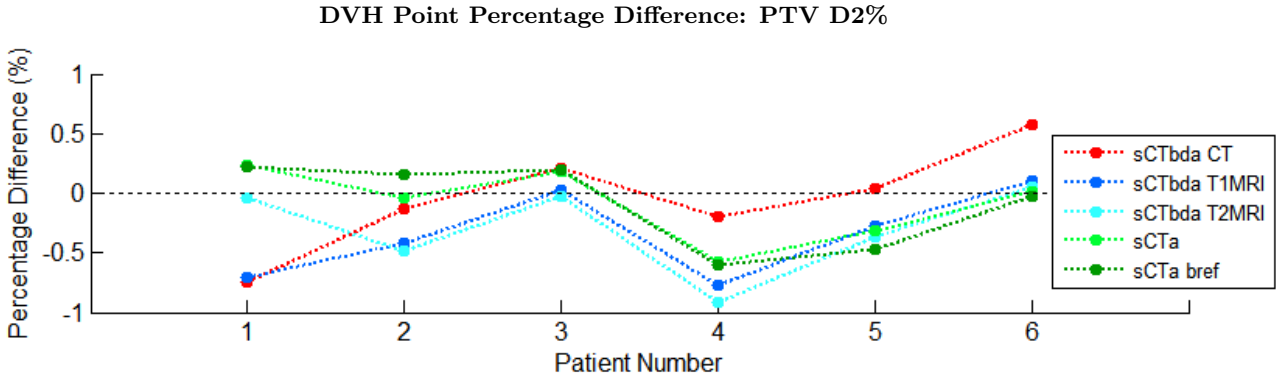

Figure 4.14: DVH point D2% percentage difference for PTV ROI for CT and sCT plans for all 6 H&N patients.

For all OAR, the same conclusions can be made (Figures 4.15 - 4.17). The maximum dose difference for both SpinalCord D2%, RParotid Dmean and LParotid Dmean are about 1%.

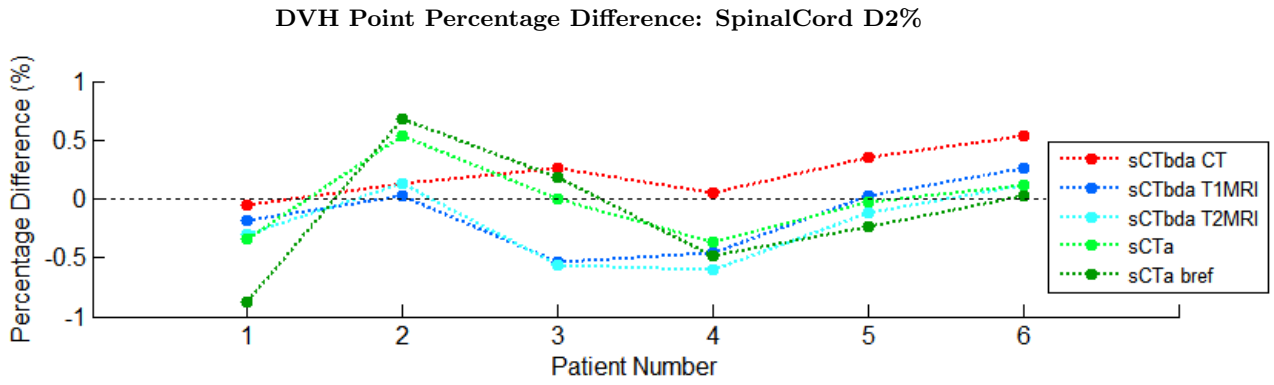

Figure 4.15: DVH point D2% percentage difference for SpinalCord ROI for CT and sCT plans for all 6 H&N patients.

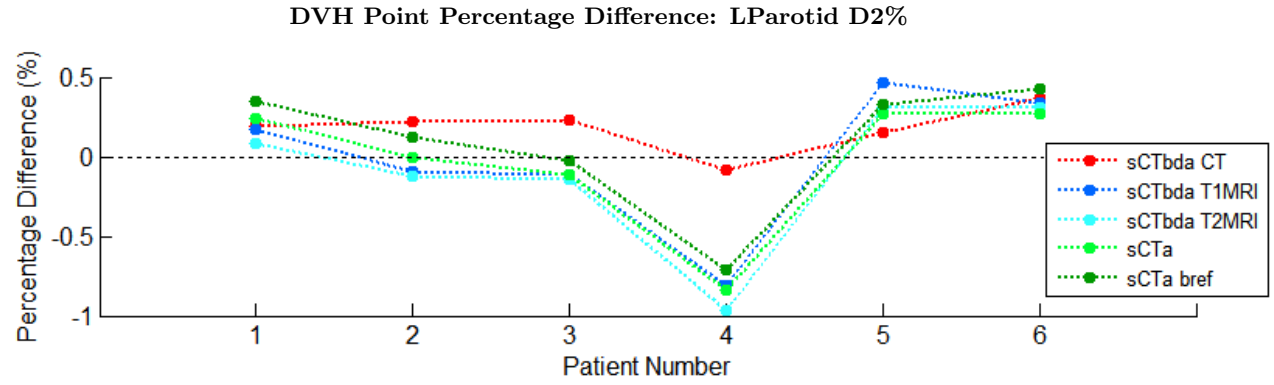

Figure 4.16: DVH point D2% percentage difference for LParotid ROI for CT and sCT plans for all 6 H&N patients.

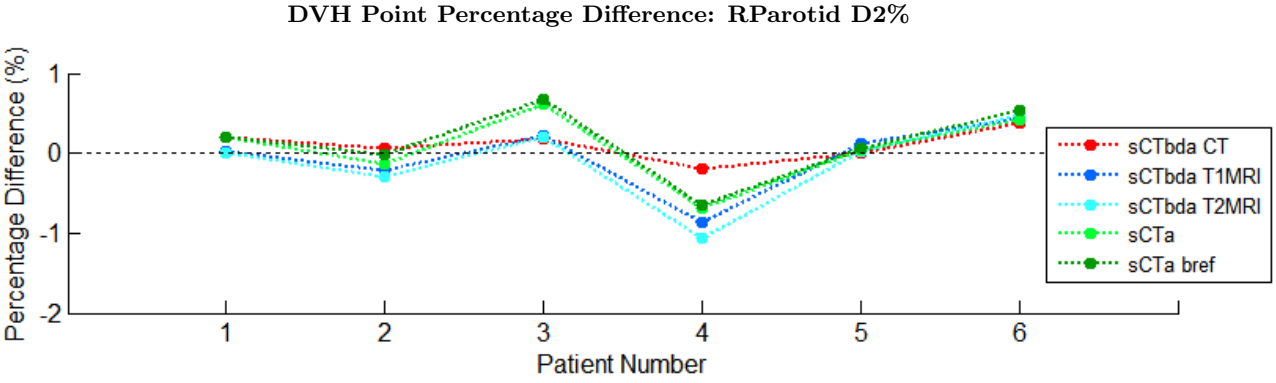

Figure 4.17: DVH point D2% percentage difference for RParotid ROI for CT and sCT plans for all 6 H&N patients.

The results for the statistical analysis of the DVH points dose differences performed using the Kruskal-Wallis test are represented in Table 4.1. The statistical test was applied to all calculated deviations between CT and sCT DVH points. The p-values obtained for each DVH point and for each contour are always greater than the significance level defined (0.01) and so no significant differences are found when using either sCT method for dose calculations compared to the clinical results obtained with the CT plan.

Table 4.1: Results for the Kruskal-Wallis statistical test conducted to deviations (including the signs stated by the difference) in DVH parameters by comparing the DVH points between CT and all used sCT dose distributions for all 6 H&N patients.

DVH Point Percentage Difference CT-sCT		
ROI	**DVH Point**	**p-value for the Kruskal-Wallis test**
PTV	D98%	0.685
	Dmean	0.336
	D2%	0.526
SpinalCord	D2%	0.252
LParotid	Dmean	0.708
RParotid	Dmean	0.850

A further statistical analysis was performed and the results for the mean PTV coverage are displayed using a box plot to determine how the values of the relative dose given to the target are distributed when using the planning CT and each sCT scan for planning (Figure 4.18). The dose is presented as a percentage relative to the prescribed dose for all 6 patients. In Figure 4.18, one can see that the variation of the data is similar for both sCT_{bda}_MRinfo plans and for sCT_a and sCT_a_bref plans, which is expected as the scans were obtained using the same method with slight variations. A clear median resemblance between CT and sCT_{bda}_CTinfo, sCT_a and sCT_a_bref can be denoted, while both sCT_{bda}_MRinfo scans show a slight increased median. This slight overdosage was already seen when evaluating the DVH bands for the PTV contour (Figure 4.10). Despite these small differences observed, the interquartile ranges (height of the boxes) do overlap for all considered plans and so no significant differences between them are found, confirming the p-value result obtained previously.

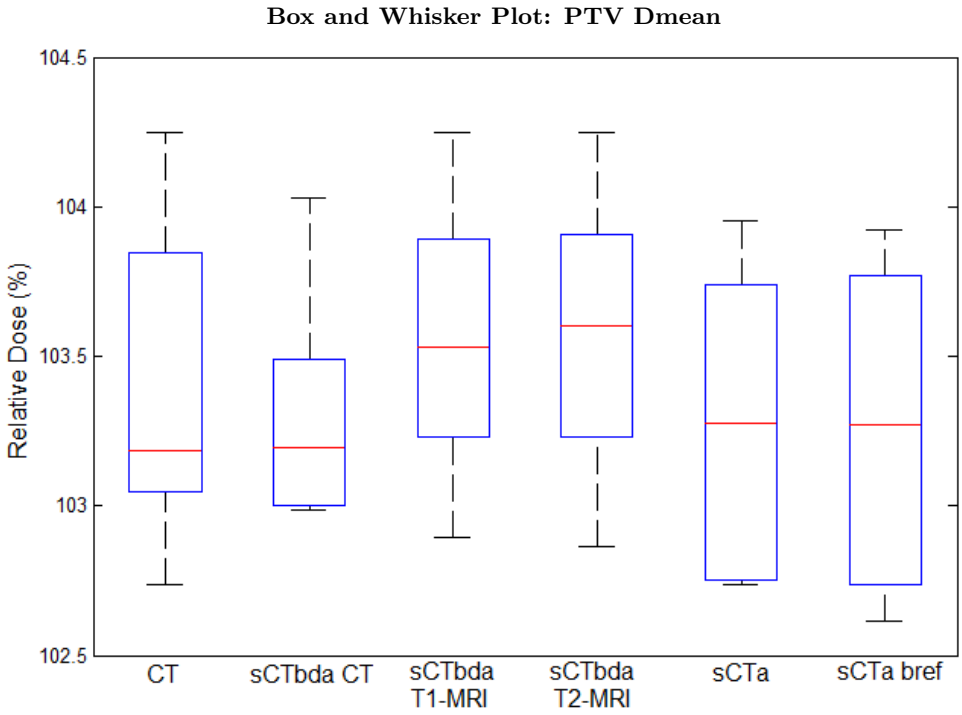

Figure 4.18: Box and Whisker plot for PTV Dmean DVH point for all 6 H&N patients.

4.1.2 Prostate Patients

4.1.2.1 Dose Difference Analysis

As for the H&N patients, DD maps are shown for one representative prostate patient using the same slice within the MRI FOV for all 5 methods. The maps in Figures (4.19 - 4.21) show an absolute dose difference in a range of -3 to 3 Gy.

For sCT_{bda}-CTinfo (Figure 4.19), minor differences at the edges that reach a maximum of 3 Gy can be seen possibly also as a result of registration inaccuracies and different voxels resolution between CT images and MRI, as explained before. These differences are increased when using both sCT_{bda}-MRinfo (Figure 4.20) as for these methods a different external contour was used based on T1- and T2-MRI scans. The biggest differences are seen in the posterior and on the lateral sides of the patient due to the use of different couches during MR and CT imaging. These differences will be explained in more detail in section 4.2.2. For all bulk density methods, a constant difference in the PTV region that reaches a maximum of +2 Gy can be denoted, indicating an underdosage of the PTV for this patient when using sCT dose calculations.

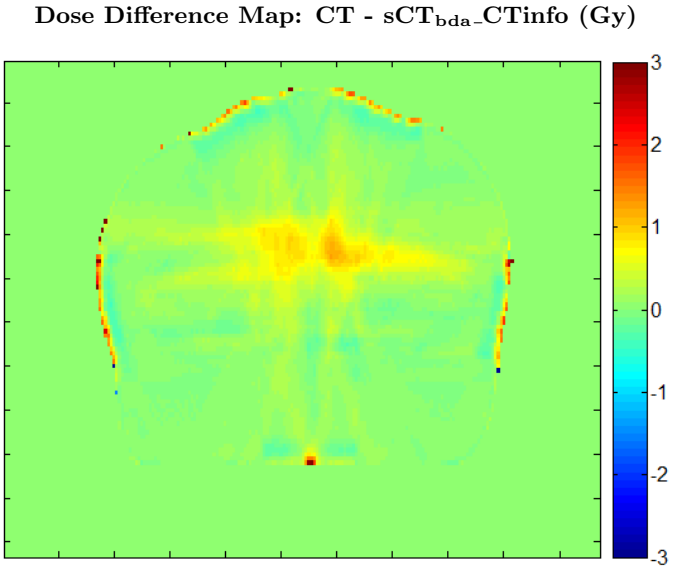

Figure 4.19: DD map for CT – sCT_{bda}-CTinfo for one representative prostate patient (scale in Gy).

For both sCT_a and sCT_a-bref (Figure 4.21), a great similarity with the original CT dose distribution is achieved in the PTV region, with dose differences around [-1,1] Gy, as well as in the outer contour region. Differently from the H&N patients, a better match is seen for the external contours defined on sCT_a scans and on the planning CT (see section 4.2.2). For sCT_a and sCT_a-bref in general similar results are obtained with only small variations at the patient edges.

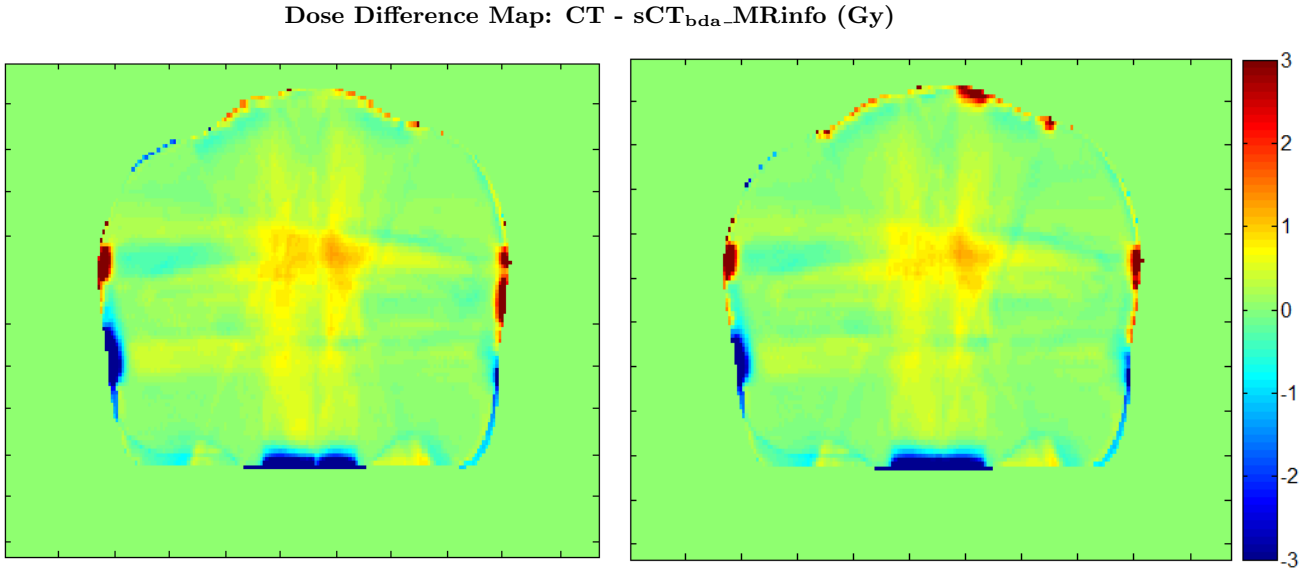

(a) $sCT_{bda\_T1\text{-}MRinfo}$ (b) $sCT_{bda\_T2\text{-}MRinfo}$

Figure 4.20: DD map for CT – $sCT_{bda\_T1\text{-}MRinfo}$ (a) and sCT_{bda}_T2-MRinfo (b) for one representative prostate patient (scale in Gy).

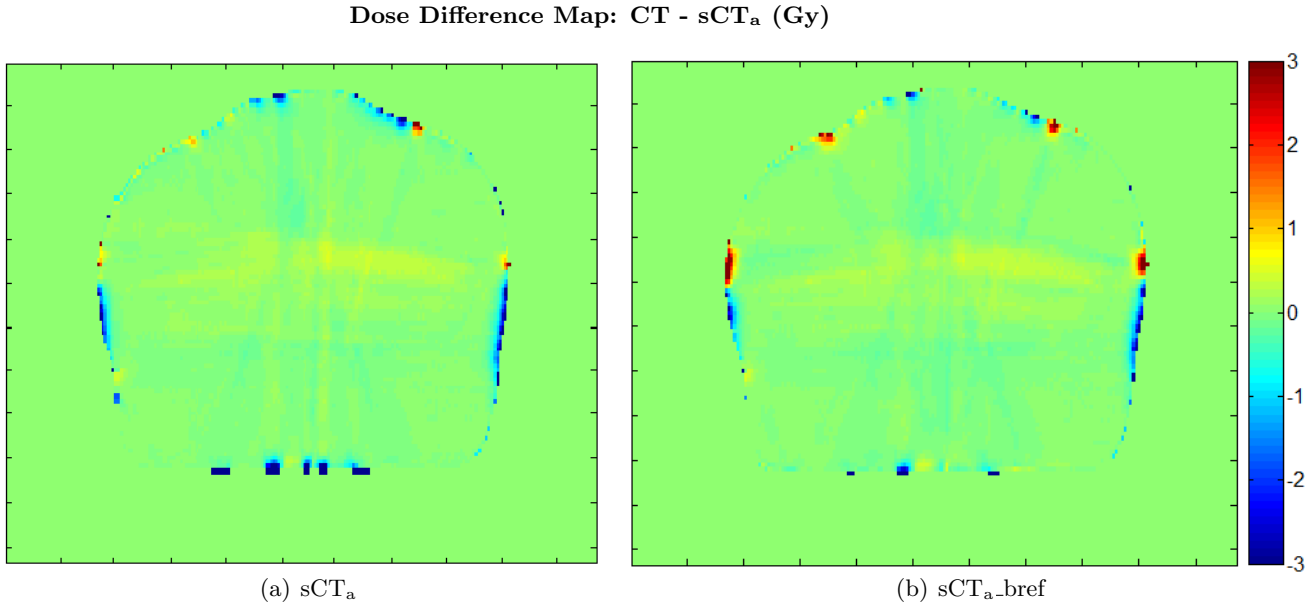

(a) sCT_a (b) sCT_a_bref

Figure 4.21: DD map for CT – sCT_a (a) and sCT_a_bref (b) for one representative prostate patient (scale in Gy).

4.1.2.2 Gamma Analysis

As for the H&N patients, a gamma analysis using 2 combinations of acceptance criteria was performed: 3mm_3% and 2mm_2%. The range of the percentage of points that fulfil the gamma criteria will be denoted for both combinations while the gamma maps in Figures 4.22 - 4.26 are only showing results for the 2mm_2% criteria.

In Figure 4.22, one can see that for the sCT_{bda}_CTinfo the majority of points that fail the criteria (coloured in red) are in the outer contour of the patient. Confirming the DD maps, for the PTV region gamma values of 0.2 - 0.6 are obtained with some points falling the test (gamma

values higher than 1). Despite these differences, the percentage of points that passes the test is elevated and equal to 96.4% for 2mm_2% criteria and 97.8% for 3mm_3% criteria.

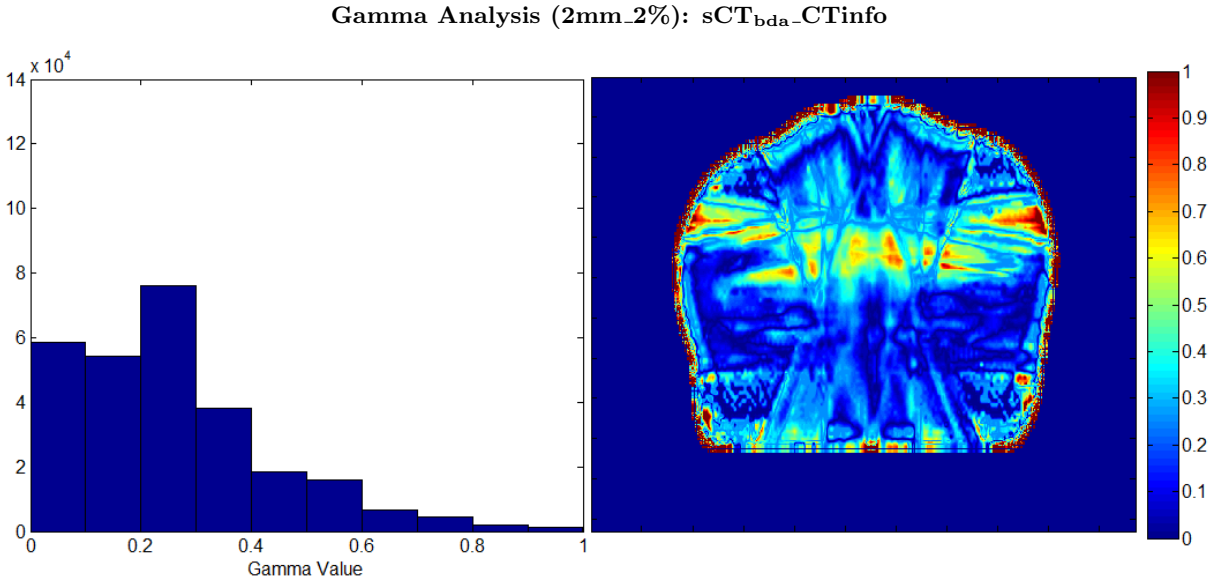

Figure 4.22: Gamma map performed for a combination of 2mm DTA and 2% DD for sCT_{bda}_CTinfo (right) and respective gamma histogram (left) for one representative prostate patient.

For T1- and T2-MRinfo sCT_{bda} (Figures 4.23 and 4.24), the differences on the outer contour are more pronounced with a greater number of points failing the test mainly on the posterior side of the patient, showing the influence of the different couches used during MR and CT imaging. Within the patient gamma values of about 0.2 - 0.8 are obtained, showing some deviations between dose distributions calculated on sCT_{bda}_MRinfo scans and calculated on the original CT scan. Regardless of the more heterogeneous gamma map, a high percentage of passing points is obtained for these methods. For sCT_{bda}_T1-MRinfo 91.5% and 95.1% of the points passes the gamma test using a 2mm_2% and 3mm_3% criteria, respectively. For sCT_{bda}_T2-MRinfo similar percentages are obtained (91.6% and 94.8%, respectively).

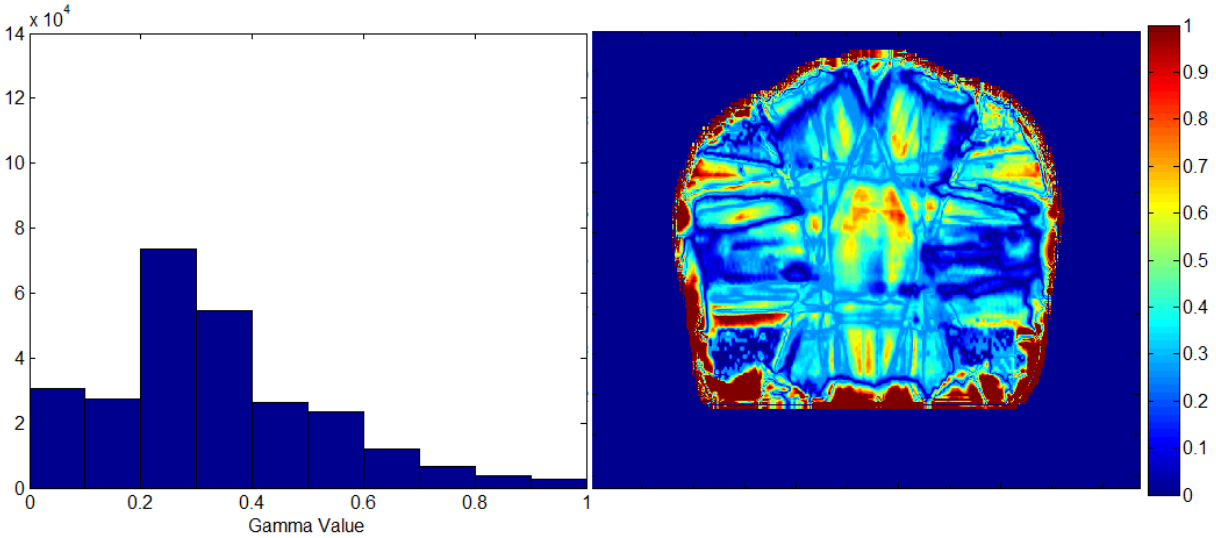

Figure 4.23: Gamma map performed for a combination of 2mm DTA and 2% DD for sCT_{bda}_T1-MRinfo (right) and respective gamma histogram (left) for one representative prostate patient.

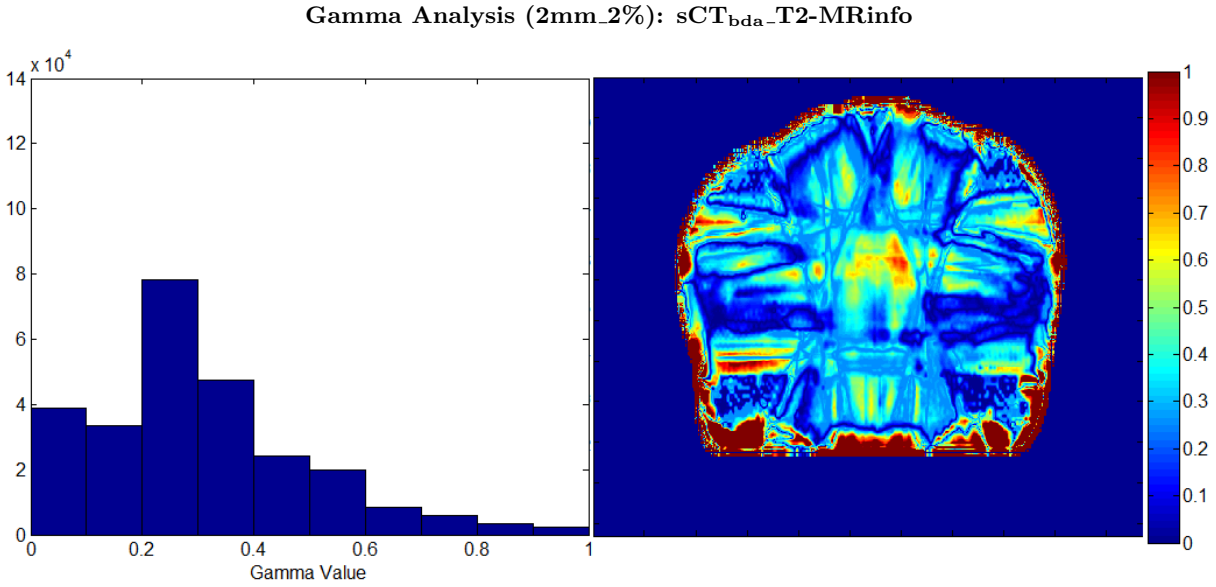

Figure 4.24: Gamma map performed for a combination of 2mm DTA and 2% DD for sCT_{bda}_T2-MRinfo (right) and respective gamma histogram (left) for one representative prostate patient.

For sCT_a and for sCT_a_bref more homogeneous gamma maps are obtained. In the PTV region mainly gamma values between 0 and 0.2 are obtained, as seen in Figures 4.25 and 4.26, which denotes a higher degree of similarity with the CT dose distribution. As for the other methods, the majority of points failing the criteria are situated at the outer contour of the patient. For sCT_a, the passing percentages are equal to 95.9% and 97.7% for a 2mm_2% and a 3mm_3% gamma test, respectively. For sCT_a_bref, a slight passing rate increase is obtained - 96.4% and 98.1%, respectively. As for the H&N patients, it can be seen that when sCT_a methods are used a greater similarity of these dose distributions to real original dose distributions is obtained than for all bulk density methods.

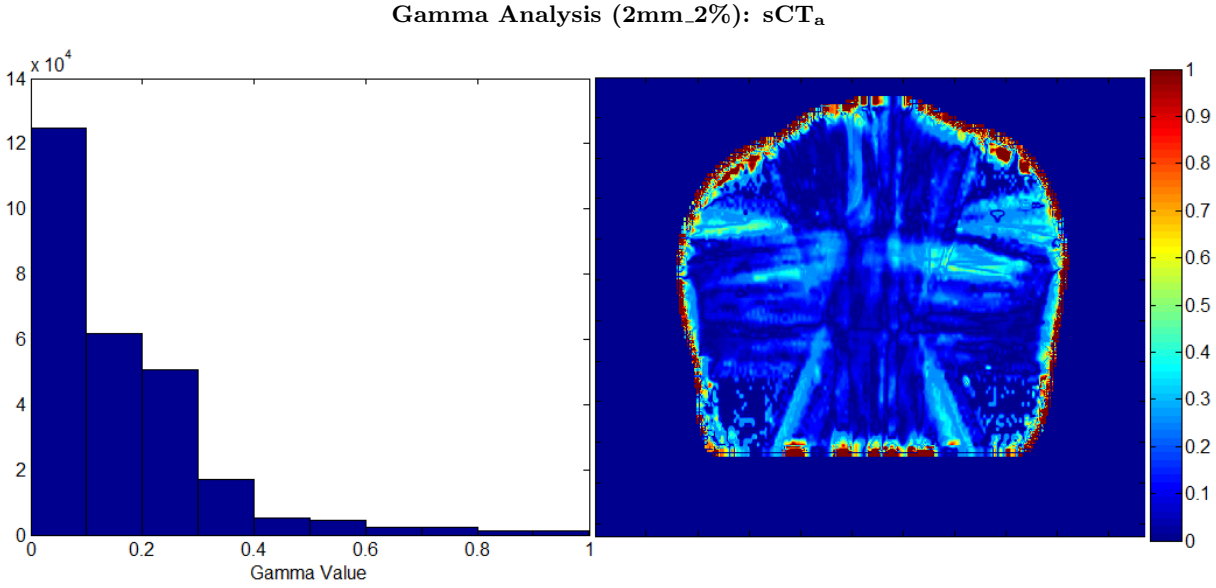

Figure 4.25: Gamma map performed for a combination of 2mm DTA and 2% DD for sCT_a (right) and respective gamma histogram (left) for one representative prostate patient.

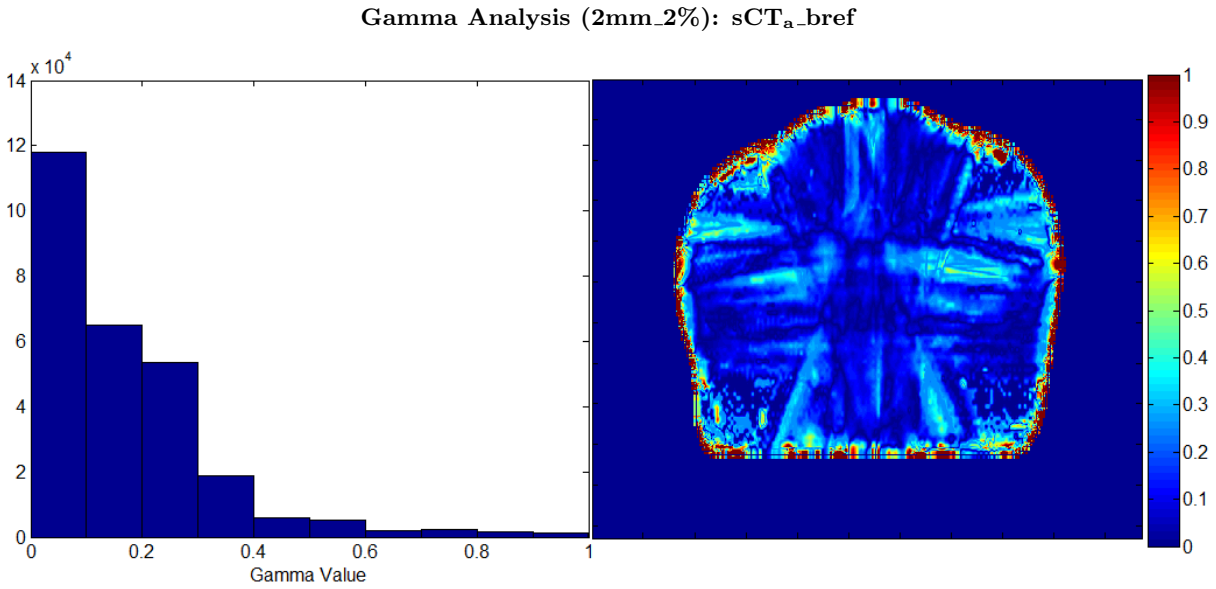

Figure 4.26: Gamma map performed for a combination of 2mm DTA and 2% DD for sCT_a_bref (right) and respective gamma histogram (left) for one representative prostate patient.

4.1.2.3 Dose Volume Histogram Analysis

As for the H&N patients, a DVH analysis plotting DVH bands enclosing results for 13 prostate patients for the PTV, the prostate and the OAR - bladder, rectum, RFem and LFem - was performed. In addition, a DVH point percentage difference for all contours is presented in this section. The DVH bands were plotted for 13 patients as 2 patients were left out due to a different prescribed dose (74 Gy instead of 67 Gy). For the DVH points percentage different analysis all 15 patients were analysed.

In Figure 4.27, one can see that the shape of the DVH bands derived using the original CT and each sCT for dose calculations are very similar for the majority of the contours. To have a more clear idea of the differences, magnified extracts of the PTV, the prostate and the bladder DVH bands can be seen in Figures 4.28 - 4.30.

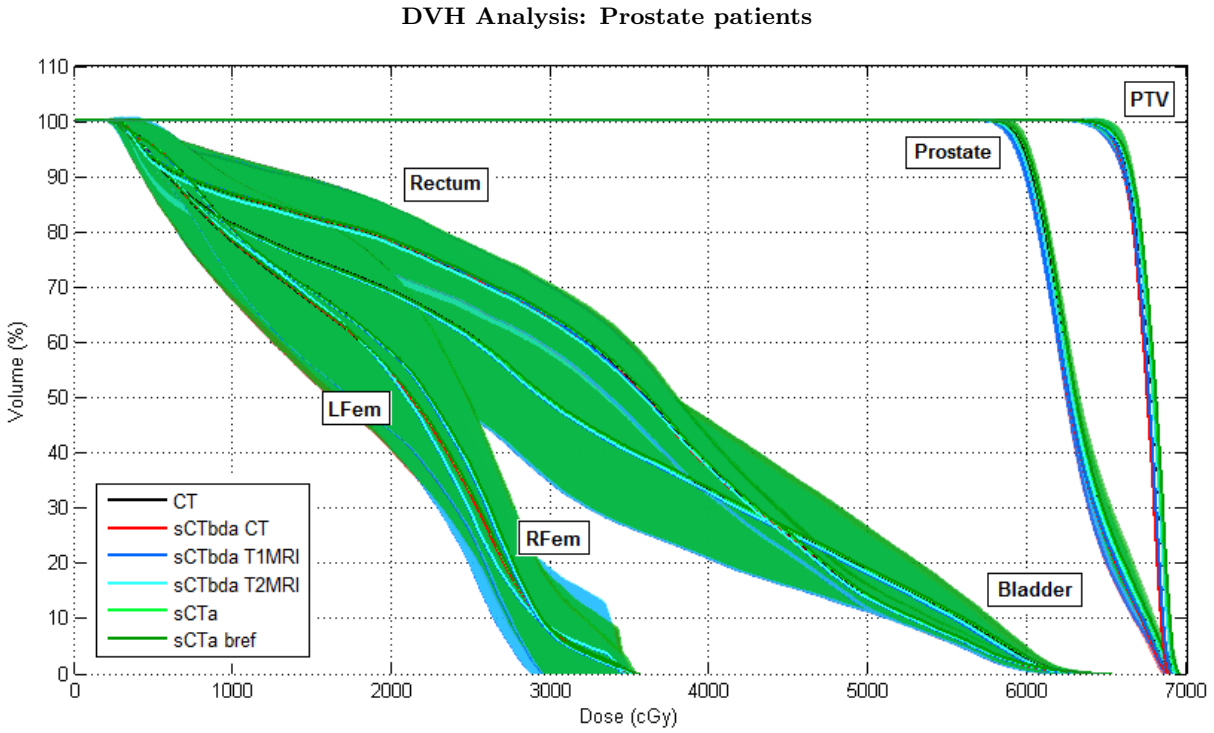

Figure 4.27: DVH bands for 13 prostate patients plotted for CT (black) and the remaining 5 sCT dose distributions: sCT_{bda}-CTinfo (red), sCT_{bda}-T1-MRinfo (blue), sCT_{bda}-T2-MRinfo (cyan), sCT_a (lime), sCT_a-bref (green). The bands were plotted for the following ROIs represented from left to right: LFem, RFem, Bladder, Rectum, Prostate and PTV.

In the zoom of the DVH bands for the PTV contour (Figure 4.28) it can be seen that the DVH bands for the majority of sCT methods do not overlay with the envelope for the original CT. The tight envelope for the original CT indicates few variations in the original dose distributions over all patients. When using sCT for treatment planning more variations in the dose distributions between the different patients are observed. For both sCT_a methods (in green) and CTinfo and T1-MRinfo sCT_{bda} (in red and blue respectively), the DVH envelopes do not match with the CT one (in black) indicating an overestimation of the dose given to the PTV for the first two and an underestimation for the remaining ones. For sCT_{bda}-T2-MRinfo, the best match with the envelope of the original dose distributions is seen. Despite all seen differences, the maximum deviation between the mean curve of the original CT and the mean curve of any sCT is only about 0.5 Gy, which is considered clinically insignificant for a prescribed dose of 67 Gy.

The zoom performed on the DVH bands for the prostate is represented in Figure 4.29. Similar results are obtained compared to the PTV contour. Both sCT_a methods showed a slight overestimation of the dose given to the prostate while for CTinfo and MRinfo sCT_{bda} an underestimation is displayed. As for the PTV contour, the observed differences are however clinically insignificant as deviations from the original CT mean curve are smaller than 0.5 Gy.

In Figure 4.30 for the bladder, despite the DVH bands appear to be overlaid for all CT and sCT methods, it's possible to see a clear similarity between CT mean curve with sCT_a and sCT_a-bref mean curves while for both CTinfo and MRinfo sCT_{bda} a slight mean underestimation is observed. Again, these differences are not clinically significant. A similar behaviour is seen for the remaining OAR.

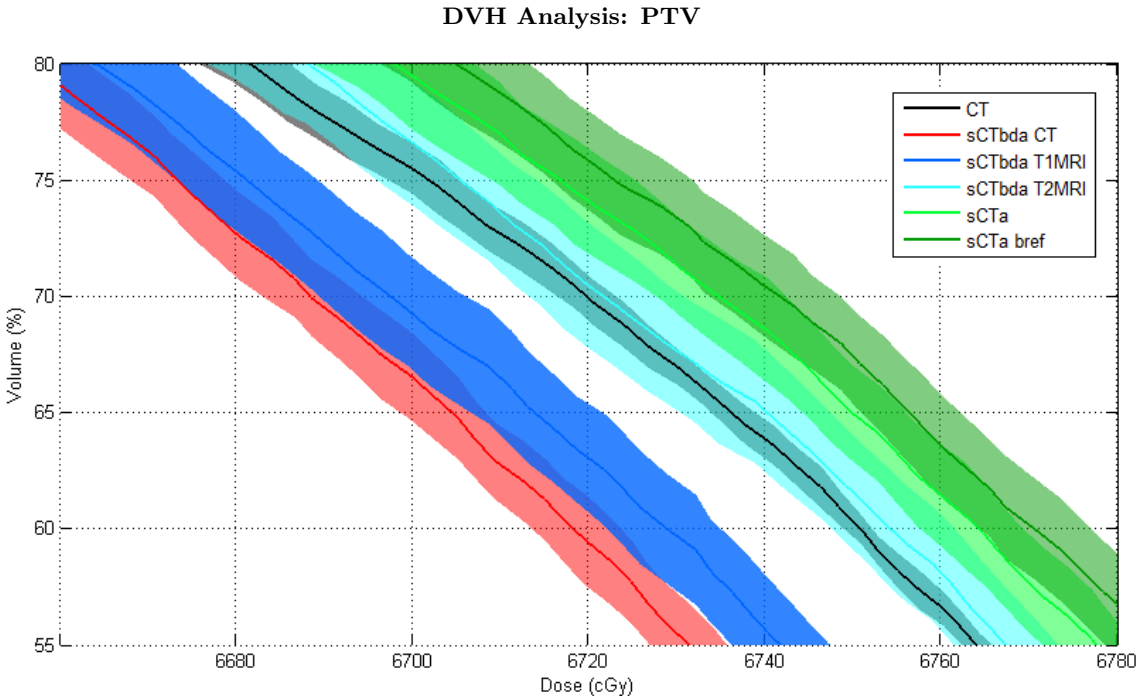

Figure 4.28: Performed zoom on the drop curve of the DVH for PTV ROI.

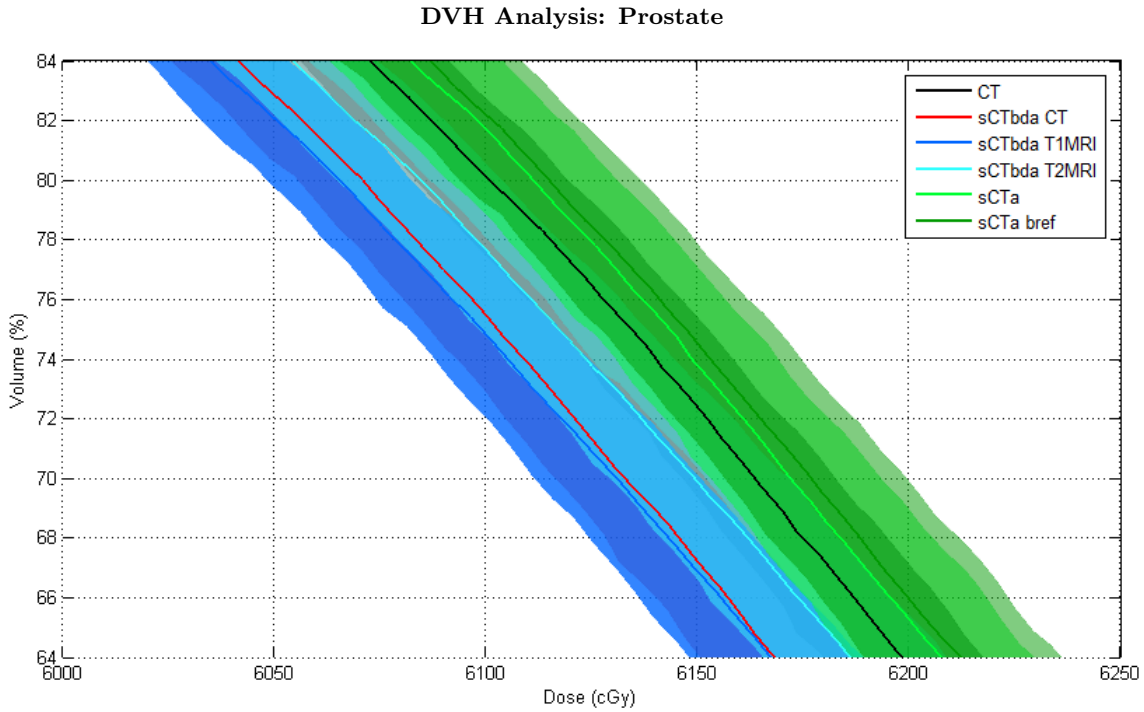

Figure 4.29: Performed zoom on the drop curve of the DVH for Prostate ROI.

The DVH points percentage differences were obtained for the DVH points stated previously in Table 3.1 in section 3.3.1 and the same uncertainty dose calculation criteria of 2% in a maximum for 95% of the patients, as mentioned before, was used for comparisons. As for the H&N patients, the absolute percentage differences will be discussed.

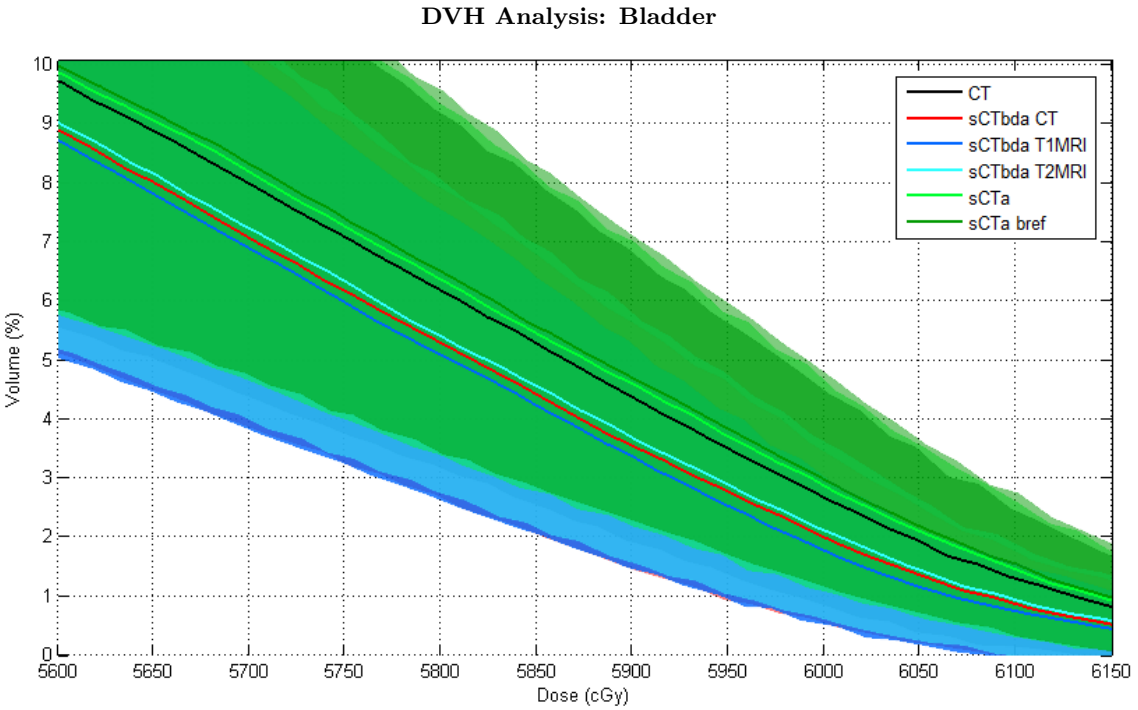

Figure 4.30: Performed zoom on the drop curve of the DVH for Bladder ROI.

For the PTV, it's difficult to see any trends looking at D98%, Dmean and D2% (Figures 4.31 - 4.33). The maximum percentage difference for all PTV DVH points is equal to about 2% and thus within the acceptable deviation for all methods.

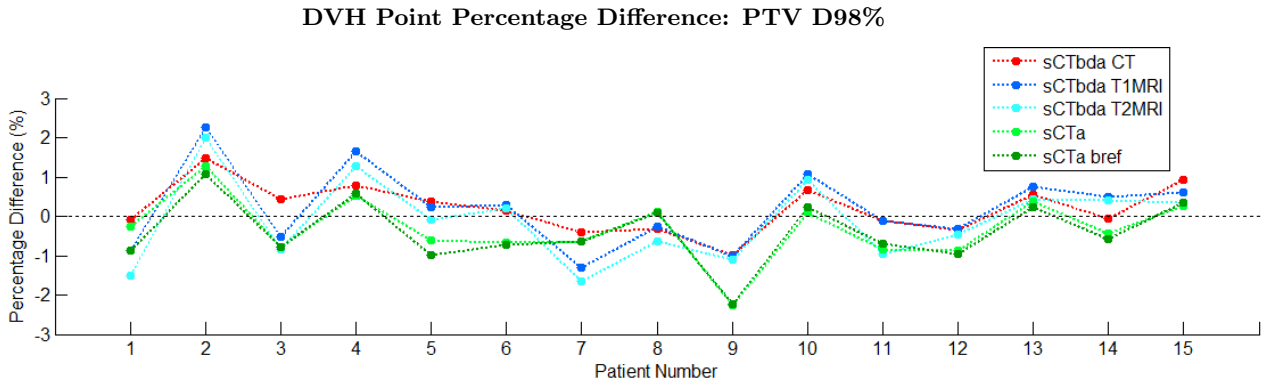

Figure 4.31: DVH point D98% percentage difference for PTV ROI for CT and sCT plans for all 15 prostate patients.

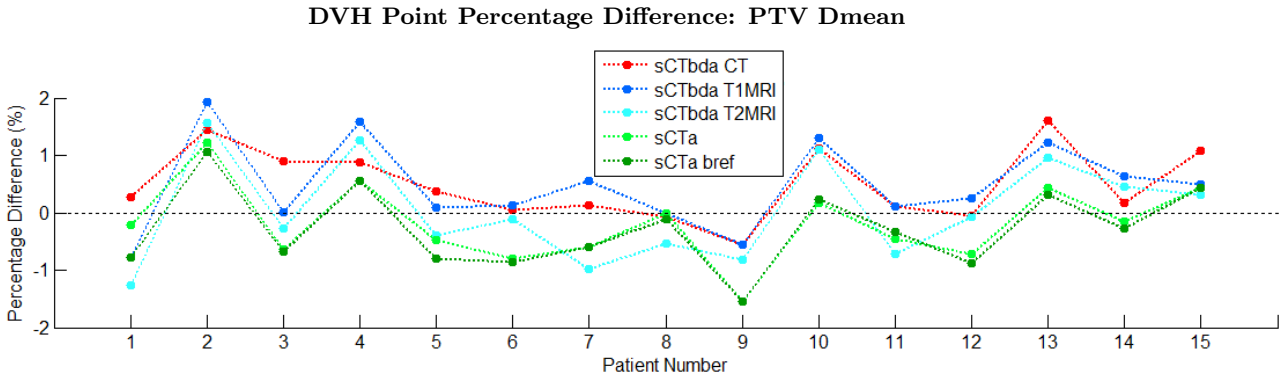

Figure 4.32: DVH point Dmean percentage difference for PTV ROI for CT and sCT plans for all 15 prostate patients.

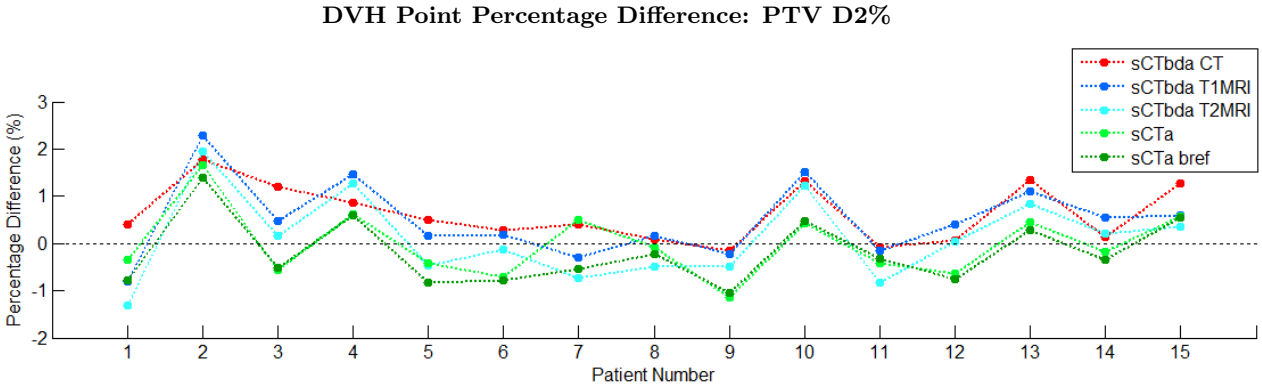

Figure 4.33: DVH point D2% percentage difference for PTV ROI for CT and sCT plans for all 15 prostate patients.

The results for the prostate and the OAR are shown in Figures 4.34 - 4.38 and similar conclusions can be derived. For the prostate, the rectum and the bladder (Figures 4.34, 4.35 and 4.36, respectively) the results are mainly within the 2% criteria. For the prostate and the rectum it's difficult to denote any trends when using different sCT. For the bladder it's possible to see a clear separation for the sCT_{bda} methods and sCT_{a} methods. For the majority of the patients, the sCT_{a} results are below the black line (which indicates a difference between sCT and CT dose distributions equal to 0) and the sCT_{bda} are above.

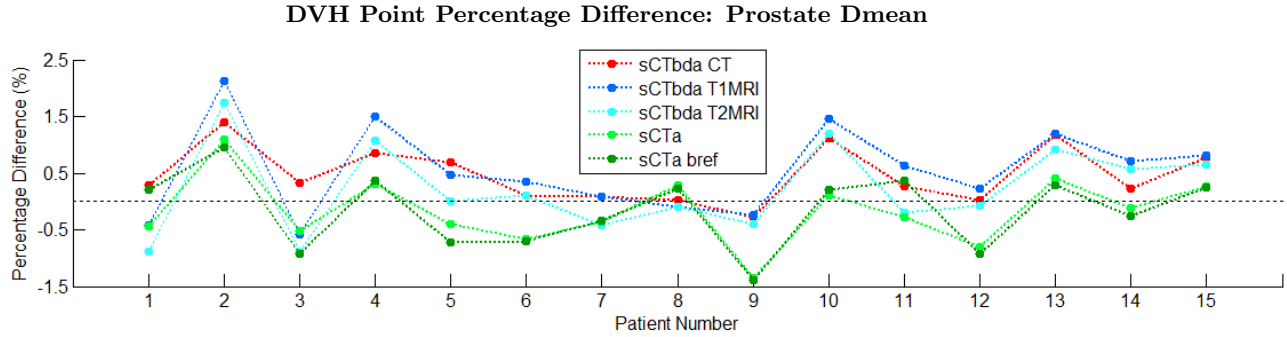

Figure 4.34: DVH point Dmean percentage difference for Prostate ROI for CT and sCT plans for all 15 prostate patients.

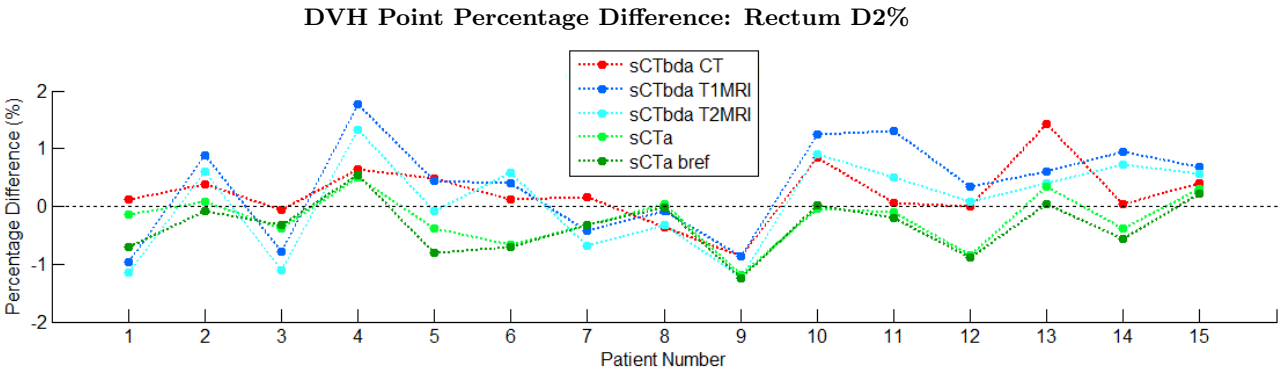

Figure 4.35: DVH point D2% percentage difference for Rectum ROI for CT and sCT plans for all 15 prostate patients.

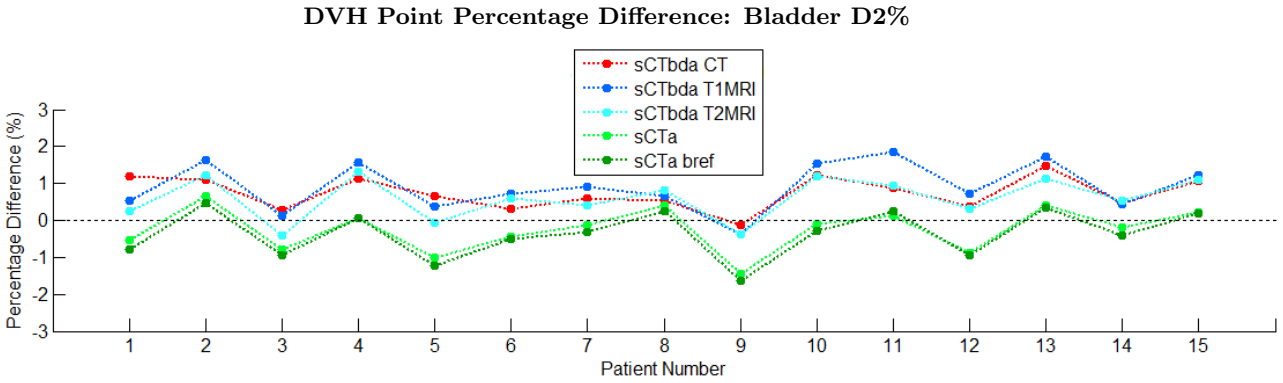

Figure 4.36: DVH point D2% percentage difference for Bladder ROI for CT and sCT plans for all 15 prostate patients.

Also for LFem and RFem (Figure 4.37 and 4.38) contours, no trend is visible. The maximum dose difference verified for the CT and sCT plan increases to about 3%. However, this maximal dose difference is only seen for a small number of patients and only for the sCT_{bda}-MRinfo method.

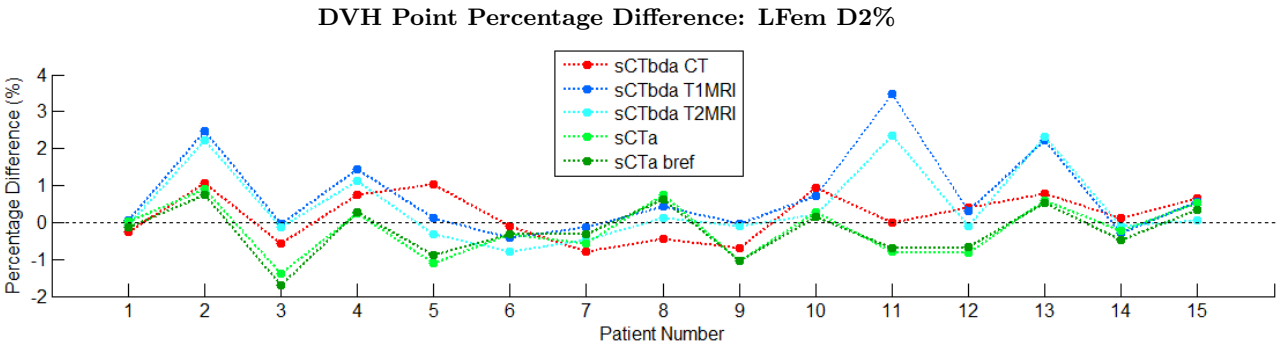

Figure 4.37: DVH Point D2% percentage difference for LFem ROI for CT and sCT plans for all 15 prostate patients.

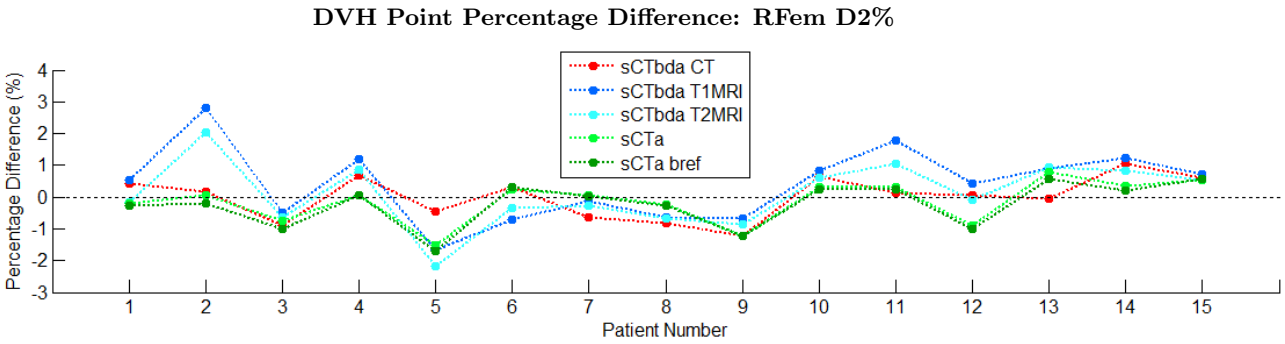

Figure 4.38: DVH point D2% percentage difference for RFem ROI for CT and sCT plans for all 15 prostate patients.

The results for the statistical analysis of the DVH points dose differences between CT and sCT dose distributions performed using the Kruskal-Wallis test are presented in Table 4.2. As for the H&N patients, the statistical test was applied to all calculated deviations between CT and sCT DVH points. The p-values obtained for each DVH point and for each contour are mostly greater than the significance level defined (0.01). For the bladder, a p-value equal to $3.067e^{-7}$ was obtained, indicating a significant difference between the 5 sCT methods when compared to the original CT dose distribution. This difference was already denoted in Figure 4.36 where a clear distinction between sCT_{bda} and sCT_{a} methods is seen. For the remaining DVH points, p-values greater than 0.01 were obtained and so no significant differences are found when using either sCT method for dose calculations compared to the clinical CT.

Table 4.2: Results for the Kruskal-Wallis statistical test conducted to deviations (including the signs stated by the difference) in DVH parameters by comparing the DVH points between CT and all used sCT dose distributions for all 15 prostate patients.

DVH Point Percentage Difference CT-sCT		
ROI	**DVH Point**	**p-value for the Kruskal-Wallis test**
PTV	D98%	0.212
	Dmean	0.013
	D2%	0.022
Prostate	Dmean	0.021
Bladder	D2%	$3.067e^{-7}$
Rectum	D2%	0.016
LFem	D2%	0.083
RFem	D2%	0.350

A further statistical analysis was performed and is shown in a form of box plots for PTV Dmean in Figure 4.39. The variation of the data is not equally distributed. A higher degree of variation can be seen for both sCT_{bda} while a low degree of variation is obtained for CT data. This variation is in agreement with the DVH bands results previously presented. A clear similarity between CT and sCT_{a} and sCT_{a}_bref medians is achieved. It's also possible to verify the underestimation seen before for CTinfo and T1-MRinfo sCT_{bda}. Despite these differences, the interquartile ranges do overlap each other between all considered plans and so no significant differences between them are found, confirming the p-value result obtained previously.

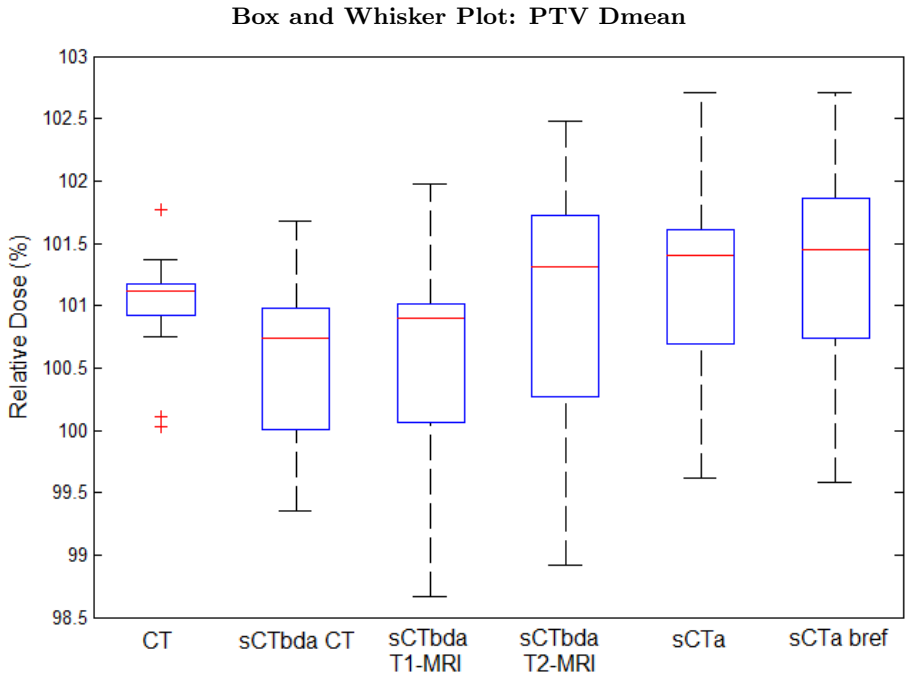

Figure 4.39: Box and Whisker plot for PTV Dmean DVH point for all 15 prostate patients.

4.1.3 Prostate Patient 16

4.1.3.1 Dose Difference Analysis

For the prosthetic hip patient, DD maps were obtained for a representative slice within the MRI FOV for sCT_{bda}-CTinfo, sCT_{bda}-T1-MRinfo and sCT_a. The maps are shown in Figure 4.40 in a dose scale of -3 to 3 Gy absolute dose difference. Results obtained for sCT_{bda}-T1-MRinfo / sCT_{bda}-T2-MRinfo and sCT_a / sCT_a-bref were similar, respectively and thus, the results for the two later are not shown here.

For sCT_{bda}-CTinfo, minimal differences on the inside of the patient ranging from -1 to 1 Gy can be seen. As this method used the original CT contours small variations were expected to occur.
For sCT_{bda}-T1-MRinfo large variations are seen. Differences between CT and sCT dose distributions are increased to 3 Gy and main differences are located on the right side of the scan where the implant was positioned. These differences are expected as the implant definition on MRI scans was done manually and only as a best guess for its real position. Due to the presence of the hip implant, artifacts in the MR images were observed which challenged the contouring even more.
For sCT_a, similar differences as for the sCT_{bda}-T1-MRinfo method are observed, however they are less pronounced. The occurrence of these differences is also expected as for sCT_a scans the Atlas method is not capable of reproducing the implant existence accurately (see section 3.2.1). As no patient with a prosthetic hip was included in the atlas, no similarity can be found when matching the patient's MRI with the MRIs in the atlas database. As a result, the algorithm is not capable of reproducing the existence of the implant.

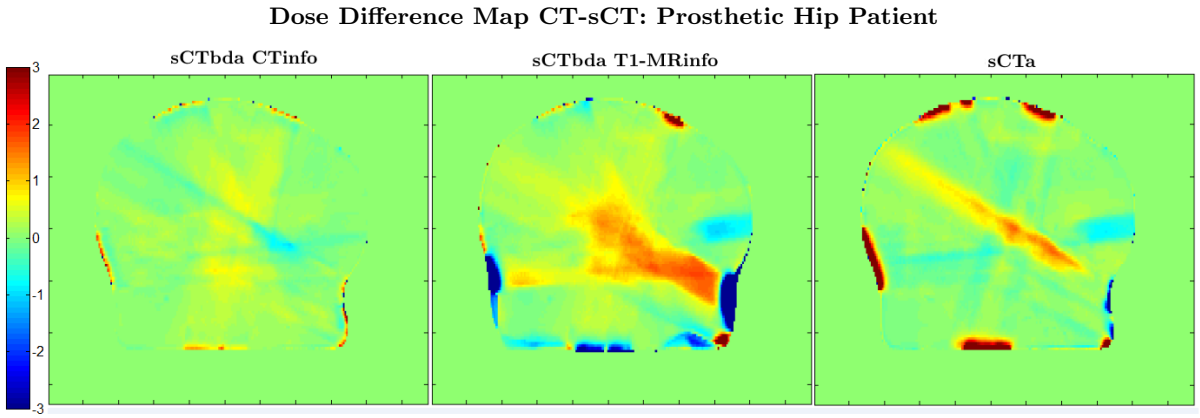

Figure 4.40: DD maps for CT – sCT_{bda}_CTinfo (left), CT- sCT_{bda}_T1-MRinfo (middle) and CT – sCT_a (right) for prostate patient 16 (scale in Gy).

4.1.3.2 Gamma Analysis

The gamma maps for sCT_{bda}_CTinfo, sCT_{bda}_T1-MRinfo and sCT_a are displayed in Figure 4.41. The 2mm_2% criteria was applied here.

For sCT_{bda}_CTinfo, it's possible to see that the majority of points (95.9%) passes the gamma test. Only some variances around the edges are observed due to the same reasons explained before (see section 4.1.2) and only a small quantity of points inside the patient fails the criteria. For sCT_{bda}_T1-MRinfo and sCT_a significant differences are seen. A high percentage of points fails the criteria not only on the edges of the patient but also on its inside. The percentage of points passing the criteria is reduced to 79.9% and 85.6% for sCT_{bda}_T1-MRinfo and sCT_a, respectively.

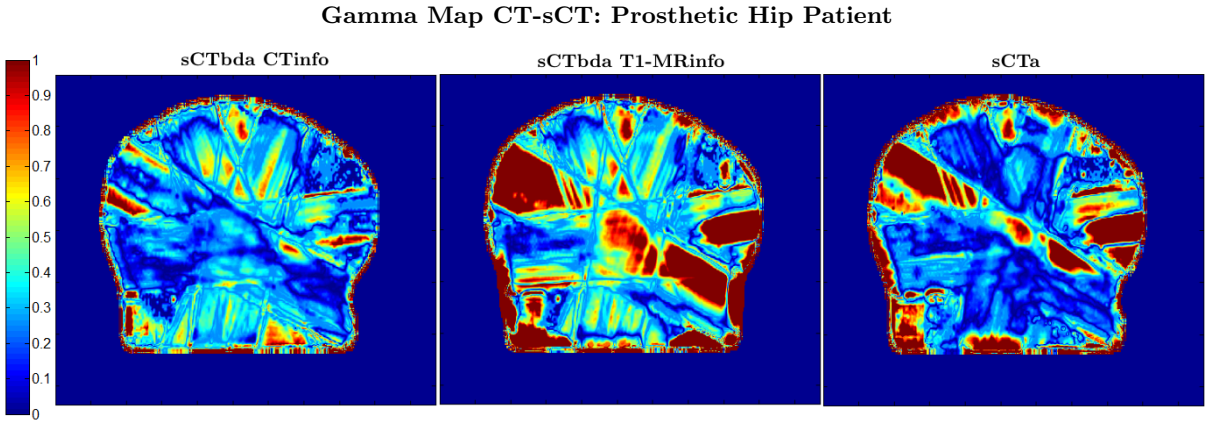

Figure 4.41: Gamma maps for CT – sCT_{bda}_CTinfo (left), CT- sCT_{bda}_T1-MRinfo (middle) and CT – sCT_a (right) for prostate patient 16.

4.2 Geometric Results

A geometric evaluation was carried out, comparing the geometrical accuracy of a delineation performed based on the clinical CT and based on the MRI and sCT_a scans. Delineation is of key importance for RTP. The tumour, OAR and other tissues have to be delineated with high precision especially for the sCT_{bda} approach, where electron densities are assigned accordingly. The results of this part of the study are divided in 3 parts for the H&N patients as well as for the prostate patients:

C.1 Individual evaluation of shape and position changes;

C.2 Individual evaluation of volume changes;

C.3 Overall evaluation of volume, shape, position and orientation changes.

4.2.1 Head and Neck Patients

4.2.1.1 Individual evaluation of shape and position changes

In Figures 4.42 and 4.44 - 4.46 overlays of external, bone, LParotid and SpinalCord contours are displayed. The contours delineated on both MRI scans (green for T1-MRI and red for T2-MRI) and sCT_a (blue) are compared to the clinically approved CT contours (black). For bone contours based on the sCT_a, results before and after performing bone refinement are shown in blue and dark yellow, respectively. Contours for one representative patient in the same slice for all methods are presented.

In Figure 4.42, a great similarity of the external contours defined in all scans can be seen. However, looking at T1-MRI and T2-MRI external contours it can be seen that the contours based on the original CT image are always a few voxels larger than the contours based on the MR images.

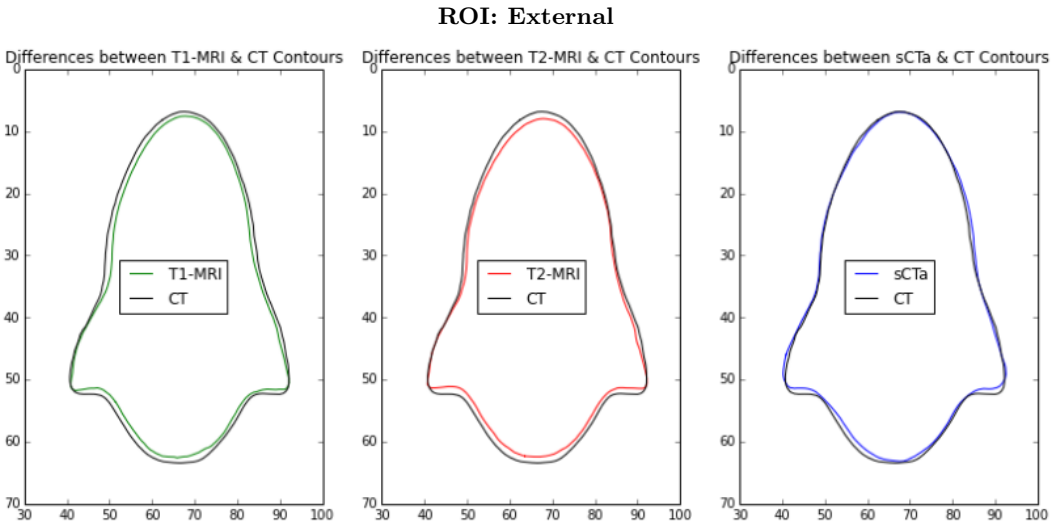

Figure 4.42: External contour delineation performed on CT (in black) against T1-MRI (left), T2-MRI (middle) and sCT_a (right) based delineations in green, red and blue respectively for one representative H&N patient.

Possible explanations might be:

1. CT images are often sharper than MR images as they are acquired quicker;
2. The resolution of MR images rarely matches the voxel size and while it's relatively easy to reduce the voxel size, this won't necessarily translate into a higher resolution;
3. For MR images, at the skin the water signals dominate while under the skin, more precisely in the subcutaneous layer, the fat signals does. Thus, when these signals are out of phase they will cancel each other making water-fat boundaries have a very low MR signal.

As a result of the above mentioned points, the MR images usually don't express clear boundaries at the patient's surface. A zoom of the boundary in a MRI scan and a CT scan is shown in Figure 4.43. A two step drop of intensity over a few voxels can be noticed in the MR image until the intensity of air outside the patient is reached. When zooming in the boundary in the CT scan a clearer drop of intensities is seen. These differences are responsible for creating different externals for all 6 H&N patients. For future studies, an important question to answer is which voxels in the MR images belong to the patient and which not. This is important to omit further interference with the registration process between images.

Defining the external based on the sCT_a scans might be a solution, as high similarities with the original CT contours are observed (example Figure 4.42 right).

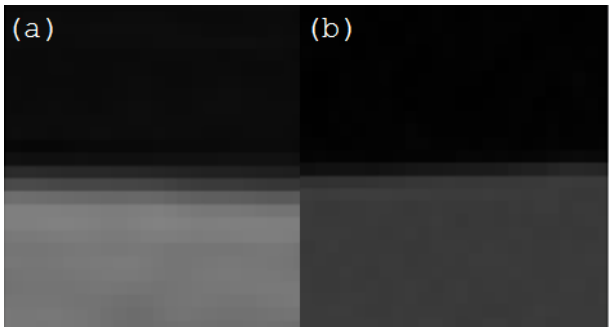

Figure 4.43: Performed zoom on MR (a) and CT (b) images on the patient's boundary.

In Figure 4.44 one can see the bone contours for all scans in a representative slice. Obvious deviations in shape are observed between the original bone contours and the contours based on the MRI, both T1 and T2 weighted. This is a result of the inter-observer variability as the contours were manually defined on the MRI scans. When looking at the contours defined on the sCT_a scans, a higher degree of shape similarity is achieved. After performing a bone refinement process, improvements can be obtained as the contours appear to be more shapely defined around the edges.

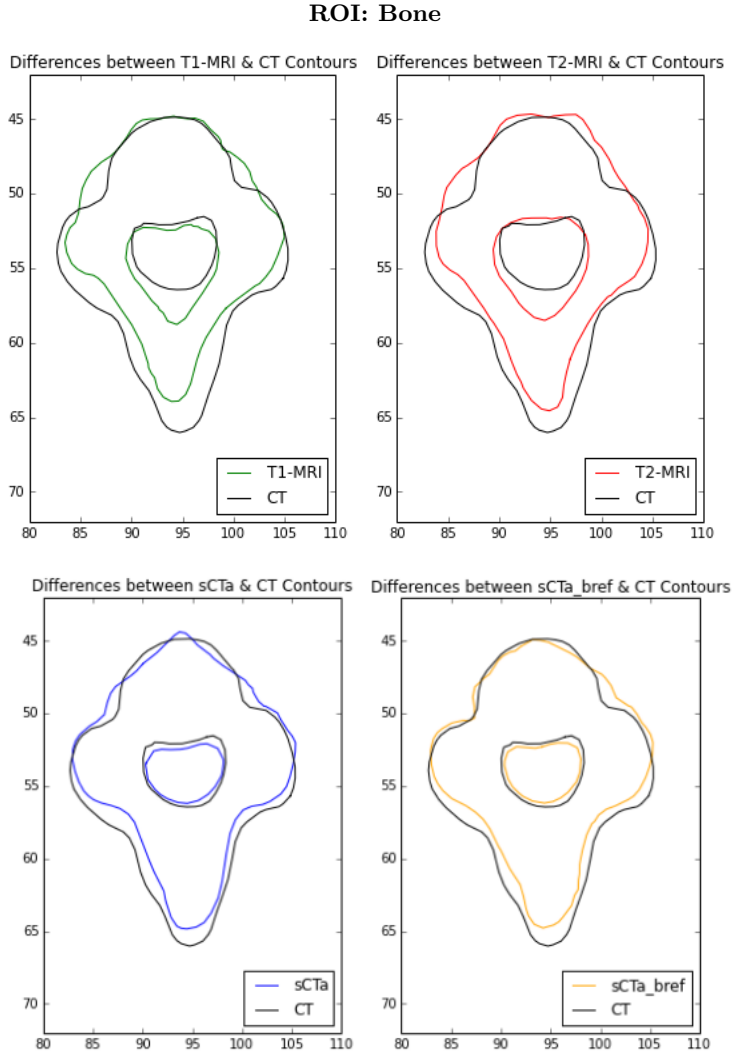

Figure 4.44: Bone contour delineation performed on CT (in black) against T1-MRI (top left) and T2-MRI (top right), sCT_a (bottom left) and sCT_a_bref (bottom righ) based delineations in green, red, blue and dark yellow, respectively for one representative H&N patient.

The results for the OAR contours are shown in Figures 4.45 and 4.46 for the LParotid and the SpinalCord contours, respectively. The results obtained for RParotid were similar to the ones obtained for LParotid.

Similarities of all contours can be seen, however for all scans there exist noticeable deviations in shape and in size. The Lparotid contour based on the sCT_a appear to be smaller than the parotid based on MR images. The SpinalCord contour based on the sCT_a on the other hand seem to be bigger than the SpinalCord contours based on the MRI scans. The later are also significantly smaller than the original SpinalCord contour. Differences between CT and MRI delineation of the spinal cord could be explained by the fact that the spinal cord is a serial organ and often an extra protection margin is considered in CT delineations, where soft tissue contrast is not optimal. In MR images, with a higher soft tissue contrast, a more precise delineation can be performed. In general, a better reproducibility of the contours can be observed when basing them on sCT_a scans than when based on MRI scans.

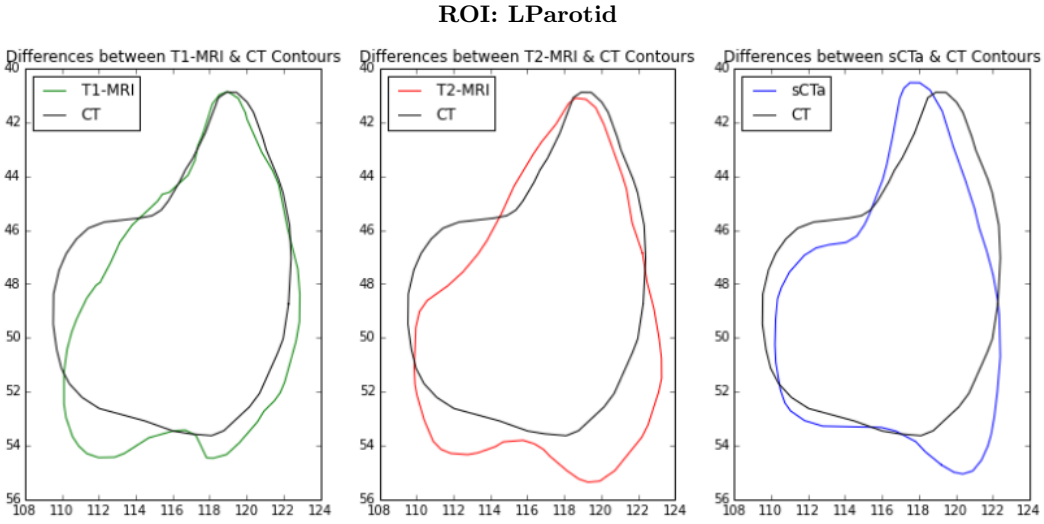

Figure 4.45: LParotid contour delineation performed on CT (in black) against T1-MRI (left), T2-MRI (middle) and sCT_a (right) based delineations in green, red and blue respectively for one representative H&N patient.

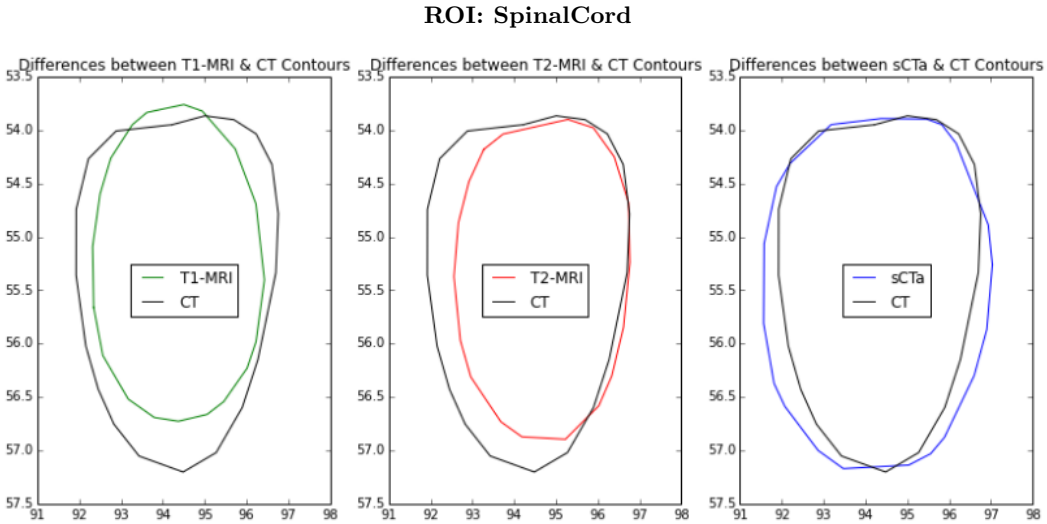

Figure 4.46: SpinalCord contour delineation performed on CT (in black) against T1-MRI (left), T2-MRI (middle) and sCT_a (right) based delineations in green, red and blue respectively for one representative H&N patient.

4.2.1.2 Individual evaluation of volume changes

To evaluate changes in volume when performing CT, MRI and sCT_a based delineations, for the external and bone contours VI results are plotted for each patient in Figures 4.47 and 4.48, respectively. For the OAR contours, the absolute volume for the LParotid and the SpinalCord in each scan - CT, T1-MRI, T2-MRI and sCT_a - are plotted for each patient in Figures 4.49 and 4.50. RParotid results were similar to LParotid results.

For the external contours, the obtained VI values are similar for all scans and lie between 1.0 and 1.07. As stated before, a VI equal to 1 denotes an equal volume for the evaluated contours. Thus, VI values greater than 1 indicate that the volume of the original clinical external contour is set higher when compared to the MRI and sCT_a contours. Accordingly to the obtained VI values, a volume underestimation is achieved for both MRI and sCT_a based delineations. This

situation might be explained by the lack of coverage in the MR images mentioned before. The result for the Kruskal-Wallis test showed a p-value equal to 0.170 and so the null hypothesis is not rejected which means that VI values have equal medians for both sCT_a and MRI scans. Despite the p-value result indicates that no significant differences are found between MRI and sCT_a based delineations, it's possible to see in Figure 4.47 that the contours delineated on sCT_a have a slight closer agreement with the original ones for all 6 patients. These differences could be explained by the fact that MR images usually don't express clear boundaries as mentioned before (see section 4.2.1.1).

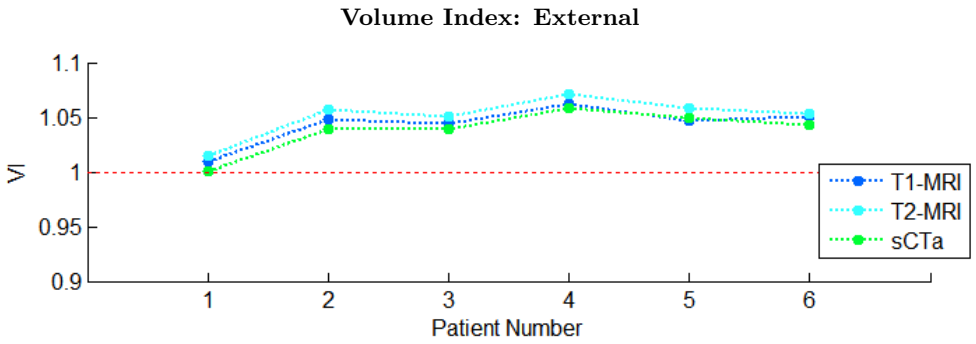

Figure 4.47: Volume Index (VI) results calculated for External ROI for all 6 H&N patients.

For bone contours, the following VI values were obtained: [1.04;1.17] for CT-MRI, [0.81;0.97] for CT-sCT_a and [0.90;1.03] for CT-sCT_a_bref. Accordingly to these values shown in Figure 4.48, two major conclusions can be drawn: First, bone volume delineated on both MRI scans is always smaller than the volumes based on CT. This was expected as the delineation was performed manually and thus some inaccuracies in bone delineation might have occurred. Second, bone volume defined on the sCT_a is always bigger than the original volume. This might be explained by the blurriness of the sCT_a scans which causes a spread in bone voxel. This situation can be improved when performing a bone refinement. These results are consistent with the results for the Kruskal-Wallis test as the p-value obtained is equal to 0.0004 which means that significant differences in volumes are found when delineating bone in MRI and sCT_a scans comparing to CT delineations. In Figure 4.48, one can see a clear trend when using MRI and sCT_a based contours: VI calculated for MRI contours are always above the red line (which indicates a perfect volume match) and VI calculated for sCT_a contours are always bellow the same.

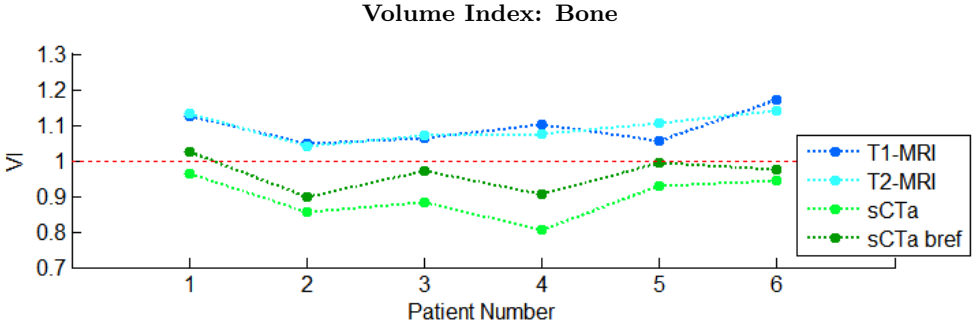

Figure 4.48: Volume Index (VI) results calculated for Bone ROI for all 6 H&N patients.

For the OAR it's difficult to see trends in Figures 4.49 and 4.50. Differences arise due to the different soft tissue contrast offered by MRI and sCT_a scans as explained in the previous section.

For all SpinalCord, RParotid and LParotid contours, the differences in volumes reached a maximum of 4 cm^3, 8 cm^3 and of 9 cm^3, respectively, for both MRI and sCT_a scans. A significant difference for the delineated contours can be seen as the parotids as well as the spinal cord are very small structures.

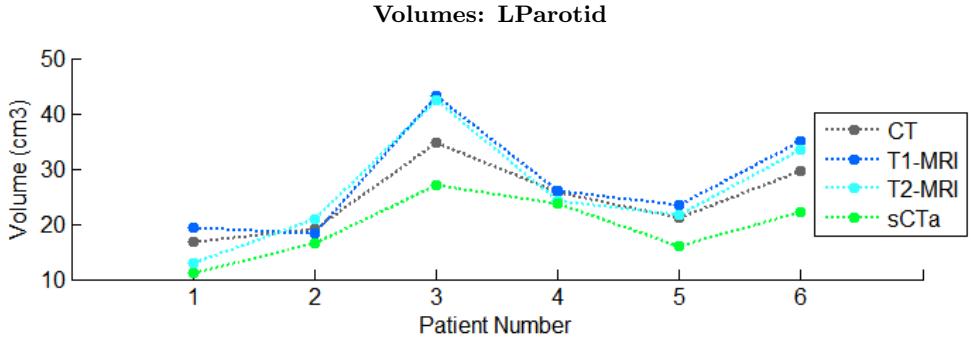

Figure 4.49: Volume changes in cm^3 for CT - (grey), T1-MRI (blue), T2-MRI (cyan) and sCT_a (green) based delineations calculated for LParotid ROI for all 6 H&N patients.

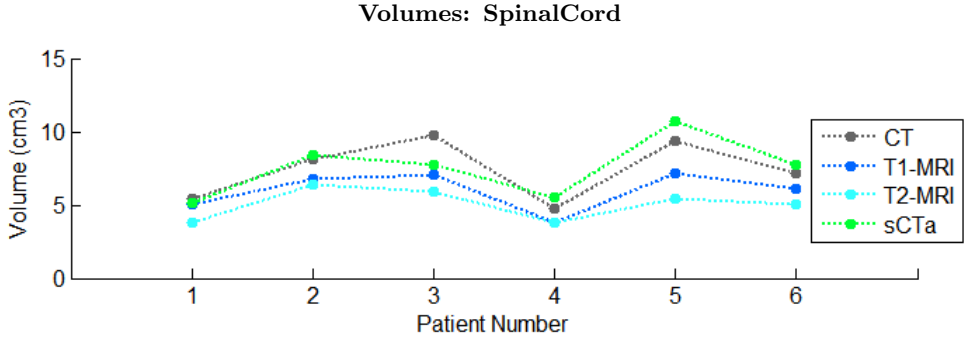

Figure 4.50: Volume changes in cm^3 for CT - (grey), T1-MRI (blue), T2-MRI (cyan) and sCT_a (green) based delineations calculated for SpinalCord ROI for all 6 H&N patients.

4.2.1.3 Overall evaluation of volume, shape, position and orientation changes

To generally evaluate the difference in contours, the DSC was calculated for every patient and for all the contours. The DSC values obtained for bone are shown in Figure 4.51 to illustrate the existence of trends. DSC value for each patient comparing contours on T1-MRI (blue), T2-MRI (cyan), sCT_a (green) and sCT_a_bref (dark green) are shown. DSC values closer to 1 indicate a high degree of similarity in volume, shape, position and orientation regarding to the CT contours (see section 3.3.2).

For the external contours, the DSC values are within the following interval [0.92;0.97] for all combinations made - CT-MRI and CT-sCT_a. No clear differences between the results obtained for different patients and for different methods are seen. As all values are greater than 0.7 in general, a good similarity with CT contours can be concluded. The result for the Kruskal-Wallis test showed a p-value equal to 0.895 and thus no significant differences in the median DSC values are found. Despite indicating that is feasible to perform external delineations using both MRI and sCT_a scans, clear deviations were observed previously in shape and in volume with more similarity between sCT_a and CT based delineations. Correcting the lack of coverage and improving the boundary definition on MRI scans might enhance the definition of the patient outline using sCTs.

For bone contours, the DSC values are comprised between 0.7 and 0.9 for all scans showing a good overall similarity with the original clinical contours. The p-value obtained for the Kruskal-Wallis test is equal to 0.065. Despite no significant differences are found in the statistical analysis for DSC values, a clear trend can be seen in Figure 4.51. High DSC values are obtained for sCT_a scans, clearly separating sCT_a and MRI results. The greater similarity between CT based and sCT_a based delineations is however in agreement with previous results. In Figure 4.51, a clear improvement on bone delineation when performing bone refinement on sCT_a is seen for the majority of the H&N patients.

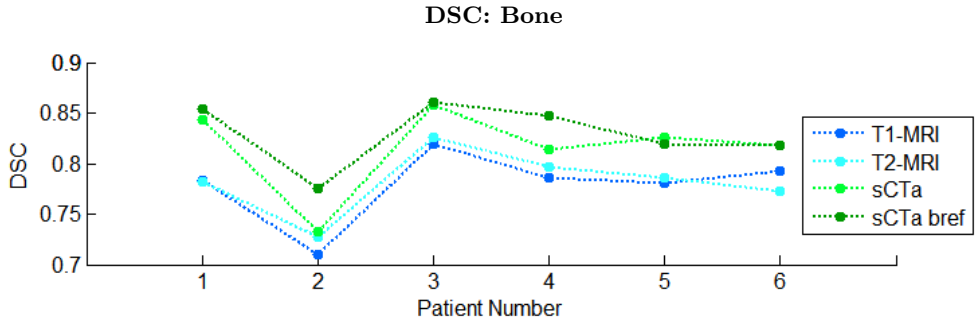

Figure 4.51: DSC values calculated for CT contours comparison with T1-MRI (blue), T2-MRI (cyan), sCT_a (green) and sCT_a_bref (dark green) contours for Bone ROI for all 6 H&N patients.

For the Lparotid contours, the DSC values achieved are equal to [0.68;0.87] for CT-MRI and [0.69;0.82] for CT-sCT_a. Similar results were obtained for RParotid. For the SpinalCord contours, the DSC values are within the following intervals for CT-MRI and CT-sCT_a respectively: [0.59;0.78] and [0.67;0.83]. The p-values obtained from the Kruskal-Wallis test are equal to 0.281 for Lparotid, 0.060 for Rparotid and 0.150 for SpinalCord which shows that no significant differences are found between delineations performed on MRI and on sCT_a. However, a greater dissimilarity with the original contours for OAR delineation is achieved. Differences between clinical delineations and MRI and sCT_a based delineations were already discussed in the previous sections. Despite sCT_a contours were proven to be more similar to CT contours, soft tissue delineations is generally believed to be accurately performed when using MRI scans.

4.2.2 Prostate Patients

4.2.2.1 Individual evaluation of shape and position changes

In Figures 4.52 - 4.57 overlays of external, bone, LFem, bladder, prostate, and rectum contours are displayed, respectively. Results for RFem were similar to LFem. Contours for one significant patient in the same slice for all methods are shown using the same selection of colours as before (see section 4.2.1.1).

In Figure 4.52, one can see shape deviations on the external contours defined on the MRI scans especially on the posterior side of the patient. Differences can be explained by the use of different couches during MR and CT imaging sessions. As a result, a systematic error is introduced. For the contours defined on the sCT_a scans almost a perfect match is obtained.

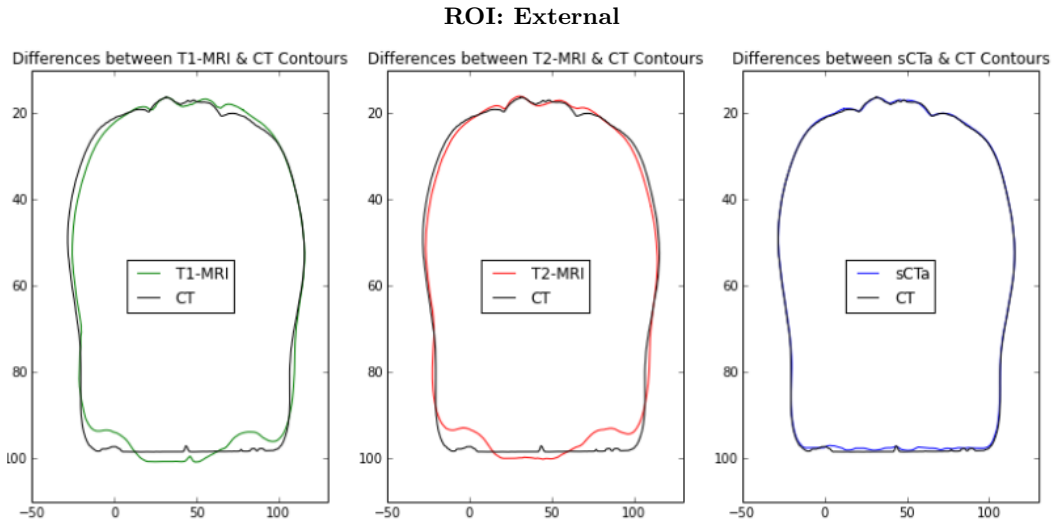

Figure 4.52: External contour delineation performed on CT (in black) against T1-MRI (left), T2-MRI (middle) and sCT_a (right) based delineations in green, red and blue respectively for one representative prostate patient.

In Figure 4.53 for bone contours the same conclusions stated before in section 4.2.1.1 can be retrieved. Significant deviations are seen for MRI contours, especially on the size of the delineated contours. These differences are considerably reduced when using the contours delineated on sCT_a scans, which could be further improved using sCT_a_bref. The differences between MRI and sCT_a based contours arise due to the manual and automatic delineation, respectively.

In Figure 4.54 for the LFem contours, slight deviations in size and position between MRI based and clinical contours can be seen. For sCT_a contours, these differences are clearly diminished and the contours are very similarly to the clinical ones. This greater similarity is expected as these ROIs are bone based contours and thus clearly seen when using CT based scans.

For the prostate (Figure 4.55), the bladder (Figure 4.56) and the rectum (Figure 4.57) contours large deviations can be seen for both MRI contours and sCT_a contours. Accordingly to Figures 4.55 - 4.57, two major conclusions can be drawn: First, MRI contours are usually smaller than the clinical approved CT contours. Second, contours delineated on sCT_a have equal or even a larger size than the original clinical contours. Similarly to the H&N patients, differences between CT and MRI delineations of OAR could be explained by the optimal soft tissue contrast offered by MRI and not by CT scans. Differences between CT and sCT_a delineations might be explained by the sCT_a image blurriness.

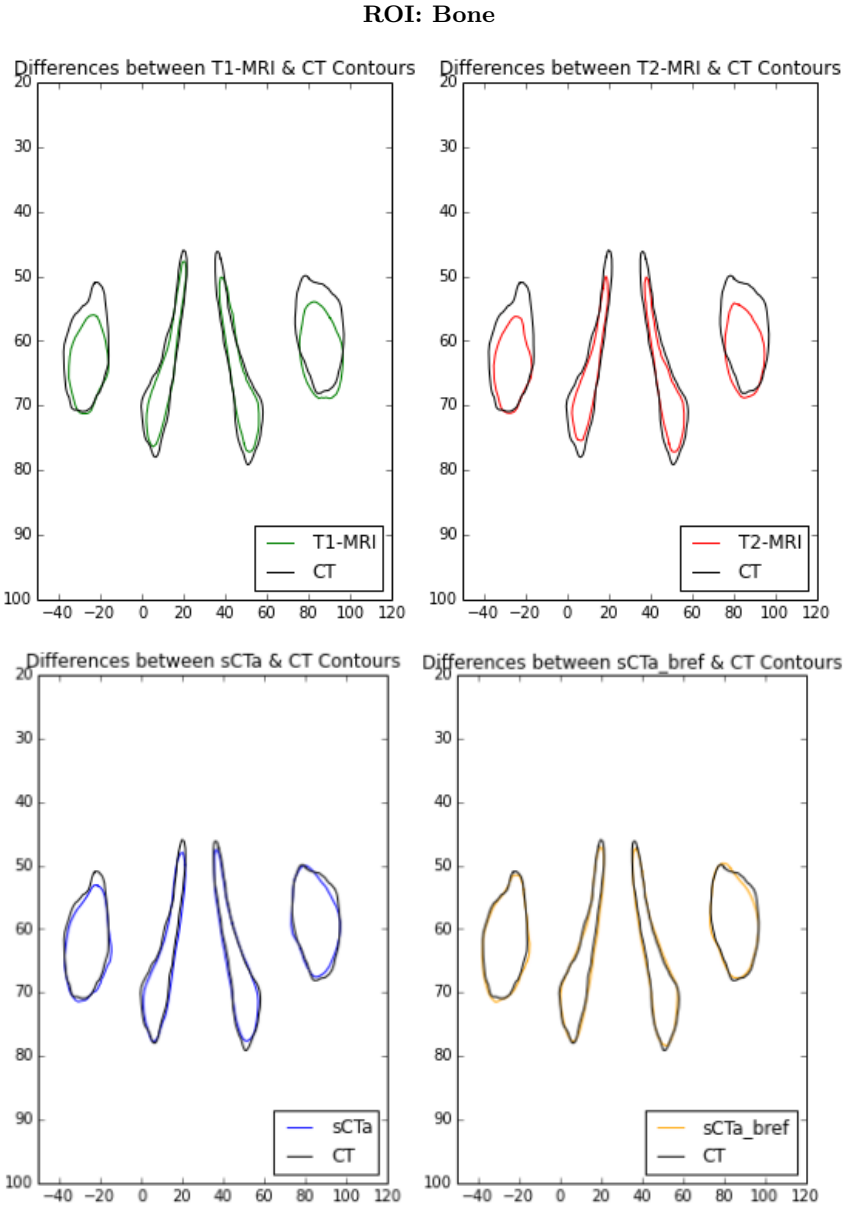

Figure 4.53: Bone contour delineation performed on CT (in black) against T1-MRI (top left) and T2-MRI (top right), sCT_a (bottom left) and sCT_a_bref (bottom righ) based delineations in green, red, blue and dark yellow, respectively for one representative prostate patient.

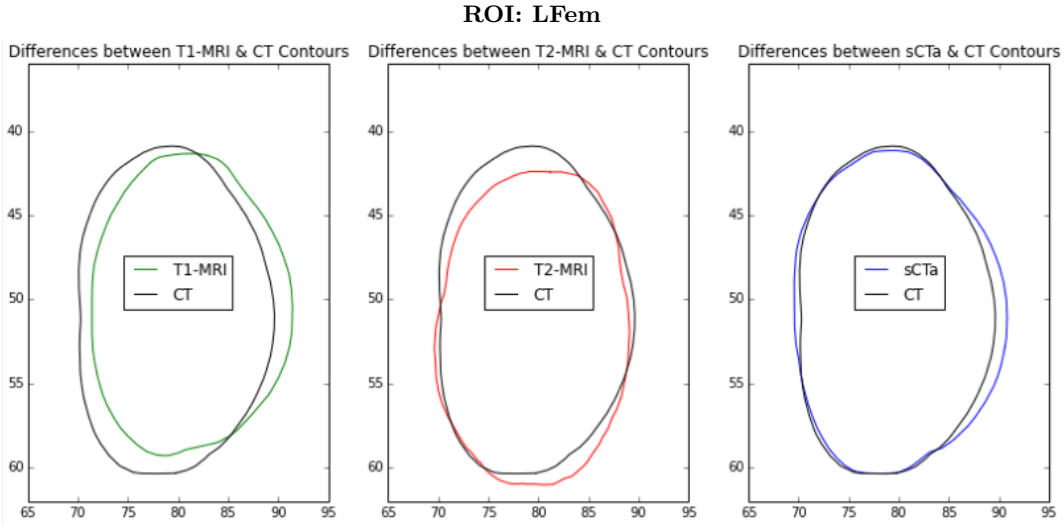

Figure 4.54: LFem contour delineation performed on CT (in black) against T1-MRI (left), T2-MRI (middle) and sCT_a (right) based delineations in green, red and blue respectively for one representative prostate patient.

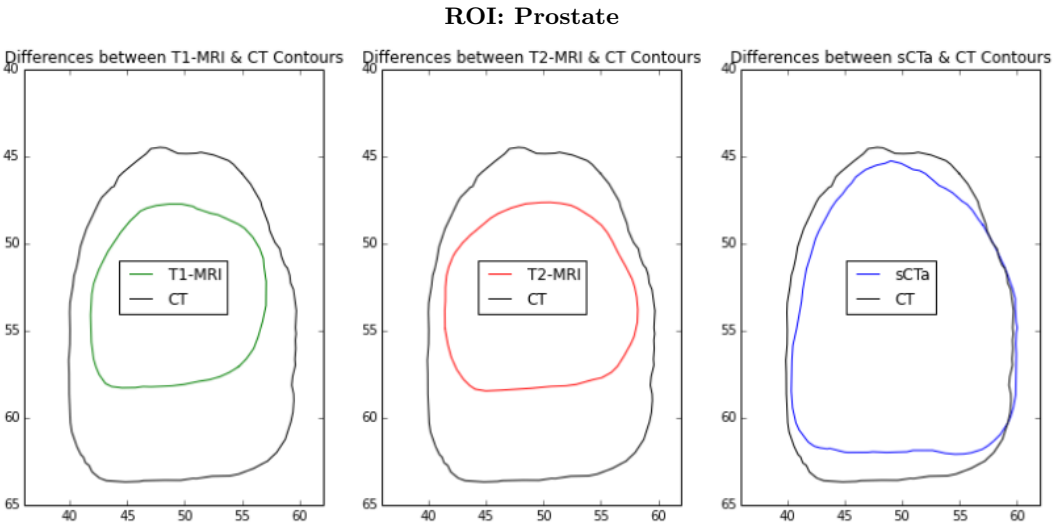

Figure 4.55: Prostate contour delineation performed on CT (in black) against T1-MRI (left), T2-MRI (middle) and sCT_a (right) based delineations in green, red and blue respectively for one representative prostate patient.

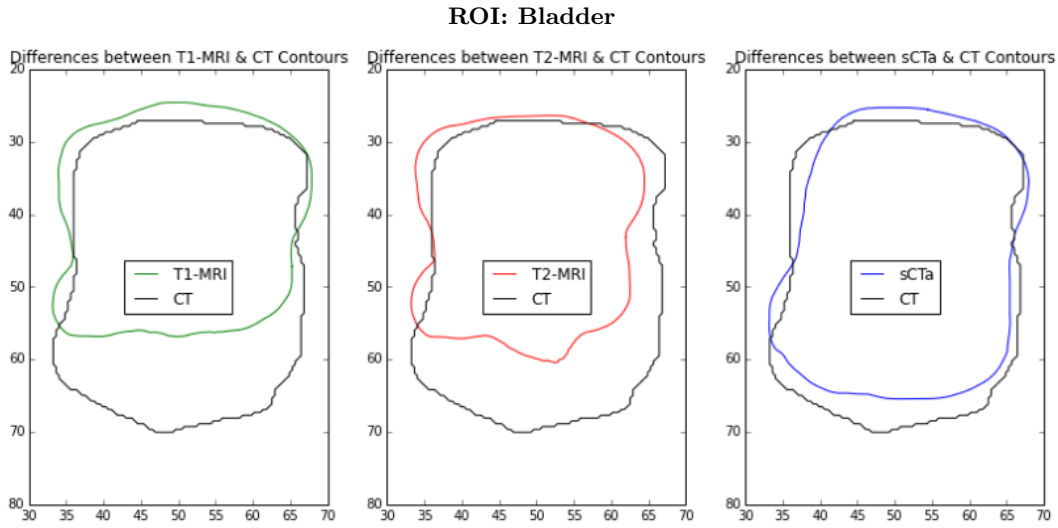

Figure 4.56: Bladder contour delineation performed on CT (in black) against T1-MRI (left), T2-MRI (middle) and sCT_a (right) based delineations in green, red and blue respectively for one representative prostate patient.

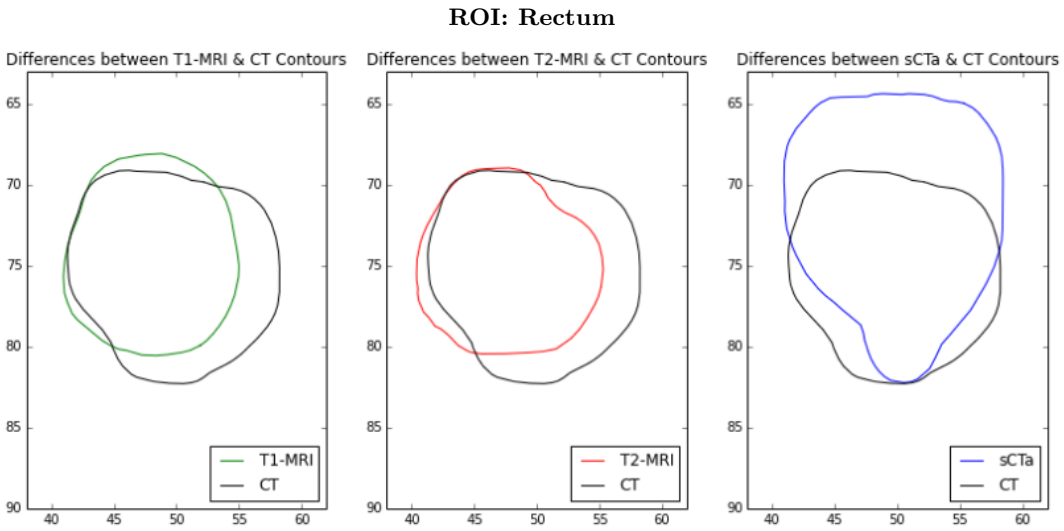

Figure 4.57: Rectum contour delineation performed on CT (in black) against T1-MRI (left), T2-MRI (middle) and sCT_a (right) based delineations in green, red and blue respectively for one representative prostate patient.

4.2.2.2 Individual evaluation of volume changes

As for the H&N patients, VI are plotted for the external and bone contours in Figures 4.58 and 4.59, respectively and for the LFem, the rectum and the prostate, absolute volumes for all patients and all scans are plotted in Figures 4.60 - 4.62, respectively.

In Figure 4.58 for the external contours one can see a clear trend between all scans. For all 15 patients a clear similarity between sCT_a based and CT based delineations is shown. VI values lie within [1.00;1.04] and [1.04;1.12] for CT-sCT_a and CT-MRI comparisons, respectively. The verified reduction in volume is due to the different couches used during MR and CT imaging sessions, as explained before. These significant volume differences are in agreement with the result for the Kruskal-Wallis test (p-value=$1.225e^{-13}$).

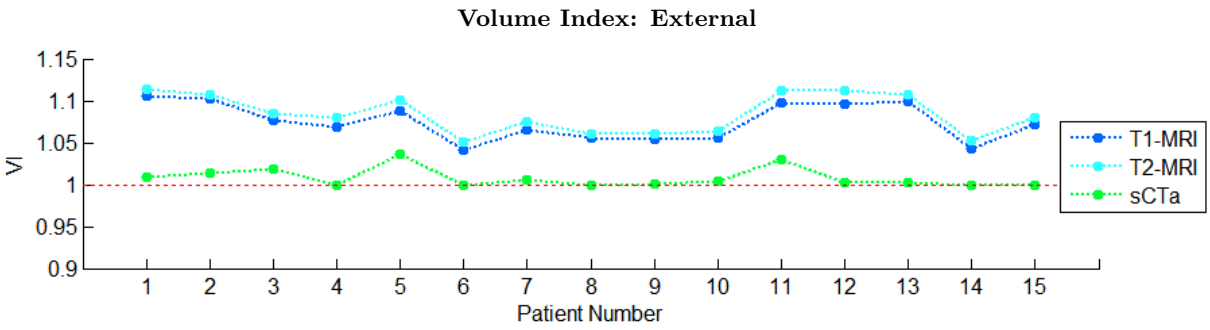

Figure 4.58: Volume Index (VI) results calculated for External ROI for all 15 prostate patients.

Also, for bone contours a clear trend is denoted in Figure 4.59. For the majority of patients, bone contours defined on sCT_a scans show a greater similarity with the clinical contour as VI values are closer to one (red line). An improvement in the results is achieved when using a bone refinement. VI values lie within [0.94;1.19] for CT-MRI comparison and within [0.94;1.04] for CT-sCT_a comparison. The result for the Kruskal-Wallis test shows a p-value equal to $6.288e^{-8}$. Significant bone volume differences are found between MRI and sCT_a delineations as expected. These differences were already explained in section 4.2.1.2.

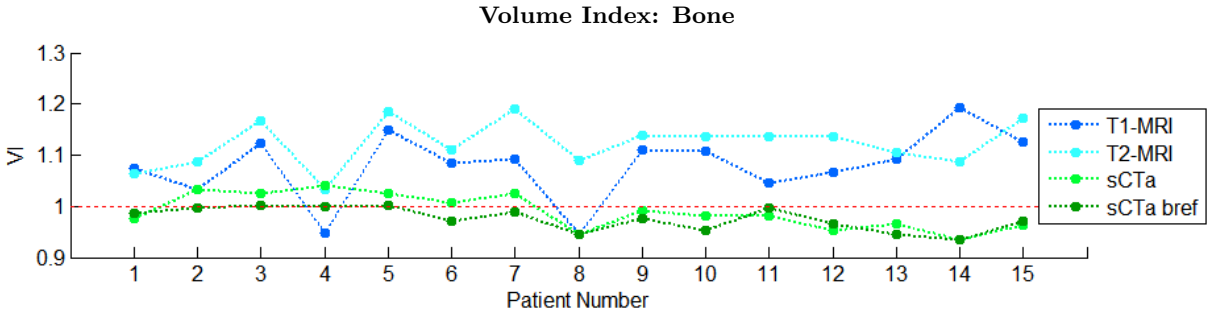

Figure 4.59: Volume Index (VI) results calculated for Bone ROI for all 15 prostate patients.

For the LFem contours, in Figure 4.60, it's difficult to see trends however, obvious deviations between scans are noticed. For all 15 patients, MRI based contours are smaller than the clinical contours confirming the achieved difficulties when performing bone based delineations using MRI as seen before. Significant volumes differences between scans are found and a maximum deviation of $35cm^3$ is verified for CT-sCT_a/MRI scans.

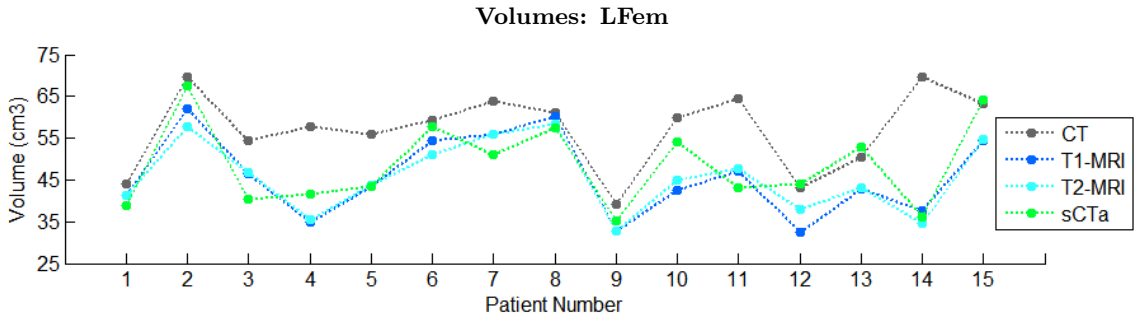

Figure 4.60: Volume changes in cm^3 for CT - (grey), T1-MRI (blue), T2-MRI (cyan) and sCT_a (green) based delineations calculated for LFem ROI for all 15 prostate patients.

For the remaining OAR - rectum (Figure 4.61) and bladder - the results were similar. For the rectum contours, no clear trend is visible. A maximum deviation of 73 cm^3 and 32 cm^3 is seen for CT-MRI and CT-sCT_a combinations, respectively. Similarly to the H&N patients, these differences in OAR delineation are considered significant.

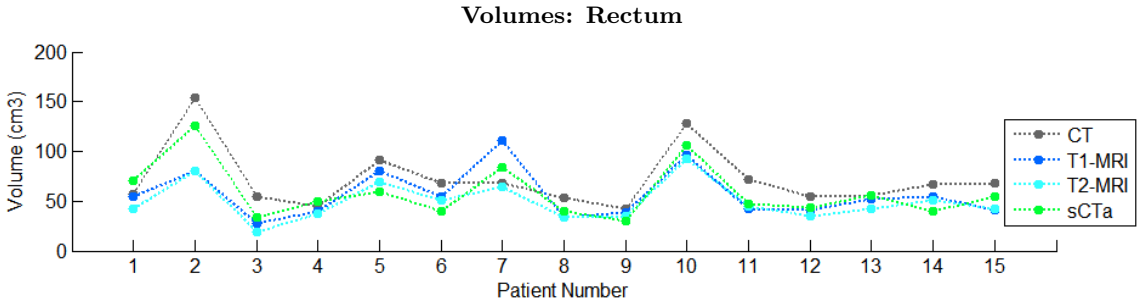

Figure 4.61: Volume changes in cm^3 for CT - (grey), T1-MRI (blue), T2-MRI (cyan) and sCT_a (green) based delineations calculated for Rectum ROI for all 15 prostate patients.

For the prostate contours in Figure 4.62, a clear similarity between sCT_a and CT based delineations is observed for all 15 patients. Due to high soft tissue contrast offered by MRI, MRI based contours are always smaller than the original clinical contours. A significant maximum deviation between CT and MRI/sCT_a based volumes equal to 40 cm^3 is found.

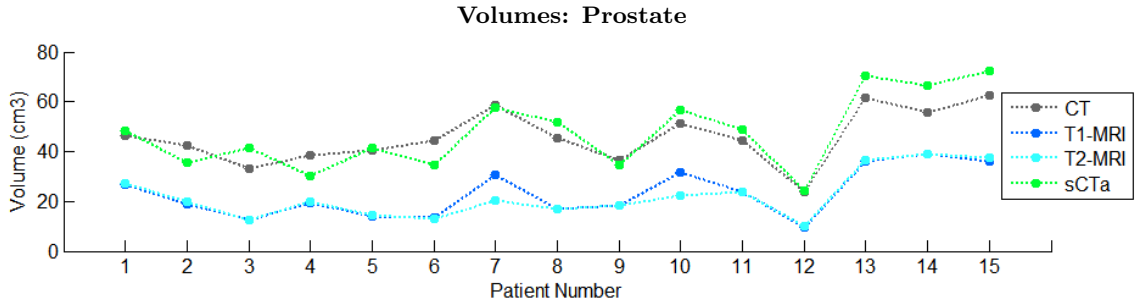

Figure 4.62: Volume changes in cm^3 for CT - (grey), T1-MRI (blue), T2-MRI (cyan) and sCT_a (green) based delineations calculated for Prostate ROI for all 15 prostate patients.

4.2.2.3 Overall evaluation of volume, shape, position and orientation changes

With the same purpose as for the H&N patients, the DSC was calculated for external, bone, prostate and OAR contours. The DSC obtained for external, bone and prostate are shown in Figures 4.63 - 4.65, respectively to illustrate the existence of trends.

For the external contours, the obtained DSC values lie within the following intervals: [0.92;0.96] for CT-MRI and [0.96;0.99] for CT-sCT_a. A high overall similarity with the original contours is achieved for all scans. However, despite the high DSC values obtained, a trend is clearly denoted. In Figure 4.63, it's possible to see two well separated regions, one comprising the results from the sCT_a delineations and another comprising the results from the MRI delineations. These differences for external delineation are in agreement with the result of the Kruskal-Wallis test (p-value=$5.452e^{-7}$). Improving the boundary definition on MRI scans (see section 4.2.1.1) and using the same fixation devices during imaging sessions might decrease these seen differences between CT, MRI and sCT_a contours.

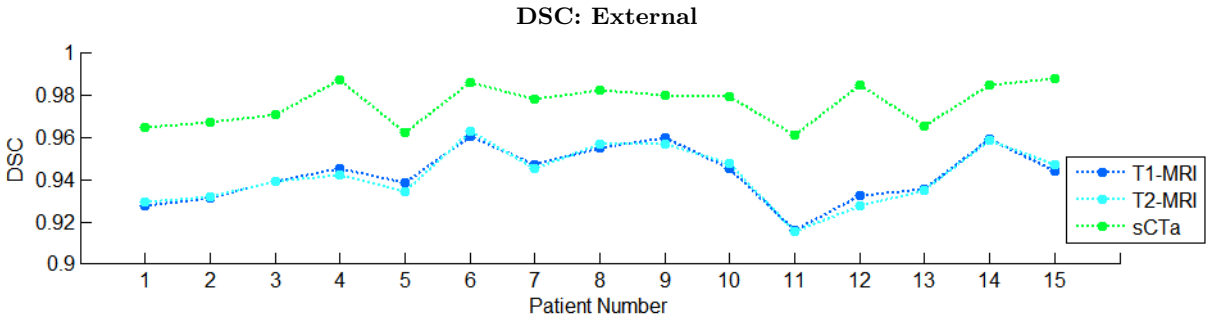

Figure 4.63: DSC values calculated for CT contours comparison with T1-MRI (blue), T2-MRI (cyan) and sCT_a (green) contours for External ROI for all 15 prostate patients.

For bone contours, the following DSC values were obtained: [0.80;0.89] and [0.91;0.95] for CT-MRI and CT-sCT_a/sCT_a_bref respectively. In Figure 4.64, an evident difference between DSC values for MRI and sCT_a based delineations can be seen. A clear similarity between sCT_a and CT contours is denoted, as expected. Performing a bone refinement during sCT_a generation does not imply a general improvement in bone delineation for prostate patients. These results are in agreement with the results for the Kruskal-Wallis test (p-value=$1.113e^{-9}$).

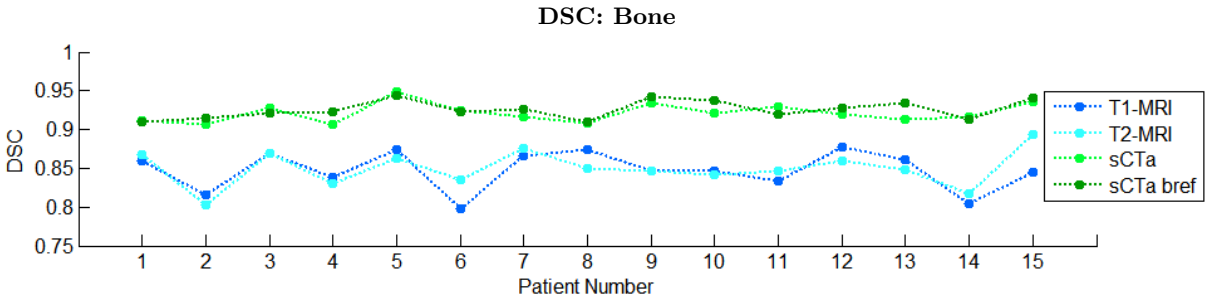

Figure 4.64: DSC values calculated for CT contours comparison with T1-MRI (blue), T2-MRI (cyan), sCT_a (green) and sCT_a_bref (dark green) contours for Bone ROI for all 15 prostate patients.

For both LFem and RFem contours, the DSC values lie within the following intervals: [0.60;0.90] for CT-MRI and [0.68;0.97] for CT-sCT_a. No significant differences are found between MRI and sCT_a based delineations for both contours (p-value=0.905/0.809 for LFem and RFem, respectively). Despite that, DSC values are greater for sCT_a scans for the majority of the patients.

For the bladder contours, the DSC values lie within the following intervals for CT-MRI and CT-sCT_a, respectively: [0.4;0.94] and [0.62;0.89]. For the rectum contours, the DSC intervals are equal to: [0.23;0.76] and [0.56;0.85] for CT-MRI and CT-sCT_a, respectively. The Kruskal-Wallis test shows significant differences between scans (p-value=0.002/0.009 for the bladder and the rectum, respectively). Despite the fact that for the H&N patients the OAR delineation didn't showed significant differences between scans, for the prostate patients a high degree of dissimilarity is seen. These differences might be enlarged as a result of organ motion. Despite the fact that the scans were taken on the same day, bladder filling variations can affect the volume and position of nearby structures.

For the prostate contours in Figure 4.65, a trend is seen as the DSC values are clearly divided in two different regions. A greater similarity is found between sCT_a and original clinical contours. The significant differences between MRI and sCT_a based delineations are in agreement with the Kruskal-Wallis test results (p-value= $6.127e^{-6}$). Despite a greater similarity between sCT_a and CT based delineations is seen for the majority of the OAR and the prostate contours, this does not mean that these represent the best achievable result. It's common notion that OAR and target delineation can be accurately performed when using MR images.

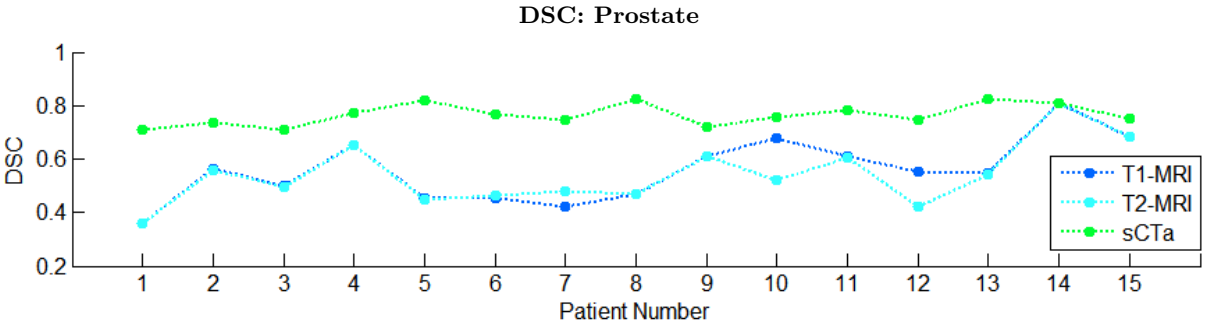

Figure 4.65: DSC values calculated for CT contours comparison with T1-MRI (blue), T2-MRI (cyan) and sCT_a (green) contours for Prostate ROI for all 15 prostate patients.

4.3 Magnetic Field Induced Dose Effects

In this section, we address the question if dose effects introduced by a magnetic field, as present in MR-LINACs, can be accurately predicted when using sCTs during dose calculations. Dose calculations based on the original planning CT and based on the different sCT were performed in the presence of magnetic fields with different strengths: 0.5T and 1.5T. The major objective was to see if the same dosimetric effects are seen due to the magnetic field when using the original CT and the different sCTs scans for dose calculations.

The increase in dose, due to the ERE, is especially manifested at the most superficial voxels of the skin. The most significant change in dose distribution in the skin is found in voxels in a range of around 20-40 Gy. In Figure 4.66, a zoom of the voxels at the patient surface is shown and one can see that for calculations based on the original CT scan, we obtained voxels with 10-20 Gy dose values in a 0T situation, 20-30 Gy in a B=0.5T situation and 30-40 Gy in a B=1.5T situation. This 20 Gy dose increase, when having the magnetic field turn on, is also visible on the DD maps in Figure 4.69 in the outer voxels. Similar effects are observed when performing the calculations on the sCT_{bda}-T2-MRinfo and sCT_a. The dose differences at the boundary are in the same order of magnitude (Figures 4.67 and 4.68, respectively).

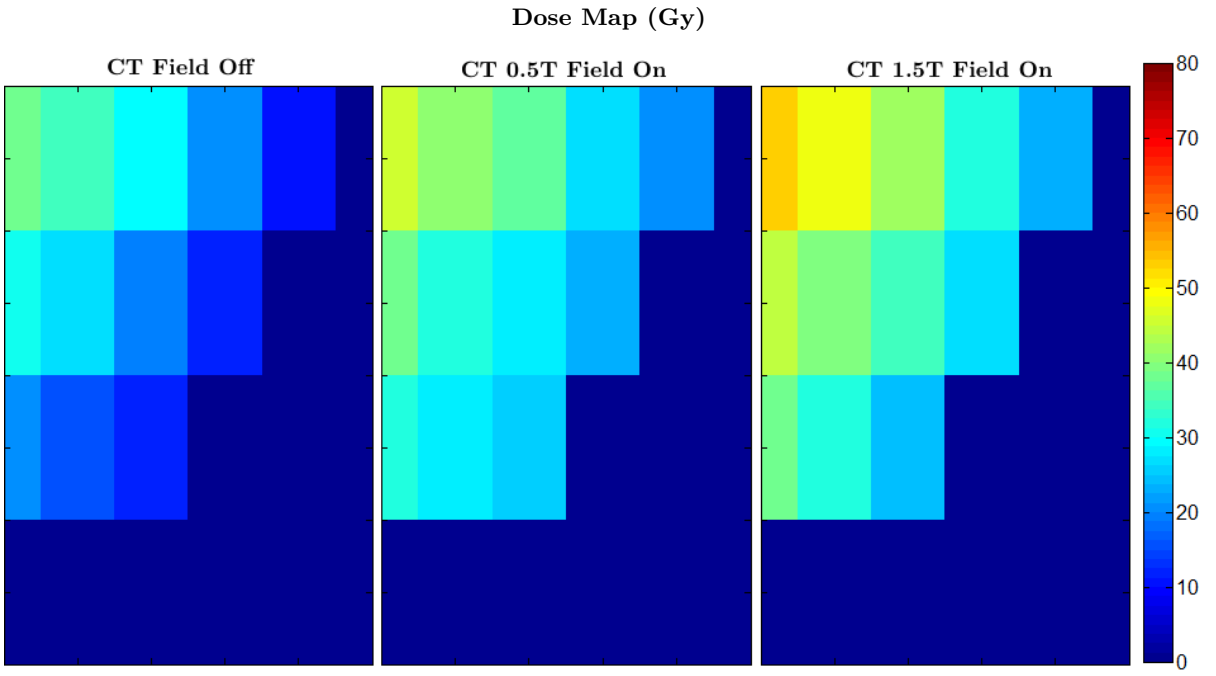

Figure 4.66: Zoom performed on the outer voxels for dose calculations based on the CT scan in the presence of magnetic fields of 0T (left) 0.5T (middle) and 1.5T (right).

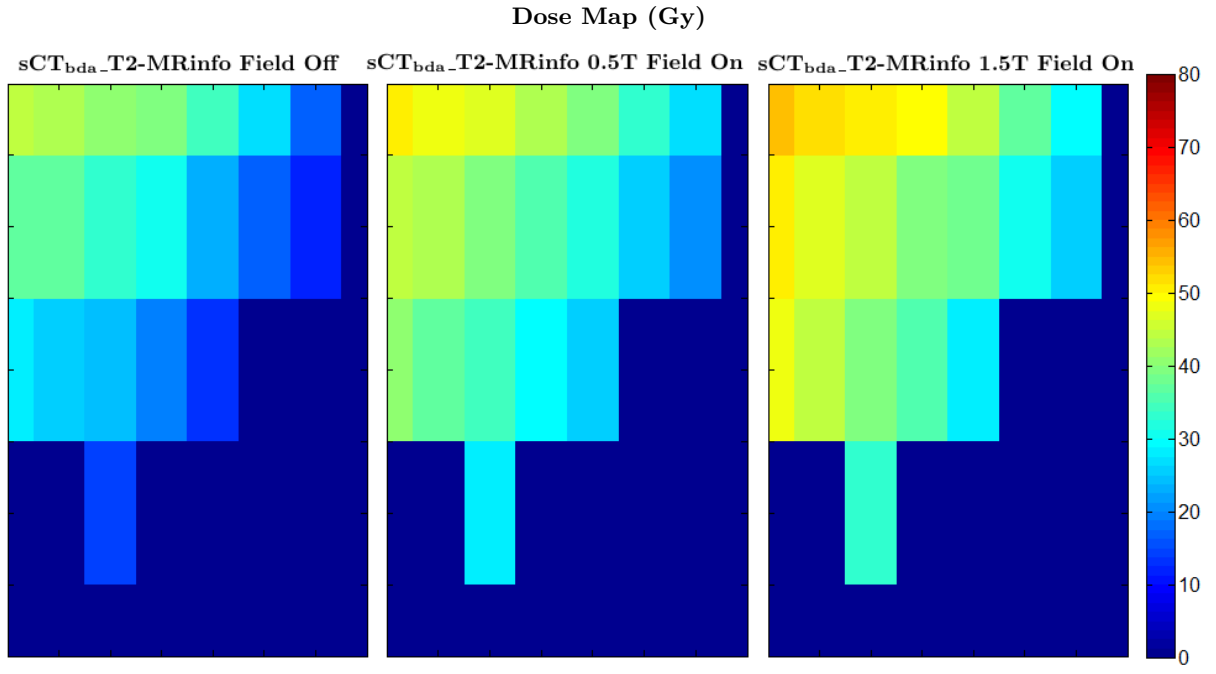

Figure 4.67: Zoom performed on the outer voxels for dose calculations based on the sCT_{bda}_T2-MRinfo scan scan in the presence of magnetic fields of 0T (left) 0.5T (middle) and 1.5T (right).

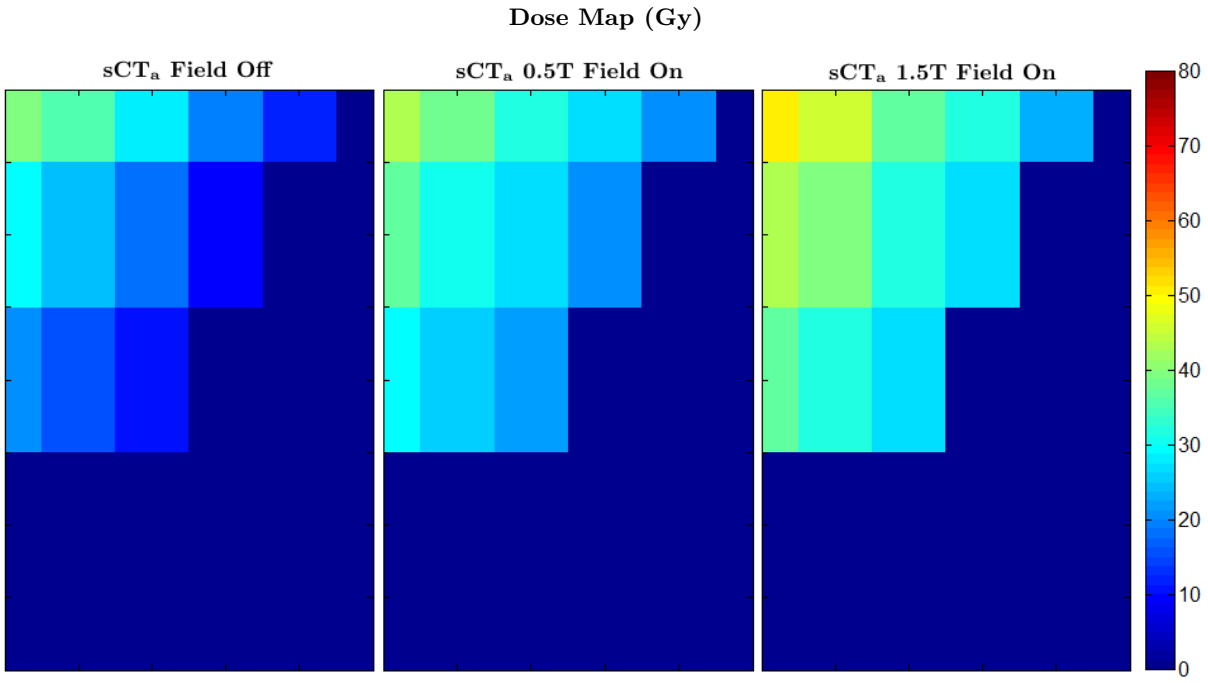

Figure 4.68: Zoom performed on the outer voxels for dose calculations based on the sCT_a scan in the presence of magnetic fields of 0T (left) 0.5T (middle) and 1.5T (right).

In Figures 4.69 - 4.71 one can see the DD maps showing absolute dose differences between -20 and 20 Gy. In agreement with the results shown before, a skin dose increase of 20 Gy is verified for dose calculations performed on CT (Figure 4.69), sCT_{bda}-T2-MRinfo (Figure 4.70) and sCT_a scans (Figure 4.71). The dose differences in the patient centre are not as significant as the dose differences verified at the patient boundary and only range around -5/5 Gy, represented mostly by the green-yellow colours.

For the two different magnetic field strengths, similar mean target coverage is achieved for all methods. Relative to the situation of 0T, using either 0.5T or 1.5T, a maximum absolute median dose increase equal to 0.7 Gy was achieved for CT and equal to 0.5 Gy for both sCT_{bda}-T2-MRinfo and sCT_a for PTV1 ROI. A maximum median dose increase of 1.3 Gy for CT and of 0.5 Gy for sCT_{bda}-T2-MRinfo and sCT_a was achieved for PTV2 ROI.
As PTV1 and PTV2 were defined close to the patient surface (see Figure 3.10 in section 3.4.1), it was expected to see a dose increase in those contours. Despite being relatively small, this dose increase was always visible in the DVH (Figure 4.72) and similar for all patients. Figure 4.72 shows a representative DVH for PTV2 overlaid for a dose calculation with a magnetic field of 0T, 0.5T and 1.5T present, for all methods.

Despite the dose increase with the magnetic field was not remarkably evident when looking at the median dose given to the PTV1, this increase was however more strongly manifested on the D2% given to the same which is a good indicator of the maximum dose received by the contour. The absolute dose difference between CT and sCT dose calculations for PTV1 increased to 3.5 Gy for CT scans, 2.5 Gy for sCT_{bda}-T2-MRinfo and 2 Gy for sCT_a when using D2%.

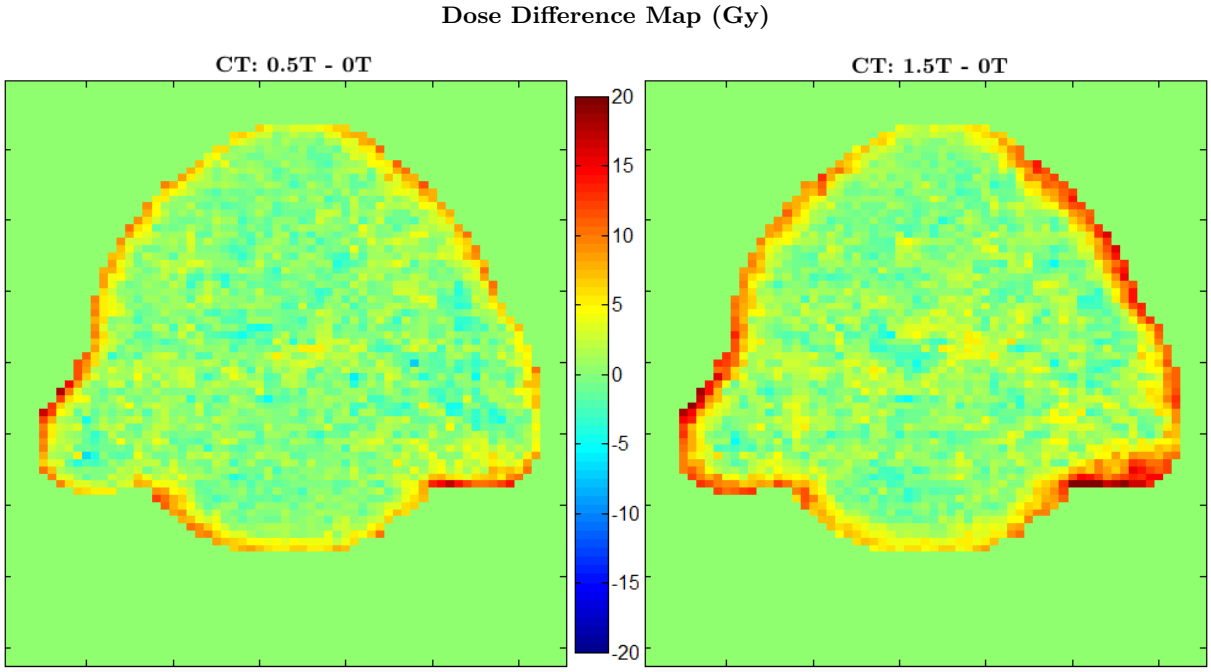

Figure 4.69: Dose difference maps between a situation with the magnetic field turned on with 0.5T (left) and 1.5T (right) field strength and a situation with the magnetic field turned off for CT scans (scale in Gy).

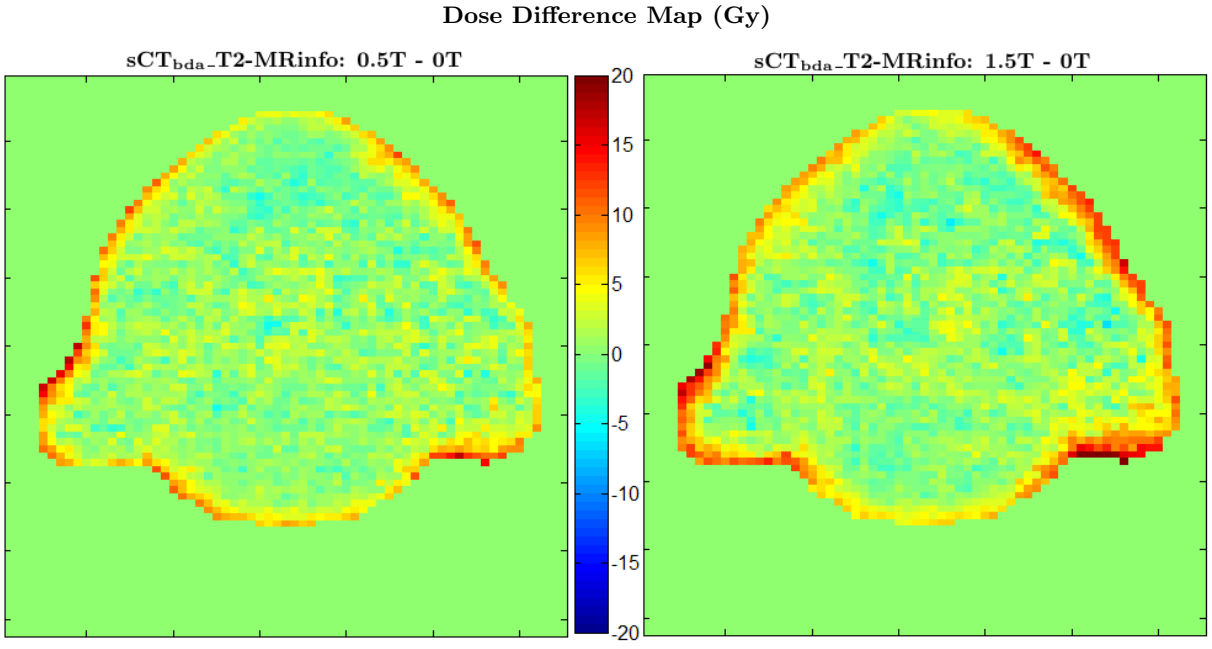

Figure 4.70: Dose difference maps between a situation with the magnetic field turned on with 0.5T (left) and 1.5T (right) field strength and a situation with the magnetic field turned off for sCT_{bda}_T2-MRinfo scans (scale in Gy).

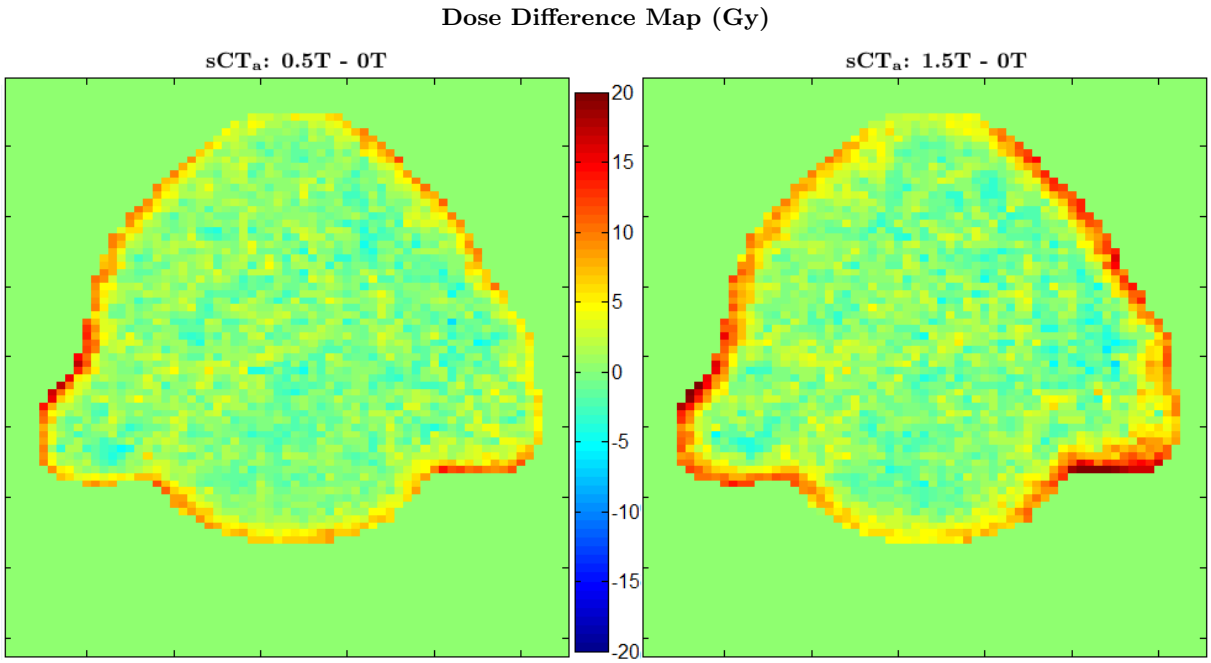

Figure 4.71: Dose difference maps between a situation with the magnetic field turned on with 0.5T (left) and 1.5T (right) field strength and a situation with the magnetic field turned off for sCT_a scans (scale in Gy).

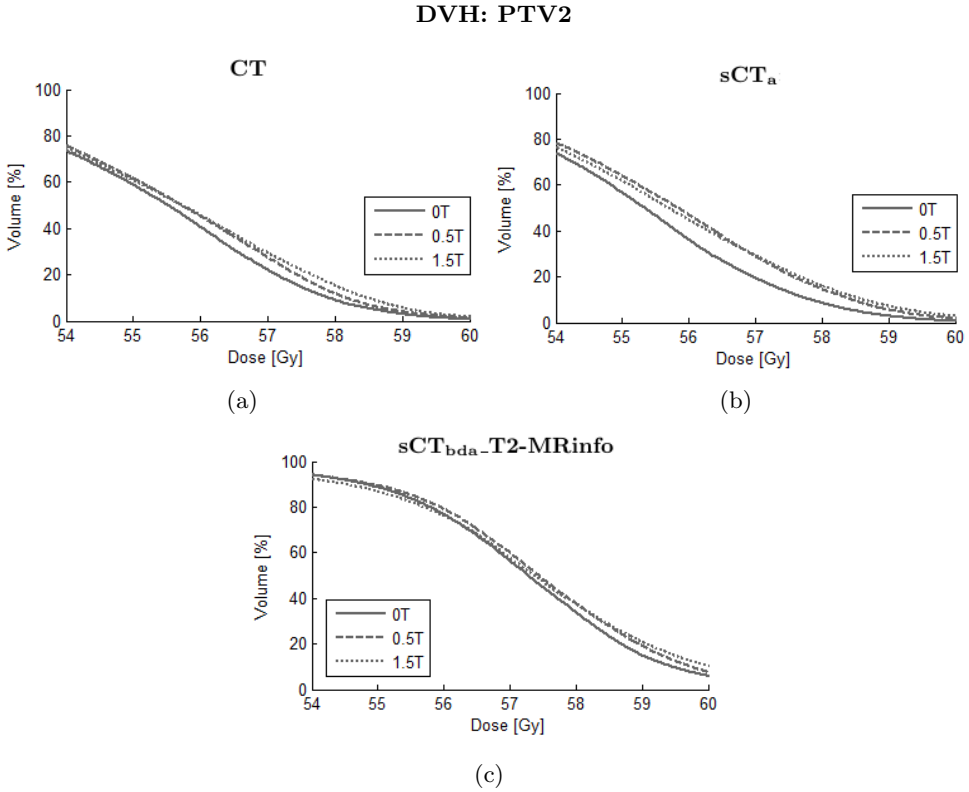

Figure 4.72: DVH for PTV2 for one representative H&N patient for 0T, 0.5T and 1.5T situations for all scans used: CT (a), sCT_a (b) and sCT_{bda}-T2-MRinfo (c).

The SpinalCord dose is unaffected by the presence of a magnetic field in all scenarios (Figure 4.73). As the spinal cord is not situated close to a tissue-air interface, this result was expected.

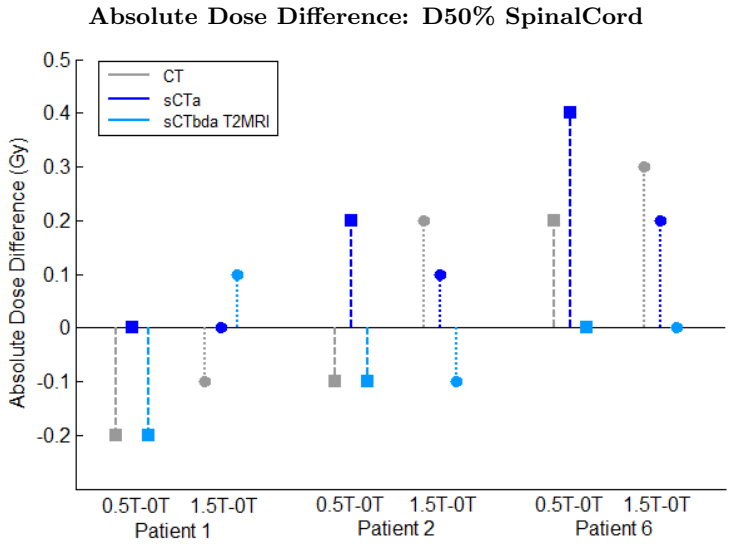

Figure 4.73: Absolute Dose Difference between a situation with the magnetic field turned on with both 0.5T and 1.5T field strength for SpinalCord D50% for all scans: CT (grey), sCT_a (blue) and sCT_{bda}-T2-MRinfo (light blue).

To perform an overall evaluation of the magnetic field induced dose effects not to a specific area but to the patient's outline the percentage volume that denotes a dose difference between the situations of having the magnetic field turn on and off bigger than 5%, 10% and 20% of the prescribed dose (3.25 Gy, 6.5 Gy and 13 Gy respectively) was calculated. Furthermore, the maximum dose increase relative to the maximum dose in a B=0T situation was calculated for all patients when using each type of CT scan.

The results for the first part are presented in Table 4.3, showing minimal and maximal values seen in the 3 evaluated patients. The percentage volume, where the dose difference in both B=0.5T and B=1.5T situations compared to B=0T is bigger than 5%, 10% and 20% of the prescribed dose, is 12-25%, 2-8% and 0-2%, respectively for all methods. These ranges were similarly represented for CT and sCT based dose calculations. In Table 4.3, one can see that the majority of the volume has a dose increase smaller than 3 Gy when turning the magnetic field on while only a small percentage faces dose increase bigger than 13 Gy for all methods. These results are consistent with the DD and DVH results presented previously.

The results for the maximum dose increase due to the ERE showed that despite small variations, both dose calculations performed on CT and on sCT revealed similar effects of increased dose when switching on a magnetic field. Dose increases are up to 35% for B=0.5T and 45% for B=1.5T.

Table 4.3: Percentage volume with dose difference higher than 5%, 10% and 20% of the prescribed dose for a situation of 0.5T and 1.5T field strength against 0T. The values are presented in ranges including the lowest and highest percentage seen in all patients, respectively. PD stands for Prescribed Dose.

	Percentage Volume (%)					
	CT		**sCT_{bda}-T2-MRinfo**		**sCT_a**	
Dose Difference	**0.5T-0T**	**1.5T-0T**	**0.5T-0T**	**1.5T-0T**	**0.5T-0T**	**1.5T-0T**
> 5% PD	12.4 - 22.5	17.7 - 25.1	11.7 - 13.1	17.8 - 19.3	10.5 - 17.2	17.1 - 19.1
> 10% PD	3.6 - 5.3	7.5 - 8.0	3.2 - 3.7	6.7 - 7.5	2.3 - 6.8	6.7 - 7.5
> 20% PD	0.1 - 0.5	0.5 - 1.9	0.1 - 0.6	0.7 - 1.2	0.1 - 1.4	0.8 - 1.5

Finally, after showing that dose calculations based on sCT scans are capable of reproducing the skin dose effects, we also investigated if the same is true for effects around air cavities. Dose distribution around air cavities in the presence of magnetic fields are characterized by a region of reduced dose and another of increased dose. The region of reduced/increased dose is caused by the fact that electrons cannot cross the cavity as they are forced to turn back by the magnetic field. This causes a dose increase when the beam enters an air cavity and causes a dose decrease when the beam exits an air cavity. This heterogeneous dose distribution is dependent on the strength of the magnetic field and also on the cavity diameter. When the cavity diameter is small relative to the in- air- electron- trajectory- radius, the electrons can cross the cavity in quasi-straight lines and as a result, the dose distribution is equal as without a cavity. This pattern is seen for all magnetic field strengths, however when having a strong magnetic field, the cavity diameter where the dose distribution still remains homogeneous is much smaller. To evaluate this effect absolute DD maps - 0.5T-0T and 1.5T-0T - were plotted for each scan in a dose scale from -20 to 20 Gy. DD maps are displayed in Figures 4.74 - 4.76.

In Figure 4.74, for dose calculations based on CT scans it's possible to see that, for both B=0.5T and B=1.5T, a heterogeneous dose distribution is obtained, when calculating the absolute DD maps. A region of high and low dose is seen in the patient at the location of the throat. Especially for B=1.5T, the increased and decreased dose are well visible. This is because the in-air- electron- trajectory- radius of secondary electrons becomes smaller with increasing magnetic field strength. Thus, for B=1.5T less electrons are capable of crossing the air cavity than for B=0.5T.

For both sCT scans, it's possible to see in Figure 4.75 and 4.76 that this effect cannot clearly be visualized. For B=0.5T the effect is totally misrepresented. For dose calculations performed at the sCT_{bda}-T2-MRinfo with a B=1.5T magnetic field (Figure 4.75) some resemblance can be seen, but much smaller than at the dose calculations based on the original CT. For the dose calculations based on the sCT_a (Figure 4.76) almost a homogeneous dose distribution in the patient centre is observed, as if no air cavity is present. For sCT dose calculations, the effects are more pronounced when using sCT_{bda}-T2-MRinfo as in this scan a very sharp boundary between air and tissue is defined. For sCT_a dose calculations, the effects are totally misrepresented due to the blurriness introduced by the method in the final scan.

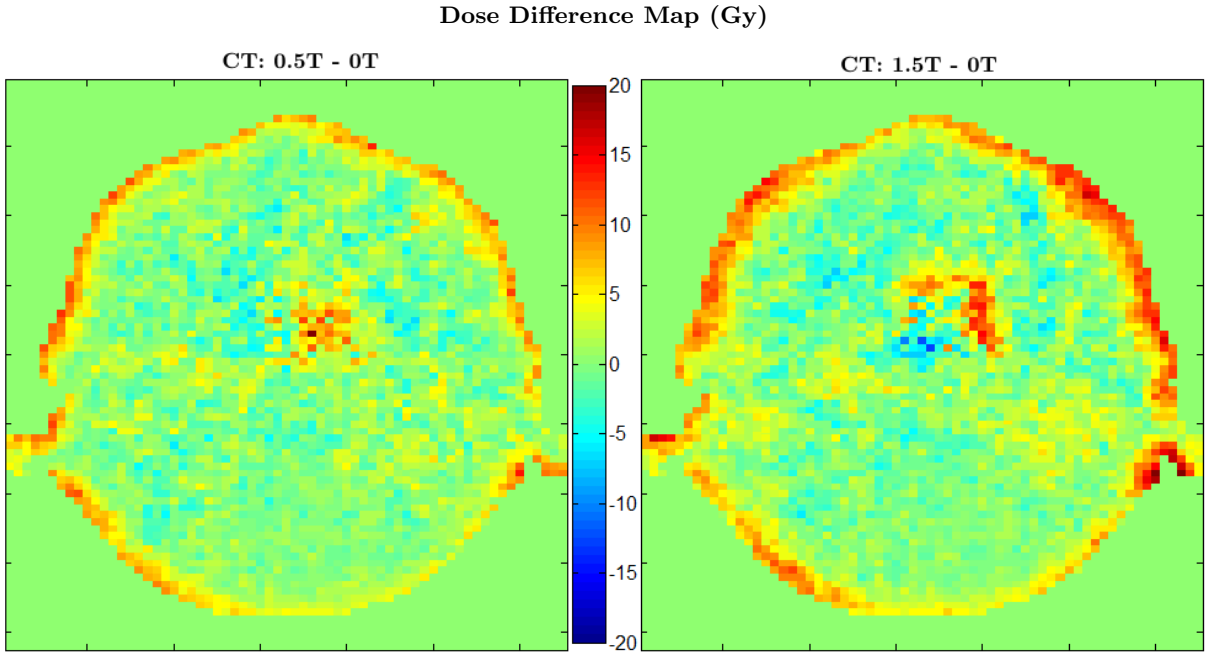

Figure 4.74: Dose difference maps between a situation with the magnetic field turned on with 0.5T (left) and 1.5T (right) field strength and a situation with the magnetic field turned off for CT scans in the presence of an air cavity (scale in Gy).

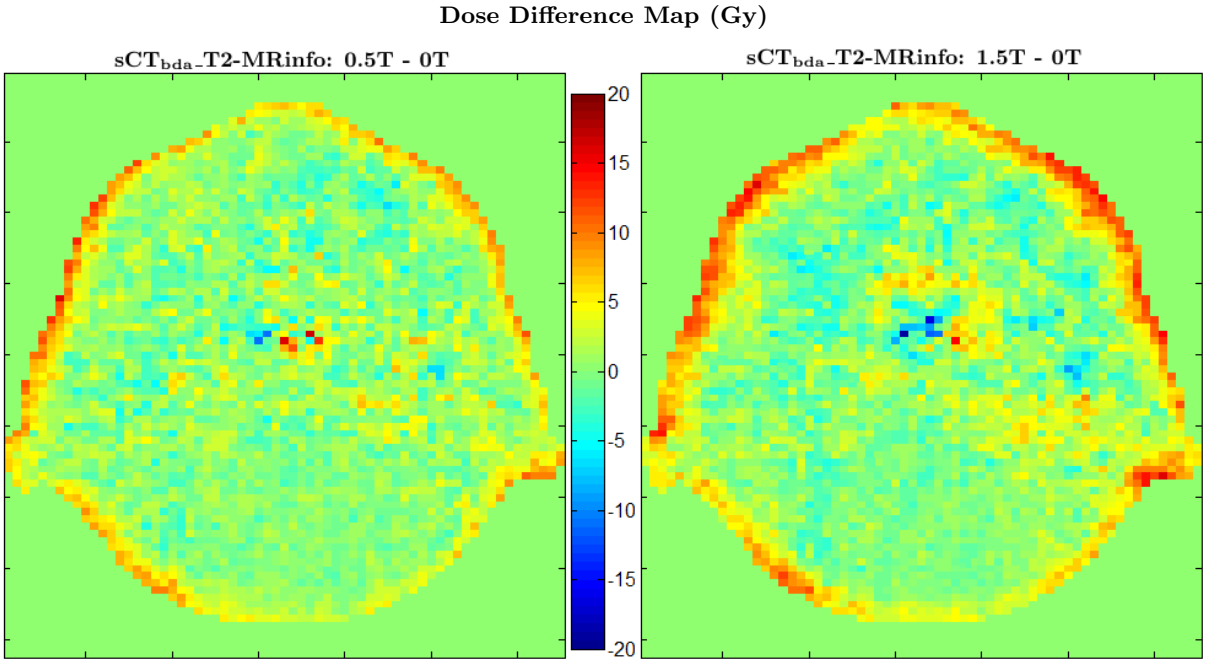

Figure 4.75: Dose difference maps between a situation with the magnetic field turned on with 0.5T (left) and 1.5T (right) field strength and a situation with the magnetic field turned off for sCT_{bda}-T2-MRinfo scans in the presence of an air cavity (scale in Gy).

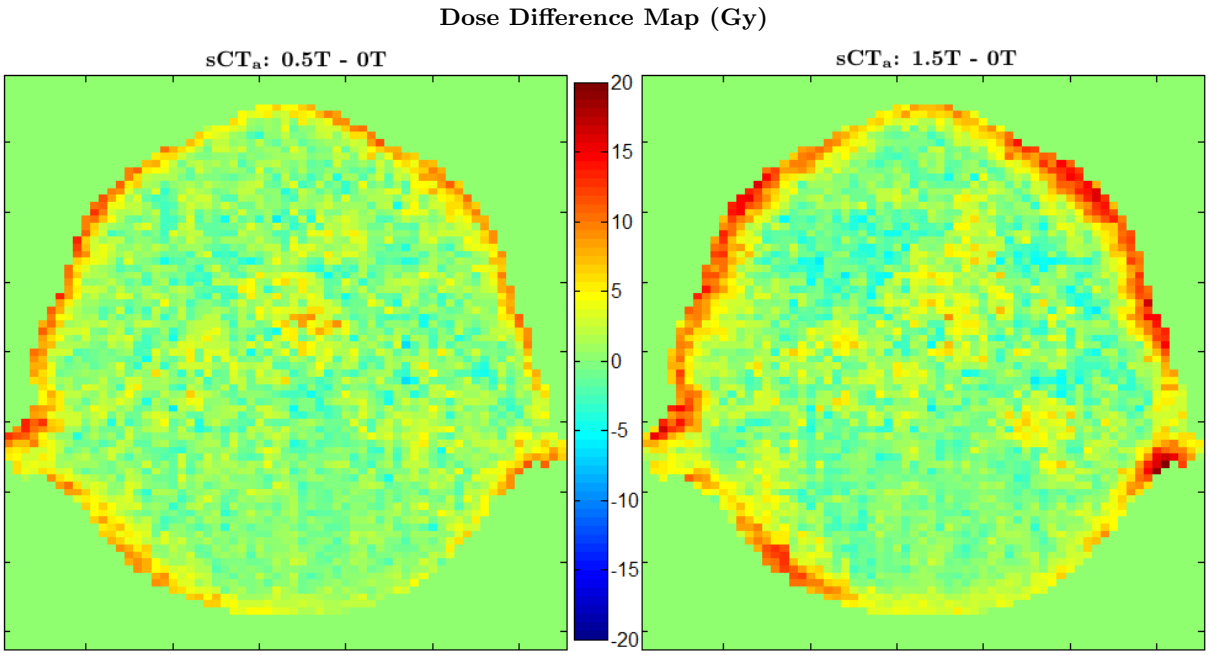

Figure 4.76: Dose difference maps between a situation with the magnetic field turned on with 0.5T (left) and 1.5T (right) field strength and a situation with the magnetic field turned off for sCT_a scans in the presence of an air cavity (scale in Gy).

Chapter 5

Conclusion and Future Work

MRI-only RTP is receiving increasing attention, as MRI becomes more integrated into modern RT. This raises the question of when it's clinically acceptable to perform RTP based on MRI as the only modality instead of using the traditional CT. In this thesis, a population based study, comparing CT based dose calculations with those carried out based on sCT scans achieved by Bulk Density Assignment and Atlas methods is performed. The assurance of a clinically acceptable dosimetric accuracy for sCTs is of key importance to establish a MRI-only external RTP workflow. Ensuring the establishment of a precise geometry for the patient within the sCT is also very important for patient positioning at treatment, especially at MR-LINAC machines, and target margins reduction when performing clinical delineations.
After performing a dosimetric as well as a geometrical evaluation two important questions should be addressed:
Is MR information's sufficient for treatment planning?
Do Bulk Density Assignment method or Atlas method provide a better basis for an MRI-only workflow?

Dose distributions based on sCT_{bda} and on sCT_{a} were compared to clinical dose distributions based on the original planning CT in terms of clinically relevant DVH points and in terms of 2D gamma analysis.
Three different approaches to generate sCT_{bda} were evaluated in this thesis. For the sCT_{bda}_CTinfo method, tissue classes in the original CT were segmented and assigned to approximated densities. The purpose of this method was to evaluate the influence of a rough density estimation on the accuracy of the dose distribution. In the sCT_{bda}_MRinfo method, the tissue class segmentation was based on the MRI scans, both T1- and T2- weighted. Thus, this method was used to evaluate MRI delineation uncertainty in addition to a rough electron density estimation. Dose distribution based on sCT_{bda}_CTinfo showed slightly better agreement with the original dose distribution than both sCT_{bda}_MRinfo. This was expected as sCT_{bda}_CTinfo introduces less variation to the real CT geometry. As sCT_{bda}_CTinfo relies on CT information, its implementation to establish an MRI-only workflow would not be viable. This method was only used to assess the performance of tissue class delineation when using MRI. For both T1- and T2-MRinfo sCT_{bda} as well as for sCT_{bda}_CTinfo no clinically significant differences were found.
In addition to Bulk Density Assignment methods, Atlas based methods were investigated for the generation of sCTs to determine which method is the best guess for geometry and electron density estimation. Similar dosimetric results were obtained for sCT_{a} generated with and without bone refinement. Dose distributions based on sCT_{a} showed slightly better PTV coverage and a more homogeneous gamma map with lower gamma values than sCT_{bda}_MRinfo. As for the Atlas methods a one-to-one estimation for each electron density voxel value is assigned, a greater similarity with the original dose distributions is expected to be obtained. However, differences seen between sCT_{a} and sCT_{bda} were not clinically significant.

Regarding the investigated dosimetric measures, it's possible to conclude that when performing dose re-calculations on either sCT_a or sCT_{bda}, no significant differences to the calculations based on the original CT are seen. Thus, both methods would be suitable to perform dose calculations for treatment planning for both H&N and prostate patients.

The feasibility of a MRI- based treatment planning will not only rely on an accurate method to derive CT equivalent data from MR data but also on the ability to delineate structures - both target volume, OAR and tissue classes - on the MRI alone. In addition to a dosimetric evaluation of the sCTs, a geometric evaluation was performed to compare different delineation methods: CT based (used for sCT_{bda}_CTinfo), MRI based (used for sCT_{bda}_MRinfo) and sCT_a based delineation. OAR and tissue classes (bone and external contours) delineated on the original planning CT, on the T1- and T2-MRIs and on the sCT_a were assessed in terms of shape, volume and position.
The following main conclusions can be retrieved: Concerning tissue class's delineation, the external and bone contours were very similar in shape, position and volume when being delineated at either the original planning CT or sCT_a. sCT_a_bref provided improvements in bone definition compared to sCT_a for the majority of the H&N and the prostate patients. When comparing external and bone delineations on MRI and CT scans, as performed for sCT_{bda}_MRinfo and sCT_{bda}_CTinfo respectively, obvious deviations in shape and in volume could be observed. Differences in bone delineation arise due to poor bone visibility in MRI scans. Differences in the delineation of the body contour arise due to differences in the set-up between the CT and MR imaging. External contour delineation was obstructed due to water fat shift effects occurring at the patient surface in the MRI scans. Also, external delineation differences were overestimated due to a lack of coverage in the MRI scans for the H&N patients and due to the use of different couches during MR and CT imaging for the prostate patients.
Despite the fact that for the majority of patients clear deviations were seen for MRI and CT based delineations, when carrying out an overall evaluation using DSC, both bone and external contours showed to be similar.

For the OAR no significant conclusions could be found. Contours based on sCT_a and MRI showed clear differences from the original clinical CT contours in shape, position and volume. However, it's common notion that soft tissue delineations can be more accurately performed when using MR instead of CT images. Thus, it's difficult to decide which delineation, CT or MRI based delineation, presents the gold standard. In general, sCT_a does not provide enough anatomic information for target volume and OAR delineation. However, bone and external delineation using sCT_a can be performed automatically and with a high degree of similarity with original CT based contours, used as ground-truth for bone and external comparisons. For MRI based delineations (used for the sCT_{bda}_MRinfo method) the opposite situation is prevailing. An accurate delineation of OAR can be performed due to the optimal soft tissue contrast offered by MRI scans while bone delineation is only performed as a best guess due to its low intensity signal when using traditional MR sequences.

The implementation of a MRI-only RTP workflow in the context of a MR-LINAC machine presents a special challenge. Here, effects due to the presence of a magnetic field have to be modelled accurately during treatment planning. An evaluation of the reproducibility of the dosimetric effects due to a magnetic field when performing dose calculations on the original planning CT and on both sCT_a and sCT_{bda}_MRinfo was done. For all calculations, a significant increase in skin dose was observed. The magnitude of this dose increase is comparable for all scans. In the presence of large air cavities in patients a significant dose increase is encountered for both high (1.5T) and low (0.5T) magnetic field strengths when using CT scans. This effect was not

reproduced when using both sCT_a and sCT_{bda} for dose calculations. For sCT_a, the effect was totally misrepresented probably due to the blurriness introduced by this method in the final scan. For sCT_{bda}, a better resemblance with the CT dose distribution was achieved probably due to the sharp boundaries defined when applying bulk densities. Regions of high risk could be affected by the dose effects verified around these air cavities due to the presence of a magnetic field. The fact that neither calculations based on sCTs scans could accurately reproduce these dose effects introduces a limitation to the use of sCTs for treatment planning in the presence of a magnetic field for MR-LINAC machines.

The results obtained in this study show that for the use of both sCT_a and sCT_{bda} methods drawbacks are found when employing them for a clinical MRI-only workflow. This is unfortunate, as a robust and automatic generation of sCT data is a pre-requisite for a full scale MRI-only implementation. For sCT_{bda}_MRinfo, manual delineation of bony structures is very time consuming and subject to inter-observer variability, making this method not feasible for clinical use. Segmentation using sCT_a can be performed automatically however, the blurriness introduces delineation uncertainties. Also, sCT_a scans do not provide any useful information for target delineation as the tumour looks different in each patient. Thus, the atlas is not capable of reproducing the same tumour localization, size and shape for the generation of each sCT_a. Furthermore, the registration processes involved in the methodology introduces an error of unknown magnitude.

Trying to overcome the limitation of both methods, sCT_a and sCT_{bda}, we suggest combining soft tissue contours and target delineation based on MRI with bone contours obtained from sCT_a. Since sCT_a is created in the same space as the MRI, the definition of soft tissue structures (as the OAR) and the target on the MRI can be easily propagated to the sCT_a for planning. As bony structures in the sCT_a images showed to be consistent with the original CT one, this scan could also be used for patient positioning, at least for H&N patients where positioning relies on accurate bone geometry definition. For prostate patients, where patient positioning is done with fiducial markers, markers that are visible in MRI scans would have to be used for positioning.

The limitations of a reduced FOV for the MRI scans that hindered some investigations in this study, should be easy to overcome in the future when radiologists are aware that MRI scans will also be used for treatment planning. Imaging protocols would have to be adapted to not only cover the PTV region, but to image the entire body contour. Also, to build reliable atlases, CT and MR images for a number of patients in the treatment position and using the same fixation devices are needed. sCT_a scans should become available latest with the introduction of the MR-LINAC, where imaging and treatment delivery can be performed at the same time. The need for achieving sharper boundaries in sCT_a scans is also of key importance for the use of the MR-LINAC for treatment planning.

Finally, it has been seen in this study that an MRI-only workflow is especially challenging to be implemented for patients that show anatomical exceptions, like for example metal implants. Dose calculations performed on sCT_a and sCT_{bda} for a prostate patient with a hip implant showed clinically significant deviations from the original planning CT dose calculations. For these patients, a traditional CT RTP workflow is preferable.

Bibliography

[1] C. Rasch, I. Barillot, P. Remeijer, A. Touw, M. Van Herk, and J. V. Lebesque, "Definition of the prostate in CT and MRI: A multi-observer study", Int. J. Radiat. Oncol. Biol. Phys., vol. 43, no. 1, pp. 57–66, 1999.

[2] C. Rasch, R. Steenbakkers, and M. Van Herk, "Target definition in Prostate, Head, and Neck", Semin. Radiat. Oncol., vol. 15, no. 3, pp. 136–145, 2005.

[3] T. Nyholm, M. Nyberg, M. G. Karlsson, and M. Karlsson, "Systematisation of spatial uncertainties for comparison between a MR and a CT-based radiotherapy workflow for prostate treatments", Radiat. Oncol., vol. 4, p. 54, 2009.

[4] K. Ulin, M. M. Urie, and J. M. Cherlow, "Results of a multi-institutional benchmark test for cranial CT/MR image registration", Int. J. Radiat. Oncol. Biol. Phys., vol. 77, no. 5, pp. 1584–1589, 2010.

[5] C. J. Dean, J. R. Sykes, R. a. Cooper, P. Hatfield, B. Carey, S. Swift, S. E. Bacon, D. Thwaites, D. Sebag-Montefiore, and a. M. Morgan, "An evaluation of four CT-MRI co-registration techniques for radiotherapy treatment planning of prone rectal cancer patients", Br. J. Radiol., vol. 85, no. 1009, pp. 61–68, 2012.

[6] M. Karlsson, M. G. Karlsson, T. Nyholm, C. Amies, and B. Zackrisson, "Dedicated Magnetic Resonance Imaging in the Radiotherapy Clinic", Int. J. Radiat. Oncol. Biol. Phys., vol. 74, no. 2, pp. 644–651, 2009.

[7] B. W. Raaymakers, J. J. W. Lagendijk, J. Overweg, J. G. M. Kok, a J. E. Raaijmakers, E. M. Kerkhof, R. W. van der Put, I. Meijsing, S. P. M. Crijns, F. Benedosso, M. van Vulpen, C. H. W. de Graaff, J. Allen, and K. J. Brown, "Integrating a 1.5 T MRI scanner with a 6 MV accelerator: proof of concept", Phys. Med. Biol., vol. 54, no. 12, pp. N229–N237, 2009.

[8] J. E. Raaijmakers, B. W. Raaymakers, and J. J. W. Lagendijk, "Integrating a MRI scanner with a 6 MV radiotherapy accelerator: dose increase at tissue-air interfaces in a lateral magnetic field due to returning electrons", Phys. Med. Biol., vol. 50, no. 7, pp. 1363–1376, 2005.

[9] I. Rosenberg, "Radiation Oncology Physics: A Handbook for Teachers and Students", Br. J. Cancer, vol. 98, no. 5, p. 1020, 2008.

[10] S. Wedd, "Intensity-Modulated Radiation Therapy", 2001.

[11] S. Webb, "The physical basis of IMRT and Inverse Planning", Br. J. Radiol., vol. 76, no. 910, pp. 678–689, 2003.

[12] J. L. Bedford and A. P. Warrington, "Commissioning of Volumetric Modulated Arc Therapy (VMAT)", Int. J. Radiat. Oncol. Biol. Phys., vol. 73, no. 2, pp. 537–545, 2009.

[13] J. L. Bedford, V. Nordmark Hansen, H. a McNair, A. H. Aitken, J. E. C. Brock, A. P. Warrington, and M. Brada, "Treatment of lung cancer using volumetric modulated arc therapy and image guidance: a case study", Acta Oncol., vol. 47, no. 7, pp. 1438–1443, 2008.

[14] G. C. Barnett, C. M. L. West, A. M. Dunning, R. M. Elliott, C. E. Coles, P. D. P. Pharoah, and N. G. Burnet, "Normal tissue reactions to radiotherapy: towards tailoring treatment dose by genotype", Nat. Rev. Cancer, vol. 9, no. 2, pp. 134–42, Feb. 2009.

[15] B. Zitová and J. Flusser, "Image registration methods: A survey", Image Vis. Comput., vol. 21, no. 11, pp. 977–1000, 2003.

[16] M. H. and D. J. H. Derek L G Hill, Philipp G Batchelor, "Medical Image Registration", vol. 1, 2001.

[17] J. Ashburner and K. Friston, "Rigid Body Registration", Hum. Brain Funct. Second Ed., pp. 635–653, 2003.

[18] A. Sotiras, C.Davatazikos and N.Paragions, "Deformable Medical Image Registration: A Survey", Research Report No 7919 Project Team GALEN, no. September, p.65, 2012.

[19] M. Goitein, "Radiation Oncology: A Physicist's-Eye View", Springer, New York, 2008.

[20] International Commission on Radiation Units and Measurements (ICRU), Ed., "Prescribing, Recording, and Reporting Photon Beam Therapy (Report 50)", 1993.

[21] International Commission on Radiation Units and Measurements (ICRU), Ed., "Prescribing, Recording, and Reporting Photon Beam Therapy (Report 62)", 2008.

[22] Estro, P. Aletti, and P. Bey, "Recommendations for a Quality Assurance Programme in External Radiotherapy", Booklet n2, Estro. 1995.

[23] R. E. Drzymala, R. Mohan, L. Brewster, J. Chu, M. Goitein, W. Harms, and M. Urie, "Dose-volume histograms", Int. J. Radiat. Oncol. Biol. Phys., vol. 21, no. 1, pp. 71–8, May 1991.

[24] International Commission on Radiation Units and Measurements (ICRU), Ed., "Prescribing, Recording, and Reporting Intensity-Modulated Photon-Beam Therapy (IMRT)(Report 83)", 2010.

[25] J. Van Dyk, R. B. Barnett, J. E. Cygler, and P. C. Shragge, "Commissioning and quality assurance of treatment planning computers", Int. J. Radiat. Oncol. Biol. Phys., vol. 26, no. 2, pp. 261–73, May 1993.

[26] D. a Low, "Gamma Dose Distribution Evaluation Tool", J. Phys. Conf. Ser., vol. 250, p. 012071, 2010.

[27] D. a Low, W. B. Harms, S. Mutic, and J. a Purdy, "A technique for the quantitative evaluation of dose distributions", Med. Phys., vol. 25, no. 5, pp. 656–661, 1998.

[28] T. Depuydt, A. Van Esch, and D. P. Huyskens, "A quantitative evaluation of IMRT dose distributions: Refinement and clinical assessment of the gamma evaluation", Radiother. Oncol., vol. 62, no. 3, pp. 309–319, 2002.

[29] P. J. Hoskin and V. Goh, "Radiotherapy in Practice – Imaging", vol. 4. Oxford Univ Pr, 2010.

[30] J. Bushberg and J. Boone, "The Essential Physics of Medical Imaging", 2011.

[31] W.R.Hendee, "Medical Imaging Physics", Fourth Ed. A JOHN WILEY & SONS INC. PUBLICATION, 2002.

[32] A.Oppelt, "Imaging systems for medical diagnostics: fundamentals, technical solutions, and applications for systems applying ionizing radiation, nuclear magnetic resonance, and ultrasound", Wiley-VCH, 2005.

[33] U. Schneider, E. Pedroni, and a Lomax, "The calibration of CT Hounsfield units for radiotherapy treatment planning", Phys. Med. Biol., vol. 41, no. 1, pp. 111–124, 1996.

[34] W. Rooney, "MRI: From Picture to Proton", vol. 85, no. 4. 2003.

[35] D. Weishaupt, V. D. Kochli, B. Marincek, and E. E. Kim, "How Does MRI Work? An Introduction to the Physics and Function of Magnetic Resonance Imaging", vol. 48, no. 11. 2007.

[36] M. a. Brown and R. C. Semelka, "MRI: Basic Principles and Applications", 2003.

[37] J. Uh, T. E. Merchant, Y. Li, X. Li, and C. Hua, "MRI-based treatment planning with pseudo CT generated through atlas registration", Med. Phys., vol. 41, no. 5, p. 051711, 2014.

[38] S. Langlois, M. Desvignes, J. M. Constans, and M. Revenu, "MRI geometric distortion: a simple approach to correcting the effects of non-linear gradient fields", J. Magn. Reson. Imaging, vol. 9, no. 6, pp. 821–31, Jun. 1999.

[39] L. N. Baldwin, K. Wachowicz, and B. G. Fallone, "A two-step scheme for distortion rectification of magnetic resonance images", Med. Phys., vol. 36, no. 9, pp. 3917–26, Sep. 2009.

[40] V. Keereman, Y. Fierens, T. Broux, Y. De Deene, M. Lonneux, and S. Vandenberghe, "MRI-based attenuation correction for PET/MRI using ultrashort echo time sequences", J. Nucl. Med., vol. 51, no. 5, pp. 812–818, 2010.

[41] M. D. Robson and G. M. Bydder, "Clinical ultrashort echo time imaging of bone and other connective tissues", NMR Biomed., vol. 19, no. 7, pp. 765–80, Nov. 2006.

[42] J. Sjölund, D. Forsberg, M. Andersson, and H. Knutsson, "Generating patient specific pseudo-CT of the head from MR using atlas-based regression", Phys. Med. Biol., vol. 60, no. 2, pp. 825–839, 2015.

[43] J. a. Dowling, J. Lambert, J. Parker, O. Salvado, J. Fripp, A. Capp, C. Wratten, J. W. Denham, and P. B. Greer, "An atlas-based electron density mapping method for magnetic resonance imaging (MRI)-alone treatment planning and adaptive MRI-based prostate radiation therapy", Int. J. Radiat. Oncol. Biol. Phys., vol. 83, no. 1, pp. e5–e11, 2012.

[44] M. Hofmann, F. Steinke, V. Scheel, G. Charpiat, J. Farquhar, P. Aschoff, M. Brady, B. Schölkopf, and B. J. Pichler, "MRI-based attenuation correction for PET/MRI: a novel approach combining pattern recognition and atlas registration", J. Nucl. Med., vol. 49, no. 11, pp. 1875–1883, 2008.

[45] P. B. Greer, J. a. Dowling, J. a. Lambert, J. Fripp, J. Parker, J. W. Denham, C. Wratten, A. Capp, and O. Salvado, "A magnetic resonance imaging-based workflow for planning radiation therapy for prostate cancer", Med. J. Aust., vol. 194, no. 4, 2011.

[46] N. Burgos, M. J. Cardoso, K. Thielemans, M. Modat, S. Pedemonte, J. Dickson, A. Barnes, R. Ahmed, C. J. Mahoney, J. M. Schott, J. S. Duncan, D. Atkinson, S. R. Arridge, B. F. Hutton, and S. Ourselin, "Attenuation Correction Synthesis for Hybrid PET-MR Scanners: Application to Brain Studies", IEEE Trans. Med. Imaging, vol. 33, no. 12, pp. 2332–2341, 2014.

[47] D. Andreasen, K. Van Leemput, R. H. Hansen, J. a. L. Andersen, and J. M. Edmund, "Patch-based generation of a pseudo CT from conventional MRI sequences for MRI-only radiotherapy of the brain," Med. Phys., vol. 42, no. 4, pp. 1596–1605, 2015.

[48] M. E. Korsholm, L. W. Waring, and J. M. Edmund, "A criterion for the reliable use of MRI-only radiotherapy", Radiat. Oncol., vol. 9, p. 16, 2014.

[49] J. H. Jonsson, M. G. Karlsson, M. Karlsson, and T. Nyholm, "Treatment planning using MRI data: an analysis of the dose calculation accuracy for different treatment regions", Radiat. Oncol., vol. 5, p. 62, 2010.

[50] A. L. Chin, A. Lin, S. Anamalayil, and B.-K. K. Teo, "Feasibility and limitations of bulk density assignment in MRI for head and neck IMRT treatment planning", J. Appl. Clin. Med. Phys., vol. 15, no. 5, p. 4851, Jan. 2014.

[51] M. Kapanen and M. Tenhunen, "T1/T2*-weighted MRI provides clinically relevant pseudo-CT density data for the pelvic bones in MRI-only based radiotherapy treatment planning", Acta Oncol. (Madr)., no. May 2012, pp. 1–7, 2012.

[52] J. Korhonen, M. Kapanen, J. Keyriläinen, T. Seppälä, and M. Tenhunen, "A dual model HU conversion from MRI intensity values within and outside of bone segment for MRI-based radiotherapy treatment planning of prostate cancer", Med. Phys., vol. 41, no. 1, p. 011704, 2014.

[53] A. Johansson, M. Karlsson, and T. Nyholm, "CT substitute derived from MRI sequences with ultrashort echo time", Med. Phys., vol. 38, no. 5, pp. 2708–2714, 2011.

[54] M. S. R. Gudur, W. Hara, Q.-T. Le, L. Wang, L. Xing, and R. Li, "A unifying probabilistic Bayesian approach to derive electron density from MRI for radiation therapy treatment planning", Phys. Med. Biol., vol. 59, no. 21, pp. 6595–6606, 2014.

[55] S. Hsu, Y. Cao, K. Huang, M. Feng, and J. M. Balter, "Investigation of a method for generating synthetic CT models from MRI scans of the head and neck for radiation therapy", vol. 8419, 2013.

[56] C. M. Rank, C. Tremmel, N. Hünemohr, A. M. Nagel, O. Jäkel, and S. Greilich, "MRI-based treatment plan simulation and adaptation for ion radiotherapy using a classification-based approach", Radiat. Oncol., vol. 8, p. 51, 2013.

[57] A. Karotki, K. Mah, G. Meijer, and M. Meltsner, "Comparison of bulk electron density and voxel-based electron density treatment planning", J. Appl. Clin. Med. Phys., vol. 12, no. 4, p. 3522, 2011.

[58] D. J. Tyler, M. D. Robson, R. M. Henkelman, I. R. Young, and G. M. Bydder, "Magnetic Resonance Imaging with Ultrashort TE (UTE) PULSE sequences: Technical Considerations", J. Magn. Reson. Imaging, vol. 25, no. 2, pp. 279–289, 2007.

[59] J. E. Holmes and G. M. Bydder, "MR imaging with ultrashort TE (UTE) pulse sequences: Basic principles", Radiography, vol. 11, no. 3, pp. 163–174, 2005.

[60] A. Johansson, M. Karlsson, J. Yu, T. Asklund, and T. Nyholm, "Voxel-wise uncertainty in CT substitute derived from MRI", Med. Phys., vol. 39, no. 6, p. 3283, 2012.

[61] Y. Berker, J. Franke, a. Salomon, M. Palmowski, H. C. W. Donker, Y. Temur, F. M. Mottaghy, C. Kuhl, D. Izquierdo-Garcia, Z. a. Fayad, F. Kiessling, and V. Schulz, "MRI-Based Attenuation Correction for Hybrid PET/MRI Systems: A 4-Class Tissue Segmentation Technique Using a Combined Ultrashort-Echo-Time/Dixon MRI Sequence", J. Nucl. Med., vol. 53, no. 5, pp. 796–804, 2012.

[62] D. a. Jaffray, J. H. Siewerdsen, J. W. Wong, and A. a. Martinez, "Flat-panel cone-beam computed tomography for image-guided radiation therapy", Int. J. Radiat. Oncol. Biol. Phys., vol. 53, no. 5, pp. 1337–1349, 2002.

[63] M. H. P. Smitsmans, J. De Bois, J. J. Sonke, A. Betgen, L. J. Zijp, D. a. Jaffray, J. V. Lebesque, and M. Van Herk, "Automatic prostate localization on cone-beam CT scans for high precision image-guided radiotherapy", Int. J. Radiat. Oncol. Biol. Phys., vol. 63, no. 4, pp. 975–984, 2005.

[64] H. a. McNair, S. a. Mangar, J. Coffey, B. Shoulders, V. N. Hansen, A. Norman, J. Staffurth, S. A. Sohaib, A. P. Warrington, and D. P. Dearnaley, "A comparison of CT- and ultrasound-based imaging to localize the prostate for external beam radiotherapy", Int. J. Radiat. Oncol. Biol. Phys., vol. 65, no. 3, pp. 678–687, 2006.

[65] L. Xing, B. Thorndyke, E. Schreibmann, Y. Yang, T. F. Li, G. Y. Kim, G. Luxton, and A. Koong, "Overview of image-guided radiation therapy", Med. Dosim., vol. 31, no. 2, pp. 91–112, 2006.

[66] J. J. W. Lagendijk, B. W. Raaymakers, A. J. E. Raaijmakers, J. Overweg, K. J. Brown, E. M. Kerkhof, R. W. van der Put, B. Hårdemark, M. van Vulpen, and U. a. van der Heide, "MRI/linac integration", Radiother. Oncol., vol. 86, no. 1, pp. 25–29, 2008.

[67] J. E. Raaijmakers, B. W. Raaymakers, and J. J. W. Lagendijk, "Magnetic-field-induced dose effects in MR-guided radiotherapy systems: dependence on the magnetic field strength", Phys. Med. Biol., vol. 53, no. 4, pp. 909–923, 2008.

[68] B. H. Kristensen, F. J. Laursen, V. Løgager, P. F. Geertsen, and A. Krarup-Hansen, "Dosimetric and geometric evaluation of an open low-field magnetic resonance simulator for radiotherapy treatment planning of brain tumours," Radiother. Oncol., vol. 87, no. 1, pp. 100–109, 2008.

[69] J. Lambert, P. B. Greer, F. Menk, J. Patterson, J. Parker, K. Dahl, S. Gupta, A. Capp, C. Wratten, C. Tang, M. Kumar, J. Dowling, S. Hauville, C. Hughes, K. Fisher, P. Lau, J. W. Denham, and O. Salvado, "MRI-guided prostate radiation therapy planning: Investigation of dosimetric accuracy of MRI-based dose planning", Radiother. Oncol., vol. 98, no. 3, pp. 330–334, 2011.

[70] T. Stanescu, H.-S. Jans, N. Pervez, P. Stavrev, and B. G. Fallone, "A study on the magnetic resonance imaging (MRI)-based radiation treatment planning of intracranial lesions", Phys. Med. Biol., vol. 53, no. 13, pp. 3579–3593, 2008.

[71] K. Eilertsen, L. N. T. A. Vestad, O. Geier, and A. Skretting, "A simulation of MRI based dose calculations on the basis of radiotherapy planning CT images", Acta Oncol., vol. 47, no. 7, pp. 1294–1302, 2008.

[72] L. Chen, R. a. Price, L. Wang, J. Li, L. Qin, S. McNeeley, C. M. C. Ma, G. M. Freedman, and A. Pollack, "MRI-based treatment planning for radiotherapy: Dosimetric verification for prostate IMRT", Int. J. Radiat. Oncol. Biol. Phys., vol. 60, no. 2, pp. 636–647, 2004.

[73] M. Hofmann, B. Pichler, B. Schölkopf, and T. Beyer, "Towards quantitative PET/MRI: A review of MR-based attenuation correction techniques", Eur. J. Nucl. Med. Mol. Imaging, vol. 36, no. SUPPL. 1, pp. 93–104, 2009.

[74] E. Schreibmann, J. A. Nye, D. M. Schuster, D. R. Martin, J. Votaw, and T. Fox, "MR-based attenuation correction for hybrid PET-MR brain imaging systems using deformable image registration", Med. Phys., vol. 37, no. 5, pp. 2101–9, May 2010.

[75] J. H. Jonsson, A. Johansson, K. Söderström, T. Asklund, and T. Nyholm, "Treatment planning of intracranial targets on MRI derived substitute CT data", Radiother. Oncol., vol. 108, no. 1, pp. 118–122, 2013.

[76] C. M. Rank, N. Hünemohr, A. M. Nagel, M. C. Röthke, O. Jäkel, and S. Greilich, "MRI-based simulation of treatment plans for ion radiotherapy in the brain region", Radiother. Oncol., vol. 109, no. 3, pp. 414–418, 2013.

[77] N. Burgos, M. J. Cardoso, F. Guerreiro, C. Veiga, M. Modat, J. Mcclelland, A. Knopf, S. Punwani, D. Atkinson, S. R, Arridge and B. F. Hutton, "Robust CT Synthesis for Radiotherapy Planning: Applicationto the Head and Neck region", MICCAI, 2015.

[78] J. Juntu, J. Sijbers, D. Van Dyck, and J. Gielen, "Bias field correction for MRI images", Comput. Recognit. Syst., vol. 30, pp. 543–551, 2005.

[79] N. J. Tustison, B. B. Avants, P. a. Cook, Y. Zheng, A. Egan, P. a. Yushkevich, and J. C. Gee, "N4ITK: Improved N3 bias correction", IEEE Trans. Med. Imaging, vol. 29, no. 6, pp. 1310–1320, 2010.

[80] S. Ourselin, a. Roche, G. Subsol, X. Pennec, and N. Ayache, "Reconstructing a 3D structure from serial histological sections", Image Vis. Comput., vol. 19, no. 1–2, pp. 25–31, 2001.

[81] M. Modat, D. M. Cash, P. Daga, G. P. Winston, J. S. Duncan, and S. Ourselin, "Global image registration using a symmetric block-matching approach," J. Med. Imaging, vol. 1, no. 2, p. 024003, Sep. 2014.

[82] M. Modat, G. R. Ridgway, Z. a. Taylor, M. Lehmann, J. Barnes, D. J. Hawkes, N. C. Fox, and S. Ourselin, "Fast free-form deformation using graphics processing units", Comput. Methods Programs Biomed., vol. 98, no. 3, pp. 278–284, 2010.

[83] J. a Shackleford, N. Kandasamy, and G. C. Sharp, "On developing B-spline registration algorithms for multi-core processors", Phys. Med. Biol., vol. 55, no. 21, pp. 6329–6351, 2010.

[84] P. Cachier, E. Bardinet, D. Dormont, X. Pennec, and N. Ayache, "Iconic feature based nonrigid registration: the PASHA algorithm", Comput. Vis. Image Underst., vol. 89, no. 2–3, pp. 272–298, Feb. 2003.

[85] C. Coolens and P. J. Childs, "Calibration of CT Hounsfield units for radiotherapy treatment planning of patients with metallic hip prostheses: the use of the extended CT-scale", IOP Publishing, 07-Jun-2003.

[86] E. Spezi, D. G. Lewis, and C. W. Smith, "A DICOM-RT-based toolbox for the evaluation and verification of radiotherapy plans", Phys. Med. Biol., vol. 47, no. 23, pp. 4223–4232, 2002.

[87] K. H. Zou, S. K. Warfield, A. Bharatha, C. M. C. Tempany, M. R. Kaus, S. J. Haker, W. M. Wells, F. A. Jolesz, and R. Kikinis, "Statistical validation of image segmentation quality based on a spatial overlap index", Acad. Radiol., vol. 11, no. 2, pp. 178–89, Feb. 2004.

[88] A. P. Zijdenbos, B. M. Dawant, R. A. Margolin, and A. C. Palmer, "Morphometric analysis of white matter lesions in MR images: method and validation", IEEE Trans. Med. Imaging, vol. 13, no. 4, pp. 716–24, Jan. 1994.

[89] I. M. Systems, "Monaco ® User Guide," 2013.

[90] I. M. Systems, "Monaco ® Training Guide," 2013.

Appendix

Appendix A

Matlab code

A.1 Function used to convert sCT from NIfTI to DICOM

sCT_a were generated in a NIfTI format. To be able to evaluate the method, the scans had to be imported into RayStation. All input files in RayStation have to be in a DICOM format. This matlab code was used to convert the sCT_a to DICOM images in a way that the system recognizes the sCT_as as CT scans.

```
function [] = CBCT_saveDICOM(nii, pathname_1,pathname_2)

%nii= name of the .nii file that contains the image.[load_untouch_nii]

files_1 = dir(pathname_1);% CT folder
files_2 = dir(pathname_2);% MR folder


%random min value that will, in principle, always be bigger than any z
%position of any slice
dz=1000;

%searching for the location of the 1st slice.
for i = 3:length(files_1);
        info(i) = dicominfo([pathname_1 filesep files_1(i).name]);
end


%identifier of CBCT DICOM series
CBCT_SeriesInstanceUID = dicomuid;
SeriesNumber = 2;


%get rest of information needed to write the DICOM FILE properly

IM_3D = nii.img;

x = - nii.hdr.hist.srow_x(1,4);
```

```
y = - nii.hdr.hist.srow_y(1,4);
z = nii.hdr.hist.srow_z(1,4);
rows =nii.hdr.dime.dim(1,2);
columns = nii.hdr.dime.dim(1,3);
N = nii.hdr.dime.dim(1,4);
Pixel_spacing(1,1) = nii.hdr.dime.pixdim(1,3);
Pixel_spacing(1,2) = nii.hdr.dime.pixdim(1,2);
Slice_thickness = nii.hdr.dime.pixdim(1,4);

%linear transformation of pixel value to HU
%To convert CT images in nifty to CT images in dicom
%slope = nii.hdr.dime.scl_slope;
%intercept = nii.hdr.dime.scl_inter;

%To convert sCT images in nifty to sCT in dicom(loaded as CT scans)
slope=info(3).RescaleSlope;
intercept=0;


%Definition of Window Center and Window Width
MR_info = dicominfo([pathname_2 filesep files_2(3).name]);
center=MR_info.WindowCenter;
width=MR_info.WindowWidth;

for i=1:N


    disp(['writing slice ' num2str(i)]);
    savename = '';
    if i < 100
        savename ='0';
        if i < 10
        savename ='00';
        end
    end

    savename = ['CBCT_' savename num2str(i) '.dcm'];

    IM_2D = int16(IM_3D(:,:,i)');
    IM_2D(IM_2D<-1000) = -1000;
    dicomwrite(IM_2D, savename, info(3),'SeriesInstanceUID',
        CBCT_SeriesInstanceUID, 'SeriesNumber', SeriesNumber, '
        InstanceNumber', i, 'ImageOrientationPatient', [1 0 0 0 1 0]',
         'ImagePositionPatient', [x y z + Slice_thickness*(i-1)], '
        SliceLocation', z + Slice_thickness*(i-1), 'Rows', rows, '
        Columns', columns,'RescaleIntercept', intercept, 'RescaleSlope
        ', slope, 'WindowCenter', center, 'WindowWidth', width, '
        SliceThickness', Slice_thickness, 'PixelSpacing',
        Pixel_spacing)
end
```

A.2 2D Local Gamma Analysis Function

```
function [gamma_map] = gamma_test(ima1,ima2,resolution_mm,
    delta_radius_mm,delta_dose_percent)
% Calculate the gamma map to compare to different x-ray images
% Criterion derived from T. Depuydt et al., Radio&Oncol 62 (2002)
    309-319

%save memory: -> single
ima1=single(ima1);
ima2=single(ima2);

%check if dimensions match
if size(ima1) ~= size(ima2)
    return;
end

%radius in pixel from mm for acceptance criterion
radius_pix=round(delta_radius_mm/resolution_mm);

%square box around pixel of interest
dim=2*radius_pix+1;
%distance of neighbourhood pixels
distance_to_centre=zeros(dim,dim);
%calculate actual distances in pixel
for j=1:dim
        for l=1:dim
            distance_to_centre(j,l)=sqrt((j-1-radius_pix)^2+(l-1-
                radius_pix)^2);
        end
end

%calculate squared relative distance for gamma criterion
distance_to_centre_relative=(distance_to_centre./radius_pix).^2;

%calculate squared dose limit for gamma criterion
dose_limit=(delta_dose_percent.*ima1./100).^2;

%finding running indexes for square box of pixels
y=zeros(dim^2,3);
y(:,1)=1:(dim)^2;

for ii=1:dim
y(1+(ii-1)*dim:(ii)*dim,2)=1:dim;
y(1+(ii-1)*dim:(ii)*dim,3)=ii;
end

%reduce number of arrays that need to be stored! "Edges" of square
    arrays violate
%distance condition
number_of_redundance=distance_to_centre > radius_pix;
```

```
46 z=distance_to_centre(number_of_redundance);
47 redundance=size(z,1);
48
49 %initialize new y array to look at valid pixel distances only
50 h=(y(:,2)-radius_pix-1).^2 + (y(:,3)-radius_pix-1).^2 <= radius_pix
       ^2;
51 m=y(h,:);
52
53 %initialise large array of shifted matrices: single to save memory
54 dose_difference=zeros(size(ima1,1),size(ima1,2),dim^2-redundance,'
       single');
55
56 for ii=1:dim^2-redundance
57         %shift ima2 with respect to pixel of interest
58         dose_difference(:,:,ii)=circshift(ima2,[(y(m(ii,1),2)-
               radius_pix-1) (y(m(ii,1),3)-radius_pix-1)]);
59         %calc gamma index -> store in same matrix
60         dose_difference(:,:,ii)=sqrt(distance_to_centre_relative(m(ii
               ,1)) + (dose_difference(:,:,ii)-ima1).^2./dose_limit);
61         %clear border with zeros
62         dose_difference(1:dim,:,ii)=0; dose_difference(size(ima1,1)-
               dim:size(ima1,1),:,ii)=0;
63         dose_difference(:,1:dim,ii)=0; dose_difference(:,size(ima1,2)
               -dim:size(ima1,2),ii)=0;
64 end
65
66 % remove NaN entries (happens if dose_limit is 0
67 dose_difference(isnan(dose_difference)) = 0 ;
68
69 %print output array
70 gamma_map=min(dose_difference,[],3);
71
72 end
```

Appendix B

Abstract Accepted for 3rd MR in RT Symposium in Lund

Purpose: The gold standard for radiotherapy treatment planning is CT imaging, as it provides high spatial resolution and electron density values. The main arguments for substituting CT for MRI are the superior soft-tissue contrast of MR images and the avoidance of imaging dose. The establishment of a MRI-only workflow in RTP depends on the ability to generate a synthetic CT (sCT) that can be used for dose calculations and the ability to delineate accurate VOIs for treatment planning. In this study, we evaluate Bulk Density Assignment (sCT_{bda}) and Atlas-based (sCT_a) methods to generate sCTs for head and neck (H&N) patients.

Methods: sCT_{bda} and sCT_a based on T2_weighted MRI- and CT-scans acquired on the same day were generated for six H&N patients. For sCT_{bda}, densities of 1.53 g/cm^3 for bone and 0.001 g/cm^3 for air were assigned to segmented structures in the MRI using a combination of threshold-based and manual delineation. The remaining anatomy was defined to be of water equivalent density. sCT_a were obtained from an anatomical atlas based on seventeen pre-acquired pairs of non-rigidly aligned T2 MR and CT images. Local similarity measures (like local normalised correlation coefficient) were used to match the patient's MRI with the atlas database.
Clinical VMAT plans with a prescribed dose of 65 Gy were re-calculated on both sCT_{bda} and sCT_a. A dosimetric evaluation, including dose differences and gamma analysis, was performed using the original planning contours. Original contours and delineations/segmentations on the MRI and sCT_a were evaluated in terms of shape, position and volume using the Dice Similarity Coefficient (DSC).

Results: Gamma analysis (2mm_2%) showed that dose distributions re-calculated on the sCT_{bda} and sCT_a were comparable. Compared to the original dose distribution, differences were less than 1 Gy in the PTV. Differences of Dmean in the PTV ranged from -0.9% to 0.3% for sCT_{bda} and from -0.4 to 0.4% for sCT_a. More points at the outer contour failed the gamma criteria due to external contour differences.
The outlines of the body and bone contours in the sCT_a and the original CT were very similar in shape, position and volume. Obvious deviations in shape and in volume could be observed between original bone contours and contours based on the MRI. However, DSC values ranged from 0.73 to 0.86 when comparing bone contours on the sCT_a with the original CT, and from 0.71 to 0.82 when comparing bone contours on the MRI with the original CT.

Conclusions: Dose re-calculations on sCT_{bda} and sCT_a showed no clinically relevant dose differences to the original dose distribution on the planning CT. Hence, sCT obtained with either method are suitable to perform dose calculations. Also, contours based on MRI and sCT_a

were found to be similar. However, segmentation of bone on the MRI cannot be performed fully automatically and the sCT_a cannot provide information of the target volume. We therefore suggest combining soft tissue contours based on MRI with bone contours obtained from the sCT_a in order to establish a MRI-only workflow for future MR-Linac machines.